NUMERICAL MODELING ON SCRATCH AND MAR INDUCED DAMAGES IN POLYMERIC SYSTEMS

A Dissertation

by

SHUORAN DU

Submitted to the Office of Graduate and Professional Studies of
Texas A&M University
in partial fulfillment of the requirements for the degree of

DOCTOR OF PHILOSOPHY

Chair of Committee,	Hung-Jue Sue
Committee Members,	Harry Hogan
	C. Steve Suh
	Svetlana Sukhishvili
Head of Department,	Andreas A.Polycarpou

December 2020

Major Subject: Mechanical Engineering

ABSTRACT

The barrel mar behavior, scratch-induced delamination, and temperature-dependent scratch behavior were investigated in this dissertation via FEM modeling. The experimental tests were carried out according to ASTM/ISO standard to validate the FEM model.

Three amorphous polymers PMMA, PC, and PS were employed to study the barrel mar behavior. By comparison to experimental results, the numerical analysis showed that the maximum plastic principal strain (ε_1^p) and total dissipated plastic energy (E_p) can be considered for evaluating mar visibility resistance. Higher mar visibility resistance corresponds to lower ε_1^p and E_p values. Based on these two criteria, the parametric analysis shows that mar visibility resistance increases with lower modulus, higher yield stress, higher hardening slope, and lower softening slope.

The FEA analysis to compare the delamination resistance of two semi-rigid PET-based laminates was conducted. The results show that the maximum principal stress distribution at the interface correlates well with the scratch-induced delamination behavior. A followed study was performed to validate the semi-quantitative FEM modeling approach with the double-layer epoxy-based polymeric coatings. The parametric study reveals the delamination at the interface could initiate either from the scratch shoulder region or behind the scratch tip.

A FEM modeling methodology to quantitatively predict the temperature-dependent scratch behavior of amorphous polymers was proposed with the following

theories. The Arruda-Boyce viscoplastic model is utilized to account for temperature and strain rate dependent strain-softening and strain-hardening behaviors. The post-yield behavior predicted in this model is calibrated using the yield point determined by the Richeton cooperative model. The pressure dependent Drucker-Prager model with calibrated post-yield experimental data at various strain rates is chosen as the plastic constitutive relationship of the polymeric systems for FEM simulation. Furthermore, temperature and pressure dependent frictional behavior is input into an ABAQUS contact model to simulate the variation of the adhesion coefficient of friction (μ_a). The FEM simulation findings show a good agreement with the experimentally determined scratch depth and scratch coefficient of friction (SCOF) measured using the scratch test.

DEDICATION

To my family and friends

ACKNOWLEDGEMENTS

I would like to deeply thank my committee chair, Professor Hung-Jue Sue, for his patience, immense knowledge, and continuous support for my Ph.D. study. And I also would like to thank my committee members Prof. Harry A. Hogan, Prof. C. Steve Suh, and Prof. Svetlana Sukhishvili for their generous encouragement and advice. Special thanks to Texas A&M Scratch Behavior Consortium members for the financial and sample support.

I also would like to express my gratitude to all of my colleagues from Texas A&M Polymer Technology Center. Thanks to their kindness, encouragement, and help in my graduate study and life. Particularly, thanks to Dr. Michael J. Mullins, Dr. Mohammad Hossain, Mr. Yang Xu, and Dr. Lei Xu for their constructive discussions and the knowledge that they would like to share with me.

Next, I would like to acknowledge the assistance of my friends who make my life in Texas A&M colorful and meaningful.

Finally, I would like to sincerely thank my father Jinshui, my mother Lihong, and my family members for their support and love.

CONTRIBUTORS AND FUNDING SOURCES

This work was supervised by a dissertation committee consisting of Professor Hung-Jue Sue, Harry Hogan, and C. Steve Suh of the Department of Mechanical Engineering and Professor Svetlana Sukhishvili of the Department of Material Science and Engineering.

The SEM images in Chapter IV were captured by Dr. Marc Mamak and Dr. Mark Agerton from The Procter & Gamble Company. The scratch tests in Chapter IV were performed by Glendimar Molero of the Department of Material Science and Engineering and were published in 2019.

All other work conducted for the dissertation was completed by the student independently.

Graduate study was supported by Texas A&M Scratch Behavior Consortium.

TABLE OF CONTENTS

Page

LIST OF FIGURES

Page

LIST OF TABLES

Page

CHAPTER I

INTRODUCTION[*]

Due to the growing adjustability of composition and geometry, polymers are extensively utilized in a wide range of industries such as automotive, packaging, and electronics. Their outstanding mechanical and aesthetic functionalities make polymers useful for electronic portable devices, coatings, automotive interior panels, and so on. However, surface damages are detrimental to the functional and perceptual properties of the polymer products. For example, as for the application in the electronic device industry, the surface damages on the touch screen could significantly reduce the efficiency of reading and controlling. In the packaging industry, the scratch damage could cause the polymer films to lose the ability to retain the structural integrity and barrier properties, which may spoil the product inside. Additionally, in the coating applications, surface damages such as sharp scratches could make the underlying metal directly exposed to air and speed up the corrosion process. The main concern about surface damages in the application of the automotive industry is about aesthetic properties. The damages so-called 'Scoff' and 'soil' on the exterior or interior parts of the vehicle have been ranked as the

[*] Part of this chapter was reprinted from Wear, 444-445, Du, S., Hamdi, M., Sue, H.-J., Experimental and FEM analysis of mar behavior on amorphous polymers, 203155, Copyright (2020), with permission from Elsevier.

[*] Part of this chapter was reprinted from Polymer, 197, Du, S., Mullins, M., Hamdi, M., Sue, H.-J., Quantitative modeling of scratch behavior of amorphous polymers at elevated temperatures, 122504. Copyright (2020), with permission from Elsevier.

top 4 concerning properties in the results of initial quality surveys (IQS) filled out by consumers [1].

Fredrich and his co-workers have clarified the tribological issues into mainly two types, the multi-pass tribological damage like wear and the single-pass tribological damage such as scratch and mar [2]. Compared to wear behavior, the fundamental studies about single-pass tribological damage is still limited to feed the wide applications mentioned above. Single-pass tribological surface damage has been recognized and categorized into ‘scratch’ and ‘mar’ based on the large volume of previous research activities. These two terms are carelessly exchanged in some of the studies, but they are two different types of damages in definitions. Scratch, defined as severe, readily visible surface damage resulting from a sliding asperity, is one of the most concerning surface damages for surface quality retention [2, 3]. Mar is defined as a type of subtle surface damage barely visible to the human eye caused by sliding objects [4]. Previous studies quantified scratch resistance based on the scratch groove dimensions, namely its depth, width, and shoulder height [5, 6]. Furthermore, distinctive damage transitions are commonly observed along the scratch path as the applied scratch load increases according to the ASTM-7027/ISO-19252 standards. For example, Browning found that periodic micro-cracks developed in the scratch groove for brittle styrene-acrylonitrile (SAN) random copolymers when the scratch normal load reached a critical value [7]. The micro-crack in the scratch groove is not only detrimental to the surface quality of polymers but easily leads to catastrophic failure under cycling load [8]. For higher scratch loads, continuous plowing with massive material removal is observed. For ductile polymers,

periodic fish-scale type damage dominated by stick-slip phenomenon was observed [9, 10]. A large amount of research has proven that scratch on polymeric multilayer systems not only damages the top surface but may also cause delamination between polymeric laminates [11, 12]. However, these scratch behaviors were not observed in the case of mar damage.

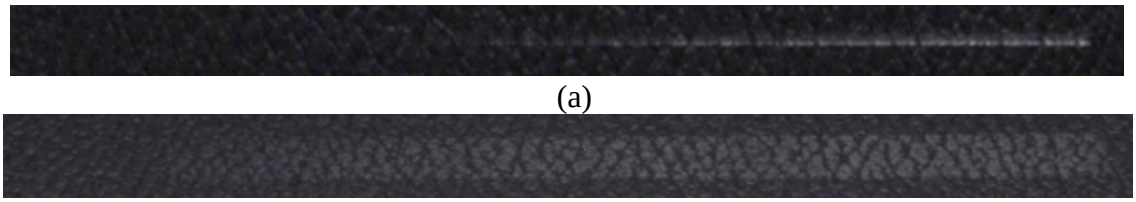

(a)

(b)

Figure I-1. Typical (a) scratch and (b) mar damages on the textured thermoplastic olefin (TPO).

Unlike scratch, this subtle damage feature cannot be easily quantified because of the gradual evolution of mar damage severity upon increased loading. Also, no clear damage transitions could be observed on the mar path. Instead, only progressive changes in surface roughness and possible wavy or proto-craze types of surface damages were found [13]. This makes mar quantification and analysis considerably challenging.

In the view of reasons mentioned above, the ‘scratch’ and ‘mar’ damages should be investigated separately for scientific study. In this chapter, a review of the research work about scratch and mar are demonstrated individually. The key findings of previous studies and the considerations to the current studies are discussed. Last but not least, the research topics of the following several chapters are outlined.

I.1. Literature Review of Scratch Behavior of Polymers

Compared to mar, the scratch behavior of polymer has been studied scientifically earlier. The first problem that researchers tried to solve is how to test and evaluate the material scratch resistance. There are some proposed testing methods and testing machines, such as the single-pass pendulum test [14], the five-finger test [15], and the Taber test [16], etc. Most of these tests are applied by the machine with dead load controls. Even though the equilibrium state could be reached in the constant load tests [17], these methodologies show low testing efficiency to quantify the scratch resistance of polymers.

In 2005, a more consistent scratch testing methodology was established as ASTM D7027-05/ISO 19252:08 standard [18]. This new method employs a linearly increasing load with an adjusted constant speed. Instead of using an indentation Berkovich tip [19], a spherical tip made of stainless steel was suggested for utilization to avoid cutting damages in the scratch test. With this method, the scratch resistance of polymers could be easily compared and quantified in mainly three aspects. The first way is to capture the critical load for damage transition at certain conditions during the scratch test. Extensive research work has been carried out to correlate the evolution of scratch induced damages features with the mechanical behavior and surface properties. Jiang and Browning et al. has demonstrated the fish scale type damages caused by stick-slip phenomenon could take place on the Thermoplastic Olefins (TPO) from certain critical loads shown as Figure I-2 (a) [9]. While the epoxy could show micro-crack beginning from a certain load in an increasing load scratch test as shown in Figure I-2 (b). By using this method, Molero et al. has proved epoxy in a higher crosslinking density has better resistance to microcrack

in the scratch test [20]. Moghbelli et al. performed ASTM-D7027 scratch tests on polymethylmethacrylate (PMMA) with different moisture exposure time period, and shows the water could lead to the reduction of scratch resistance to crack damages because water could act as a plasticizer. The crack damage combined with crazing features on one of the PMMAs is shown in Figure I-2 (c). [21]. Browning et al. demonstrate increasing of acrylonitrile (AN) content and molecular weight of styrene-acrylonitrile (SAN) random copolymers results in delaying the onset of micro-cracking due to the improvement of the tensile strength (Figure I-2 (d)) [7].

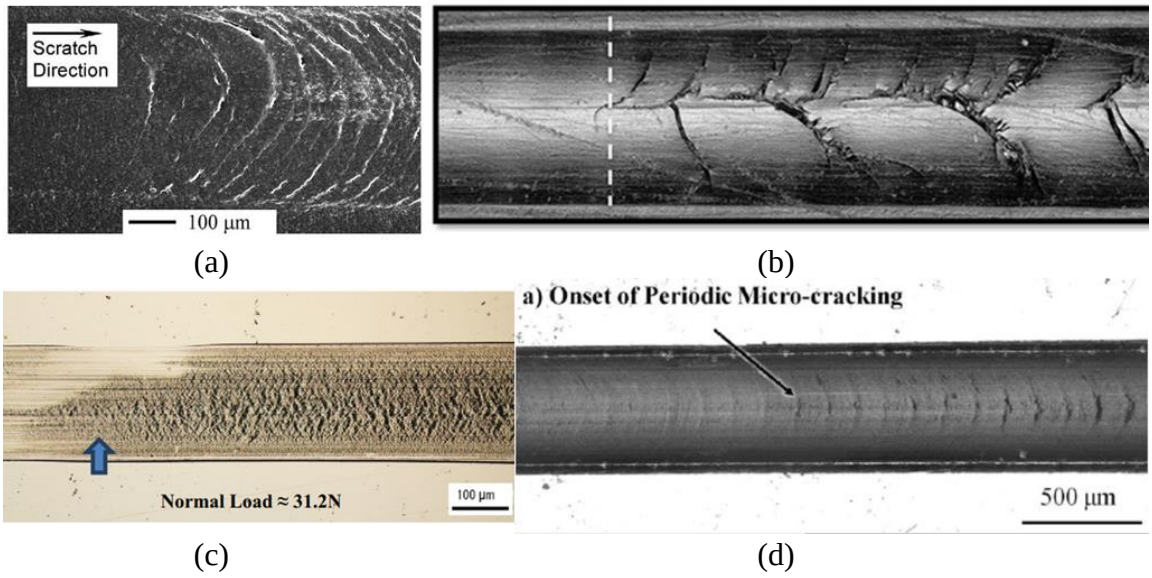

Figure I-2. The crack onset damages of (a) TPO (b) D.E.R. 661 Epoxy (c) PMMA (d) SAN under ASTM-D7027 scratch tests. Respectively reprinted from (a) Jiang et.al [9]. (b) Molero et. al [20] (c) Mogehbelli et. al [21] (d) Browning et. al [7].

The second way to compare and quantify scratch resistance is to measure the material deformation induced by scratch. The scratch groove geometry such as groove

depth, width, and shoulder height as shown in Figure I-3 could be measured with atomic force microscopy (AFM) or the high-resolution 3D scanner such as Laser scanning confocal microscope (LSCM) [22]. The model system with a more severe scratch deformation in the same testing conditions means it has a lower resistance to deformation. The previous studies demonstrated not only material parameters such as modulus and yield stress but the coefficient of friction could affect the scratch resistance to deformation significantly. Hossain et al. found even a 0.1 difference COF on amorphous polymers could lead to about 5- 10 μm different scratch depth and shoulder height value [23]. Fredrich et al. conducted ASTTM-D7027 scratch tests on several high-performance polymers including Polybenzimidazole (PBI), Polyparaphenylene (PPP), Polyetheretherketone (PEEK), Polyimide (PI) [2]. And it shows Polybenzimidazole (PBI) is the most scratch-resistant material among the above-mentioned ones in terms of the scratch width. Browning et al. found the ethylene-propylene rubber (EPR) TPO has a lower scratch depth in the faster scratch test due to the improvement of yield stress at higher strain rates [24].

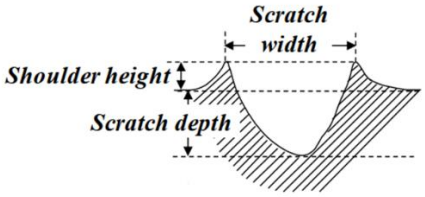

Figure I-3. Schematic of the cross section of scratch groove features. Reprinted from Hossain, et al. [6].

The third aspect to compare and quantify the scratch behavior of polymers is to study the resistance of the scratch groove to the visibility. Scratch becomes visible to human eyes when changes in light scattering/reflection between the scratch path and the background surface exceed 1-3% contrast, depending on the color and gloss of the samples [25, 26]. The physics behind the changes in contrast, can be mainly due to: (1) Change in surface roughness due to the appearance of damages in the scratch groove. Damages such as crazing or brittle crack demonstrate the whitening effect due to the existence of micro-voids. With a non-white virgin color, the scratch becomes easily visible. Therefore, the scratch resistance to the visibility of many crazeable polymers such as Polystyrene (PS), Polymethyl methacrylate (PMMA), Acrylonitrile styrene acrylate (ASA) could be affected by this mechanism [21, 27]. (2) Change in surface topography of the scratch such as groove height and depth. In a certain light condition, a scratch performed by increasing load test begins to become visible from a certain position, because the scratch shoulder height reaches a critical value to show enough contrast compared to the virgin surface [24, 26, 28]. The onset of visibility caused by this reason is closely related to the incident light directions. (3) Change in surface refractive index due to molecular orientation, etc. Based on the above physics, Jiang and Browning et al. proposed the methodology to quantitatively evaluate scratch visibility according to contrast, size, and continuity criteria [26]. Many studies to scratch visibility using this method have shown consistent results with human observation surveys [25, 29, 30]. Scratch resistance to visibility has drawn significant attention in some areas especially the automotive industry. It has been shown the texture could disguise the scratch to some degrees, so that improve the resistance to

scratch visibility [31]. Therefore, the TPO plates used for vehicle interiors are always designed with textures.

To study the mechanics involved during the scratch process, finite element methods (FEM) has been widely used due to its capability to formulate several physical phenomena and unique material response into a single analysis [32]. The advantage of numerical modeling compared to the experiment is that the parametric study could be achieved, since it is extremely difficult to experimentally choose polymers with the systematic change in their constitutive property without altering other properties. For instance, previous studies showed that the elastic modulus and yield stress are usually coupled [33-35]. Similarly, the softening and hardening slopes are interconnected as in the case of PS modified with poly(2,6-dimethyl-1,4-phenylene oxide) or di-(ethyl glycol)-dimethacrylate cross-linking agent [36]. Several FEM numerical studies in the early stages are to study the effects of key parameters on the scratch behaviors of the polymer. For example, Subhash et al. carried out a parametric study with FEM simulation for the displacement-controlled scratch test with an indenter tip. The studies show the maximum tangential force F_T increases with the apex angle α of the indenter and the interfacial friction coefficient μ_s [37]. Some researchers have conducted parametric studies to investigate the effect of material properties and surface conditions on scratch behavior [6, 38, 39]. The typical compressive true stress-strain curves and simplified piece-wise linear curves for parametric study are shown in Figure I-4. It was concluded that the yield stress, strain at stress recovery, and coefficient of surface friction (COF) are the most important parameters for scratch induced deformation [6]. Strain hardening slope has a moderate

effect [6]. Additionally, Young's modulus in the range of 1.65 GPa to 4 GPa could be regarded as no effect on scratch depth [40]. Increasing yield stress, strain at recovery, strain hardening slope, and reducing COF could improve the scratch resistance to deformation.

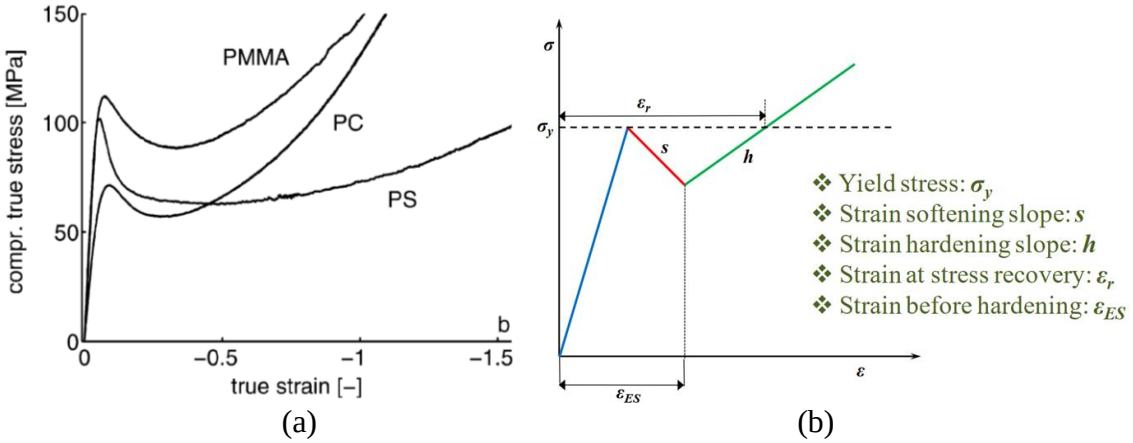

(a) (b)

Figure I-4. (a) Compressive true stress-strain curves of PMMA, PC, and PS, (b) simplified piece-wise linear stress-strain curve for parametric study. Respectively reprinted from (a) Van Melick, et al. [36] (b) Hossain et al. [6].

Extensive previous studies utilized the FEM model described previously to provide a mechanistic explanation of scratch damage. Jiang and his coworkers carried out the FEM simulation to analyze the stress field during the scratch tests [9]. They found the high tensile max. principal stress and hydrostatic tension behind the scratch tip are responsible for the damages such as crack, craze, and microvoid [9]. Xu et al. built a 3D FEM model for alternating multilayered PVDF/PMMA sheets and revealed scratch damage of PVDF material was caused by tensile tearing [41]. With the multiplication of layers, the decrease of tensile stress imposed on the first PVDF layer led to the delay of

scratch damage. Pagmoux et al. utilized the Maximum principal stress field calculated via FEM model considering the coating thickness effect to explain the crack features on the scratch shoulder of the Diamond-Like-Carbon (DLC) coating [12]. Xiao et al. performed a 3D FEM scratch modeling accounting for the mechanical properties of cast Polyurethane (CPU) to explain the bulging phenomenon observed in the mid-portion of the scratch groove [42]. The studies show the von-Mises stress concentration in the PU elastomer model system shift away from the centerline of the scratch path, which couldn't be seen in the semi-rigid or rigid polymers. Hamdi et al. investigated the scratch behavior of polyamide 6 (PA) and propylene (PP) laminates, and utilized FEM modeling to gain an understanding of scratch mechanisms [43]. The low scratch resistance exhibited by the PA/PP laminates was associated with the high stress magnitude at the interface, which led to interfacial failure. Contrarily, PP/PA laminates could minimize interfacial stresses through the absorption of mechanical energy at the top PP layer and by preventing stress concentration build-up at the interface of the bottom PA layer. This behavior was attributed to low friction, material constitutive behavior, and the density-graded structure of PP/PA laminates.

Compared to the above FEM modeling studies, very limited research has attempted to achieve the quantitative prediction of polymer scratch deformation. Jing et. al derived an analytical model for estimating the inelastic and damage zone size for brittle solids [44]. Breemen et. al implemented a hybrid experimental-numerical approach to understand the frictional behavior during the scratch process and proposed a quantitative modeling framework to predict the instantaneous penetration and lateral force during

scratch [45]. Hossain et al. used a FEM parametric study to show that the yield stress, strain at recovery, and strain hardening slope are important factors that influence the residual scratch depth [6, 38]. They have also successfully introduced a numerical model for predicting the scratch-induced deformation of polycarbonate (PC) and styrene acrylonitrile (SAN) at room temperature by incorporating appropriate rate and pressure dependent constitutive models and frictional behaviors [46].

The experimental and numerical research efforts discussed above help us gain insight into the scratch behavior of the polymer. However, there are still many problems waiting to be solved. Due to the complexity of the scratch behaviors mentioned above, a better understanding of the scratch behavior of polymers is still needed.

I.2. Literature Review of Mar Behavior of Polymers

As a new proposed single pass tribological damage, there have been only a few reports that focus on the mar behavior of polymers. As mentioned above, mar is a different type of surface damage from scratch. Mar damage can be caused by one or a combination of the following mechanisms: meniscus wrinkling, uneven viscoelastic deformation, localized molecular orientation, crazing, shear banding, and micro-cracking. The underlying physics of most of these mechanisms are still unclear and cannot be easily modeled. Depending on the surface properties, mar damage can be induced by two mechanisms, ironing or roughening [4]. The ironing process is usually formed on rough surfaces. Surface asperities are suppressed by the smoother mar tip and the mar area

becomes smoother than the background of the sample. In contrast, roughening mar is usually formed on smooth surfaces. The damaged area is roughened by the mar tip.

While the research to mar and scratch is closely related especially in terms of testing and evaluation methods. The ASTM-7027/ISO-19252 standards designed for testing scratch behavior have been extended to mar testing by changing sliding tips, either a smooth barrel head or a tip with rough sandpaper surface respectively shown in Figure I-5 (a) (b) [29]. A smooth barrel head usually causes ironing mar. However, it can also induce roughening damage when the roughness of the mar head is higher than that of the polymer surface [4]. Given its significant roughness, the sandpaper surface can only generate roughening mar damage. Recently, the smooth barrel tip was used to conduct mar tests on textured thermoplastic olefin (TPO) designed for automotive interior parts. This study found a good correlation between the obtained mar damage performance and the results of initial quality surveys (IQS) filled out by consumers [1]. Therefore, this testing condition will be considered in our study because of its simplicity and practicality. As for the mar resistance evaluation, due to the lack of clear damage transition and obvious geometrical change on the mar path, the mar resistance could be only captured through visibility. Chrisman and Hamdi have successfully conducted linear increasing load mar tests on polymeric films and TPO bulks. And the mar resistance of different samples was evaluated based on the contrast curve as a function of the normal load. It turns out the mar damage visibility determined by this methodology correlates well with human perceptions. However, no FEM study has been conducted to investigate the behavior of mar induced damage [4, 43].

(a) (b)

Figure I-5. The tips to test mar behaviors of polymers with ASTM-7027/ISO-19252 standards (a) barrel mar tip (b) sandpaper mar tip. Reprinted from Chrisman et al. [29].

I.3. Research Scopes and Dissertation Layout

The literature review about single-pass tribological damages gives us a hint about the fundamental knowledge that has been generated and the problems still waiting for resolved. Due to the broad scope of this field, several research topics are determined based on the achievements of previous studies and recently developed techniques. The knowledge generated via the research efforts in the current dissertation provides the guidelines for the development of scratch and mar resistant polymeric systems.

In Chapter II, the research subtopics covered in this dissertation are highlights. Furthermore, because of the complexity as pointed out above, the research strategy to each research subtopic is illustrated in this Chapter.

Chapter III focuses on the mar behavior of polymers. This subtle damage is highly under-investigated because of its complexity for modeling [30]. Due to the gradually increasing intention to mar damages from various industries, building a FEM model to study the mar damage is the precondition for future fundamental research. Therefore, in

this chapter, the FEM analysis to mar behavior of several engineering polymers is carried out to connect the visibility evaluation with mechanics knowledge.

Chapter IV and V, and VI focus on scratch behaviors of the polymer. Extensive FEM studies have modeled the scratch deformation without damages [5, 47, 48]. But scratch induced damages such as crack, stick-slip features, etc. are still under-investigated [49]. Delamination is one of the most common scratch induced damages in various multilayer polymeric systems such as food packaging, photonic devices, and automotive exterior paint. However, due to the lack of fundamental studies in this field, there are still many unknowns. Both Chapter IV and Chapter V are about experimental and FEM analysis to scratch induced delamination damage. In Chapter IV, the FEM modeling combined with the scratch test is carried out to investigate the corresponding stress state that causes delamination during scratching in the semi-rigid multi-layer polymeric systems. Furthermore, the delamination strength of the model systems is semi-quantitatively assessed. In Chapter V, experimental work is carried out to validate the FEM modeling approach for the quantitative determination of delamination strength proposed in Chapter IV. Besides that, a parametric study is conducted in this chapter to gain insight into the effect of layer thicknesses and material parameters on delamination behavior in the scratch test.

From the above literature review, another under-investigated research topic is the development of quantitative modeling methodology to predict scratch behavior under different conditions. This topic is significant since the achievements could help to predict the scratch behavior in advance. Due to the development of polymeric-based composite

materials, more and more products made of polymer have been used at different temperatures, such as warm/cold food packaging, fire-safety products, and automotive ventilation systems. However, surface quality is still required to be maintained in different conditions. Due to the highly temperature-dependent behavior of polymers, scratch at elevated temperatures always demonstrates more severe deformation than that at room temperature [50, 51]. Therefore, Chapter V focuses on proposing a quantitative FEM model to predict the temperature-dependent scratch deformation [22]. Also in this chapter, the chosen theories that describe temperature dependent constitutive and friction behaviors are illustrated in details. Then, the contributions to the polymeric research community and the limitations of the proposed model are discussed in the chapter as well.

CHAPTER II

OVERVIEW OF RESEARCH OBJECTIVES AND STRATEGIES[*]

To model the scratch and mar behavior of polymeric systems, there are mainly three types of factors that should be considered in the FEM analysis as shown in Figure II-1, namely constitutive behavior, contact behavior, and structure & geometry. It is well-known that the constitutive properties of the polymer are strain-rate dependent, hydrostatic pressure dependent, temperature-dependent, and time dependent [52]. Different from ceramics and steel, most of the polymers such as Polypropylene (PP) and Polycarbonate (PC) demonstrated inelastic region and strain-softening behaviors respectively before and after yielding point [53]. Unfortunately, there is no one universal model that could predict all of this constitutive behavior precisely in a wide testing ranges until now [30]. Therefore, it is very important to choose appropriate polymeric constitutive models and make certain assumptions according to the research objective. The second type of behavior needed to be taken into account in the scratch and mar simulation is the contact behavior. From the literature review in Chapter I, the texture pattern and roughness of the polymeric surface, and the coefficient of friction (COF) between the contact pairs could affect the scratch and mar damages significantly [23, 25]. Last but not least, as for the polymeric

---

[*] Part of this chapter was reprinted from Wear, 444-445, Du, S., Hamdi, M., Sue, H.-J. Experimental and FEM analysis of mar behavior on amorphous polymers, 203155, Copyright (2020), with permission from Elsevier.

[*] Part of this chapter was reprinted from Polymer, 197, Du, S., Mullins, M., Hamdi, M., Sue, H.-J., Quantitative modeling of scratch behavior of amorphous polymers at elevated temperatures, 122504. Copyright (2020), with permission from Elsevier.

systems with complicated structures, such as multi-phase composite or multilayer laminates, the structure and geometry has to be considered in the FEM model [43, 54, 55]. For example, Chandelia et al. studied the scratch behavior of epoxy/silica and epoxy/rubber micro-composites. They found a higher plastic deformation is induced with an increase in volume fraction for both types of particles compared to neat epoxy. And deeper residual scratch depth is expected in composites containing micro rubber particles than containing silica particles [56].

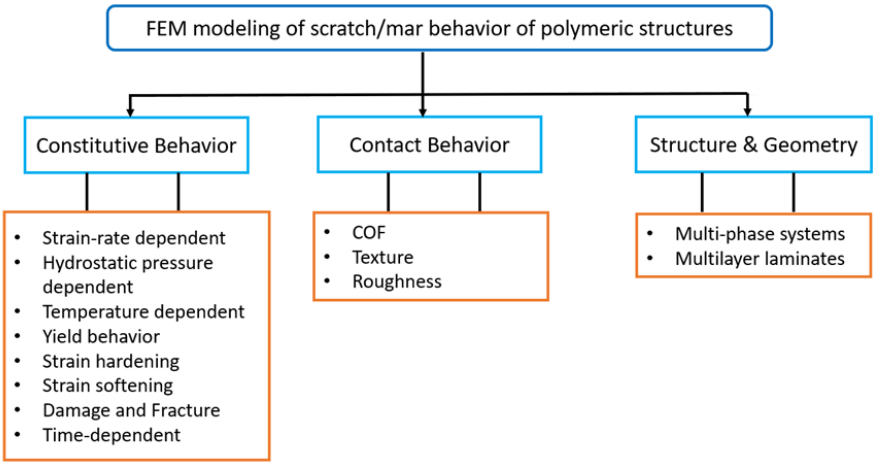

Figure II-1. Factors to be considered in the FEM scratch and mar model.

However, it is not always necessary to take all of these factors into account in the FEM scratch and mar model. Making assumptions appropriately to ignore some non-key factors is critical to keep computational efficiency. For example, the polymer strength is always ignored in the numerical model for analyzing the scratch deformation without crack and micro-void damages [39, 43, 57]. Commonly, the heat generation in a single

tribological path might be ignored in the FEM modeling. Because it has been shown that the temperature rise caused by heat generation on many polymers under the ASTM standard scratch test is negligible [53,54]. The next part illustrates the modeling strategy and assumptions are made for each research subtopic.

II.1. Research Subtopic 1: FEM Modeling of Barrel Mar Behavior of Amorphous Polymers

II.1.1. Research objectives

As mentioned in the dissertation layout, FEM analysis for the mar damage is focused on Chapter III. However, the biggest issue for modeling mar behavior is that mar resistance could be only quantified through visibility analysis nowadays [29, 58]. However, visibility couldn't be calculated in numerical modeling. Furthermore, some parameters that affect the visibility of mar damage couldn't be considered in the FEM analysis, such as light conditions. Therefore, the first objective is to establish the correlation between the test and simulation by proposing some useful criteria in the FEM model for the quantitative assessment of mar performance. After that, the effect of material behaviors on mar performance is investigated with these criteria.

II.1.2. Research strategy

With the preference of the previous FEM modeling for scratch damage, a similar FEM approach has been chosen for the mar behavior simulation. The barrel head induced mar damage is investigated in the current study instead of sandpaper mar damage, since it still seems impossible to model the multiple micro-scratches involving 3-body abrasion

caused by random geometry particles on sandpaper. Also, although FEM modeling coupled with statistical analysis has been employed to model scratch damage on a polymer surface with a regular texture pattern [59], there is still a lack of a robust mapping method and mathematical representation for modeling on the polymer with irregular surface texture. Thus, only the elastic-plastic smooth surfaces without asperities will be considered for the present FEM mar behavior simulation.

To correlate with simulation, the uniform smooth matte surface requires to be prepared to generate barrel tip ironing mar in the experimental work. To do so, an embossing process on the model polymer systems was performed using a stainless steel plaque with $R_a = 3.24 \pm 0.07\ \mu m$, which was processed by an electron digital machining (EDM) treatment as shown in Figure II-2 [60]. Furthermore, three model amorphous polymethylmethacrylate (PMMA), polycarbonate (PC), and polystyrene (PS) samples were chosen as model systems, since their key material properties such as modulus, yield stress are very different from each other. This could be a benefit in the parametric analysis to correlate the mar performances to material properties.

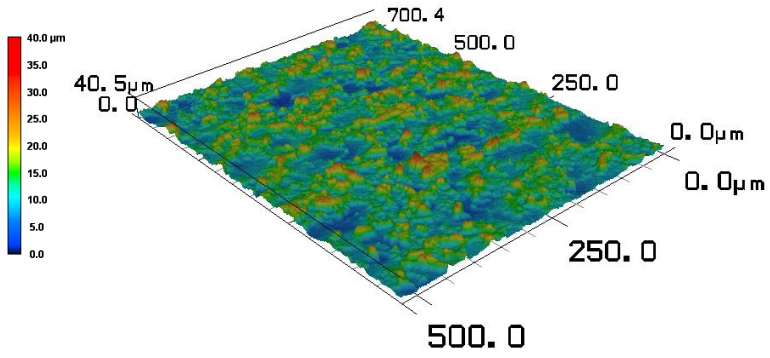

Figure II-2. Representative VLSCM image of EDM-processed stainless steel plate.

II.2. Research Subtopic 2: FEM Analysis on Scratch Induced Delamination Damage of Polymeric Multilayer Structures

II.2.1. Research objectives

Some previous research work has proven that scratch on polymeric multilayer systems is not only detrimental to the top surface but may also cause delamination between polymeric laminates [11, 12] due to the extremely high interfacial stress [61]. Therefore, the scratch test based on ASTM-D7027 could become an efficient testing methodology to evaluate the resistance of laminates to adhesive failure. One of the objectives in Chapter IV is to propose an approach that combines scratch test and FEM modeling to determine the delamination strength of multilayer polymeric systems. Furthermore, the stress state at the interface was analyzed via FEM analysis to provide the groundwork for a comprehensive in-depth study in Chapter V.

The research work in Chapter V answers why the resistance to scratch induced delamination and the interfacial failure mode in various types of polymeric laminates can be different [55, 62]. For example, it has been shown that a typical Mode II shearing-

dominated delamination occurs in the scratch test between the pentaerythritol triacrylate (PETA) top coating and trimethylolpropane ethoxylate triacrylate (TETA) base layer [55]. A mixed-mode delamination was observed between the blow-molded top polyethylene terephthalate layer and the adjacent nylon layer [61]. The difference in delamination mode and delamination resistance is often attributed to the constitutive properties and the respective thickness of each layer. However, only a few reports focus on actual adhesive failure between two layers. The 'delamination' mentioned in most previous FEM studies are actually cohesive failure of the tie layer [63, 64], instead of the debonding between two surfaces. For example, Wredenberg et al. implemented an interfacial cohesive zone into their FEM model to simulate the delamination of vinyl ester coating from the steel substrate [64]. However, the initiation and propagation criteria of the 'delamination' are quantified by the energy release rate (G) of the crack growing inside the tie layer, which indicates that their modeled 'delamination" is the cohesive fracture of the tie layer. Most previous scratch-induced delamination analyses focused on ceramic or metallic coatings as the model systems, like the Diamond-Like-Carbon (DLC) coatings and chemical vapor deposited (CVD) diamond coatings [12, 65, 66]. Unfortunately, those findings are not applicable to polymeric systems due to its more complex mechanical behaviors compared to metals and ceramics, such as strain-softening [67] and hydrostatic pressure dependent behavior [68, 69]. Furthermore, nearly all the research work focuses on investigating how the properties of the top layer laminate or coating affect the scratch induced delamination [12, 65, 66]. It has been shown that the constitutive behaviors of the base layer are equally important in affecting delamination behavior [61, 62]. For example, a blow-molded tri-

layer polymeric system with a PET base layer exhibits a higher delamination resistance than that with a nylon base layer, even though the top layer of both laminates are the same [61]. Therefore, it is necessary to carry out a fundamental study to understand how the delamination between the polymeric laminates is influenced by both top and base layer thicknesses and constitutive properties. Generally, Chapter V focuses on determining the effects of laminates' constitutive properties and thicknesses on scratch induced delamination behavior by conducting parametric study with an experimentally verified FEM modeling approach.

II.2.2. Research strategy

To understand the actual adhesive failure between two polymeric layers, cohesive zones approaches are not used. Instead, the stress distribution at the interface between two adjacent layers was analyzed via FEM modeling in this work. The current study is based on the tensile maximum principal stress criterion [70-72] for the onset of delamination, which means the delamination will only initiate when the peak tensile maximum principal stress (σ_1^t) at the interface reaches a critical value. Hence, the delamination resistance of the model systems can be assessed by comparing the development of the peak σ_1^t at the interface right before delamination. Furthermore, the direction of the peak σ_1^t at interface when delamination occurs can also reveal the failure mode. For example, a Mode I dominant delamination occurs when the direction of the peak σ_1^t at the interface is nearly perpendicular to the interface.

To simplify the problem, the model did not consider node separation and element deletion, temperature rise, heat generation, or time and temperature-dependent response

[73, 74]. However, the hydrostatic pressure dependent yield criterion needs to be included in the FEM model because the crack propagation of polymer is hydrostatic stress dependent [75, 76].

Furthermore, since there is still a lack of an appropriate FEM modeling approach to model the plowing damages, weakening the bonding strength by applying PTFE agent at the interface is to make delamination in scratch test takes place before the onset of unstable plowing damages. To validate the FEM model, a double-layer coating system made by the bisphenol-F based epoxy resin (D.E.R. 354 Dow Chemical) and Mannich based agent (D.E.H. 615 Dow Chemical) was chosen as model systems. Because it allows for the fast cure at room temperature to avoid uneven coating. A micrometer integrated film applicator was used to control the coating thickness accurately. To modify the constitutive properties of the epoxy coating, the different mount of Jeffamine® M1000 mono-amine was mixed with D.E.R. 354 epoxy resin and the D.E.H. 615 curing agent. The cross-linking density of the epoxy network is reduced because part of the epoxide groups reacts with the M1000 mono-amines [77].

II.3. Research Subtopic 3: Quantitative Modeling of Scratch Behavior of Amorphous Polymers at Elevated Temperatures

II.3.1. Research objectives

In the research scope section of Chapter I, the significance of developing the temperature dependent quantitative modeling approach has already been shown. Therefore, briefly, the objective of Chapter VI is to quantitatively predict the scratch-

induced deformation of amorphous polymers at elevated temperatures, but below T_g of the polymer.

II.3.2. Research strategy

As mentioned in Chapter I, Hossain et al. successfully introduced a numerical model for predicting the scratch-induced deformation of polycarbonate (PC) and styrene acrylonitrile (SAN) at room temperature by incorporating appropriate rate and pressure dependent constitutive models and frictional behaviors [8]. However, this approach cannot be used to predict the scratch performance of polymers as a function of temperature. One of the assumptions involved in their study is that the strain rate would not affect strain softening and hardening behaviors of PC and SAN. Therefore, the post-yield behavior at various strain rates was estimated by simply shifting the post-yield stress-strain curve measured in a quasi-static state to the yield point at different strain rates [8]. Unfortunately, this stress-strain curve shifting would not be appropriate if the post-yielding behavior of the polymer is also affected by temperature. To overcome this drawback, a temperature-strain rate-dependent constitutive model, namely the Arruda-Boyce viscoplastic model, was employed to describe the post-yield behavior at various conditions [9]. Although the above model is semi-empirical, this has been successfully applied to determine the tensile and compressive behaviors of amorphous polymers, such as polymethyl methacrylate (PMMA), PC, and even semi-crystalline thermoplastic olefins [78-82].

One limitation of the Arruda-Boyce viscoplastic model is its inaccurate prediction of the polymer yield stress, especially at high strain rates [78, 83]. A previous parametric

analysis showed that yield stress has a significant influence on scratch behavior [6, 84]. Even a small difference in yield stress like 15 MPa will induce conspicuous changes in scratch groove dimensions [6]. Therefore, an accurate prediction of this parameter is necessary for quantitative analysis. The yield stress was previously predicted using Bauwens-Crowet's approach and Ree-Eyring theory [46, 85]. Based on Bauwens-Crowet's work, the curves showing the relationship of yield stress versus temperature or strain rate can be divided into three zones, as shown in Figure II-3 [86]. At high temperatures or low strain rates (Range I), the yield stress of amorphous polymers can be assumed to mainly relate to a single molecular backbone activation process, α process. While at low temperatures or high strain rates (Range I'), an additional energy process, β process, is required to supply the activation of frozen molecular movement besides the α process [87]. Hence, Range I' is an activation process combining the α+β processes. However, between Range I and Range I', there is a transition range without equations describing the relations between yield stress and temperature/strain rates [86], which results in the inaccurate yield stress prediction in the transition region, especially $|\sigma_c|$ as shown in Figure II-3.

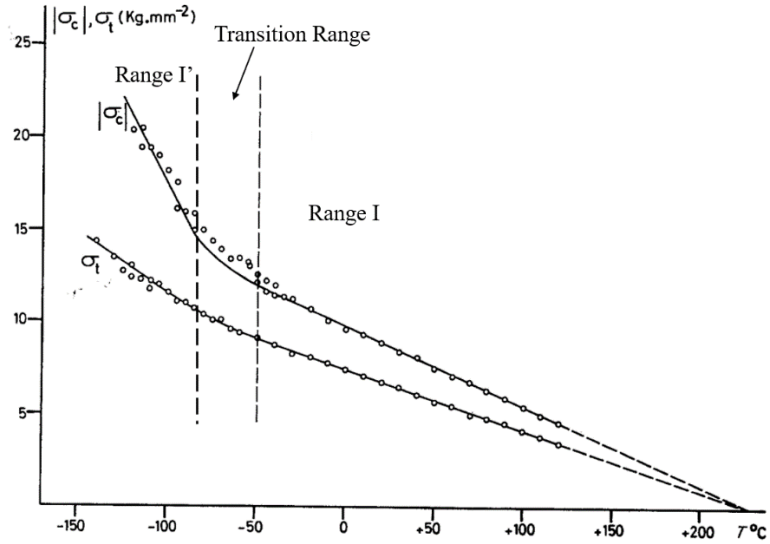

Figure II-3. Uniaxial compressive ($|\sigma_c|$) and tensile σ_t yield stress of Polycarbonate (PC) versus temperature at a constant strain rate 4.16× 10^{-3} /*s*. Reprinted from Bauwens-Crowet et al. [86].

From the previous studies, the average effective strain rate near the scratch groove of PC was estimated to be 480/s with Equation (II-1) [88], where v is the scratch testing speed of 100 mm/s and w is the width of the scratch groove. By using Equation (II-2), the position of the transition region in the yield stress versus temperature plot at a constant strain rate of 480/s was approximated as 101°C [86], which means that the transition is below the T_g of PC (T_g ~148°C). Q_β is the activation energy and C_β is a material constant of the β activation process. The Q_β and C_β of PC are respectively 9.6 $kcal/mol$ and $2.76 \times 10^{-9}\ s$, from Bauwens and Crowet's work [87]. R is the gas constant 8.31446 $J \cdot K^{-1} \cdot mol^{-1}$.

$$\dot{\varepsilon} = \frac{v}{w} \tag{II-1}$$

$$T_\beta = -\frac{Q_\beta}{R \ln 2 C_\beta \dot{\varepsilon}} \tag{II-2}$$

However, there is no equation for yield stress prediction in this transitional regime. Therefore, the Bauwens-Crowet's approach has limited capabilities for predicting the yield stress of amorphous polymers at high strain rates, and the temperature range around T_β below T_g. To overcome this issue, Richeton et al. developed a cooperative model to predict the yield stress of amorphous polymers in a wide range of strain rates and temperatures based on the Eyring theory [89]. By considering the cooperative movements of the polymer chain segments and the structural change of amorphous state due to thermal history, Richeton's model has been found to predict the yield stress of amorphous polymers as a function of temperature and strain rate more accurately than the previous models [90, 91].

Other than the temperature effect, the contact behavior between the scratch tip and substrate also has a significant effect on the scratch resistance of polymeric surfaces [38, 92, 93]. The evolution of friction during the scratch process needs to be carefully considered in the contact model. Hossain et. al introduced a pressure-dependent coefficient of friction (COF) of PC and SAN determined by simulated shear strength. This was useful for modeling the effect of pressure on the contact behavior during the scratch test [46]. It has to be noted that COF is highly dependent on temperature [94, 95]. Therefore, for quantitative modeling of scratch-induced deformation at various temperatures, the effect of temperature on COF should be considered.

Based on the research objectives and strategies illustrated above, the experimental and FEM modeling work of each subtopic was demonstrated in the following chapters from Chapter III to Chapter VI.

CHAPTER III

EXPERIMENTAL AND FEM ANALYSIS OF BARREL MAR BEHAVIOR OF AMORPHOUS POLYMERS*

III.1. Experimentals

III.1.1. Model systems

The model amorphous polymers investigated in this study consist of commercialized PMMA (Plexiglas® V052), PC (Makrolon 2800), and PS (Polystyrol 158K) materials prepared using the injection molding process. Their melt flow rates and glass transition temperatures (T_g) are presented in Table III-1. Each system has dimensions of 150 mm × 150 mm × 3 mm and 150 mm × 150 mm × 6 mm for various mechanical characterization needs. PMMA samples were provided by Arkema Inc (King of Prussia, USA), while PC and PS samples were provided by BASF SE (Ludwigshafen, Germany). To obtain more consistent mar results, all the samples have high gloss piano black color and similar surface roughness.

Table III-1. Melt flow rate and glass transition temperature (T_g) of the model systems.

	Melt Flow Rate (cm^3/10 min)	T_g (°C)	(R_a)
PMMA	2.4 (@ 230 °C, 3.8 kg)	116	$36 \pm 3\ nm$
PC	10 (@ 300 °C, 1.2 kg)	148	
PS	3.5 (@ 200 °C, 5 kg)	100	

* Part of this chapter was reprinted from Wear, 444-445, Du, S., Hamdi, M., Sue, H.-J., Experimental and FEM analysis of mar behavior on amorphous polymers, 203155, Copyright (2020), with permission from Elsevier.

III.1.2. Surface roughness embossing

The original surface roughness values of the model systems are $(R_a)_{initial} = 36 \pm 3\ nm$. It is difficult to investigate mar-induced ironing damage on such considerably smooth surfaces. Therefore, it is crucial to modify the surface roughness of the model samples in a consistent fashion without affecting their bulk properties. It has been found that embossing is a reliable process to achieve consistent nanometer to micrometer scale surface roughness in a repeatable fashion. Consequently, a stainless steel plaque processed by an electron digital machining (EDM) with a surface roughness of $R_a = 3.24 \pm 0.07\ \mu m$ was used to emboss similar surface roughness values on the model systems. The samples were compressed for 30 minutes using a PHI hydraulic press at a pressure of 1.3 MPa and a temperature that is 10°C above the T_g of the embossed polymer. Then, the samples were left to cool in the hot press until reaching ambient temperature.

III.1.3. Surface roughness characterization

A Keyence VK9700 Violet Laser Scanning Confocal Microscope (VLSCM) was employed to measure the surface roughness of the embossed samples [96]. Measurements were taken on an embossing steel surface, the embossed model systems, and on the marred paths of the samples at distances of 10 (~15 N), 30 (~42 N), 50 (~75 N), 70 (~112 N), and 90 mm (~154 N) from the origin. At each location, the measurements were conducted at five random nearby locations over an area of $675 \times 506\ \mu m$ using a 20x objective lens. A representative VLSCM image showing the roughness of embossed stainless steel is shown in Figure II-2.

III.1.4. Mar test

Mar tests were conducted according to ASTM D7027 / ISO 19252 standards [97, 98] using Scratch 5 Machine provided by Surface Machine Systems® (College Station, TX). Barrel mar tests were performed using a self-aligned stainless steel barrel tip (Figure III-1) with a length of 12 mm and a diameter of 10 mm. The test consists of applying a normal load linearly increasing from 1 to 180 N along the injection molding direction at a constant speed of 10 mm/s over a distance of 100 mm. To obtain consistent results, at least three mar tests were carried out on each material. The load range was chosen to make the mar of the model systems visible enough for assessment and analysis.

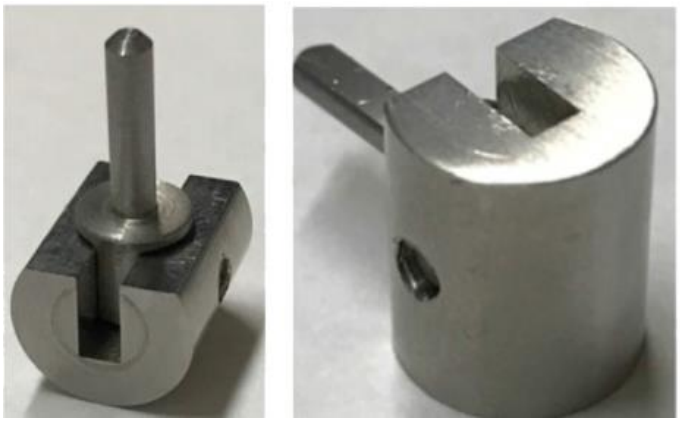

Figure III-1. Self-aligned stainless-steel barrel tip used for mar test. Reprinted from Chrisman et al. [29].

III.1.5. Coefficient of friction (COF)

The global coefficients of friction (COF) of the embossed samples were determined by sliding a smooth stainless steel flat tip with dimensions of $10\,mm\,\times$

10 mm. A constant normal load of 3 N was applied over a distance of 100 mm at a speed of 10 mm/s. Five measurements were performed on each sample.

III.1.6. Mar visibility evaluation

The visibility of the marred samples was evaluated according to the procedure described in the previous study [25, 26, 29]. Samples were placed in a Black Box with dimensions of 690 mm × 430 mm × 690 mm provided by Surface Machine Systems®. Preliminary tests showed that the observation angle should be set to 90° and the angle between the camera and the light source should be set to 50° to maximize the darkening effect caused by the ironing process. Then, mar images were analyzed using Tribometric® software provided by Surface Machine Systems®. This software generates a contrast curve showing the contrast value between mar area and virgin background of the sample as a function of the applied mar load. Figure III-2 shows the areas utilized for mar visibility evaluation, which consists of a green box capturing mar area and two surrounding white boxes indicate the background of the sample surface. The distance between the mar area and each of the background areas is 0.5 mm. At each pixel, the contrast value was determined using Equation (III-1):

$$Contrast\ (\%) = \frac{(I_m)^{1/\gamma} - (I_b)^{1/\gamma}}{(I_{max})^{1/\gamma}} \quad \text{(III-1)}$$

Where I_m refers median brightness of the pixel line (blue area in Figure III-2) in the mar path. I_b refer the intensity of background, determined by the median grayscale value of two $2\,mm \times 0.5\,mm$ areas in yellow boxes. I_{max} is the maximum captured

intensity along the whole mar path. γ refers to the power-law scaling factor to normalize color intensity values.

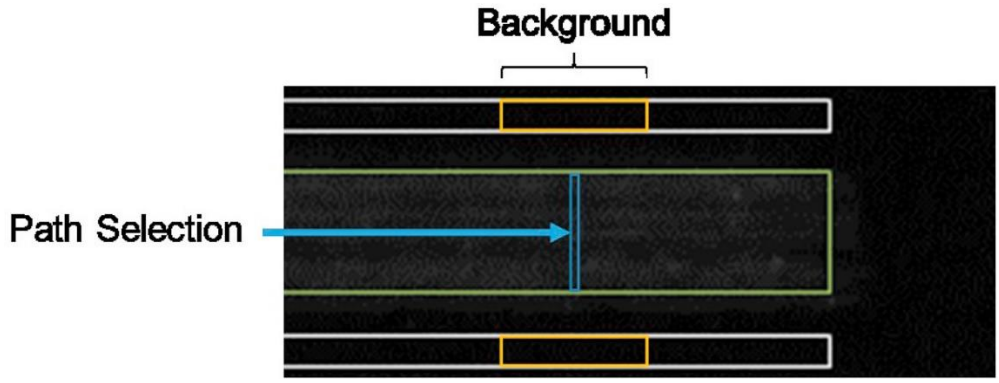

Figure III-2. Areas utilized for mar visibility Evaluation. Reprinted from Chrisman et al. [29]

III.1.7. Human observation procedure

Ten trained participants were involved in the human visibility assessment described previously [29, 58]. The test was conducted in a dark room to avoid background interference. Each of the participants was separately asked to rank the mar severity from 1 to 10, with 10 referring to the most visible mar. No information about the model system and testing conditions were notified to participants during the procedure.

III.2. FEM Modeling

III.2.1. FEM model

The commercial finite element package ABAQUS 2017® was employed to perform the FEM modeling of the mar tests [99]. The dimensions and boundary conditions of the model are presented in Figure III-3 [43, 61]. The mar tip was modeled as a rigid

cylindrical body with a diameter of 1 mm, an edge of 1 mm, and a spherical side with a diameter of 1 mm to suppress the stress singularities caused by the edge effect.

Eight-node 3D linear brick elements (C3D8R) with three nodal displacement degrees of freedom and reduced integration were considered to mesh the substrate. A refined mesh with element dimension $46.5\ \mu m \times 56.2\ \mu m \times 30.0\ \mu m$ was considered beneath the mar tip across a critical distance A-B for better computational performance and computational efficiency [39, 49]. Also, dynamic stress analysis and adaptive remeshing provided by ABAQUS were utilized in our model to preserve the mesh quality and avoid excessive distortion of the elements [43, 99].

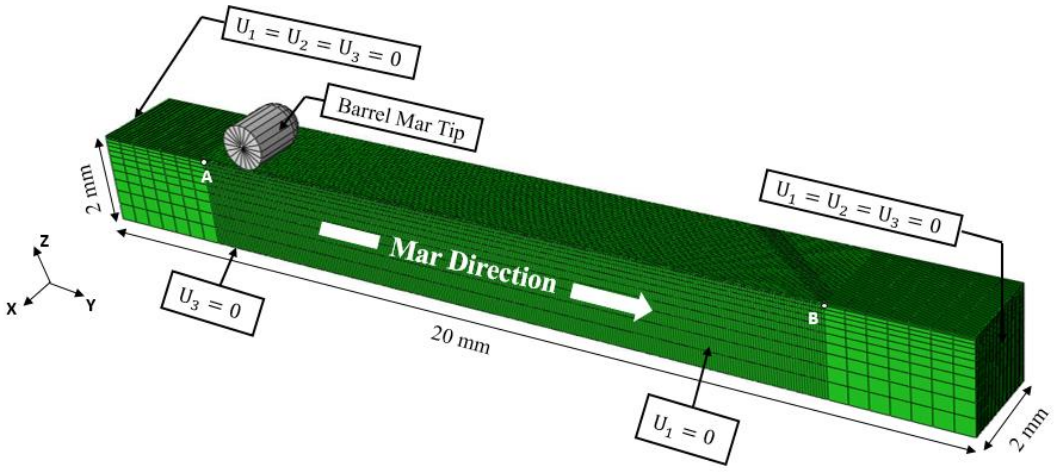

Figure III-3. 3D finite element analysis model with the boundary conditions described.

III.2.2. Mar simulation

The mar test was modeled in accordance with the same ASTM/ISO standards [97, 98]. The model did not consider elements separation and removal after damage, heat generation, and time and temperature-dependent response for simplification purposes. The first step is the indention test where the rigid mar tip moves down with an applied load of 0.5 N and maintains contact with the surface. Then, the mar process takes place and the tip slides over a distance of 12 mm with a speed of 10 m/s and a linearly increasing load from 0.5 to 50 N. The mar direction is indicated in Figure III-3. The friction of $\mu = 0.3$ was considered between the tip and the substrate. This is roughly the COF value of the roughened materials measured experimentally as will be shown later. Finally, the tip stops at the end of the mar distance and moves upward allowing for material elastic recovery. The FEM model methodology used in the present study including the same constitutive model, boundary conditions, and mesh size has been verified by previous single-path tribological studies [5, 6, 43].

III.2.3. Material properties

The 3D constitutive models such as BPA (Boyce-Parks-Argon) model [59, 79, 100, 101] and the EGP (Eindhoven Glassy Polymer) model [102-104] have been demonstrated with the good capability to model the temperature and strain rate dependent compressive behavior of PC and PMMA. However, to perform a meaningful parametric study and to identify the most relevant material parameters that affect mar behavior where the tensile behavior is also important, a simplified isotropic hardening model coupled with the experimentally obtained tensile and compressive true stress-strain curves were chosen

to generate piece-wise linear curves for all the FEM modeling needs (Figure III-4) for the FEM simulation [6]. These experimentally generated constitutive relations were found to be sufficient in capturing the mar behavior differences among the three model systems Also, previous work showed that the viscoelastic recovery of PC and SAN following the scratch test is limited and can be ignored [46]. In order to further simplify the simulation, PC, PMMA, and PS were assumed to be elastic-plastic materials without considering temperature and rate dependent behavior. The main constitutive parameters are Young's modulus (E), yield stress (σ_y), softening slope (s), and hardening slope (h). The values of these parameters, as well as the density (ρ), of the modeled materials are summarized in Table III-2 [6].

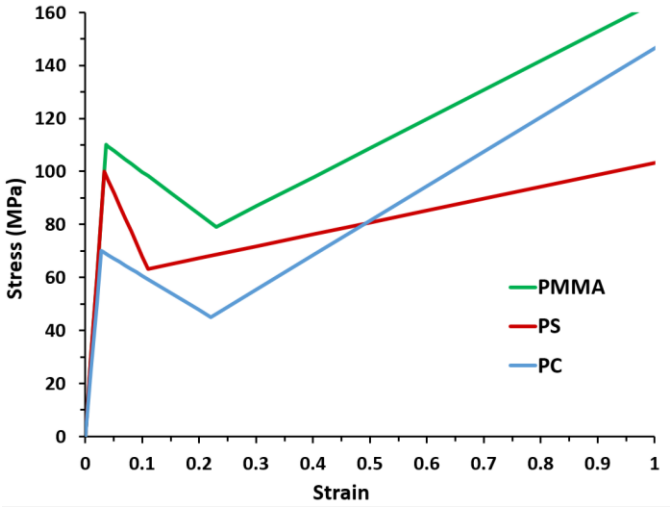

Figure III-4. Typical piece-wise linear stress-strain curve of PMMA, PC, and PS for FEM modeling.

Table III-2 Constitutive parameters introduced in the FEM model.

Model System	E (GPa)	σ_y (MPa)	s (MPa)	h (MPa)	ρ (g/cm^3)
PMMA	3	110	-160	110	1.18
PC	2.5	70	-130	130	1.20
PS	3	100	-480	45	1.04

III.2.4. Parametric study

The impact of each of the constitutive parameters presented in Table III-2 on the mar behavior is investigated separately by conducting a parametric analysis. Each of these parameters will be exclusively varied in the range of the model polymers investigated while maintaining the linear piece-wise stress-strain curves of the model systems. The values of fixed and varying parameters for each case study are highlighted in Figure III-5. It should be noted that the yield strain (ε_y) is slightly changed when altering elastic modulus or yield stress.

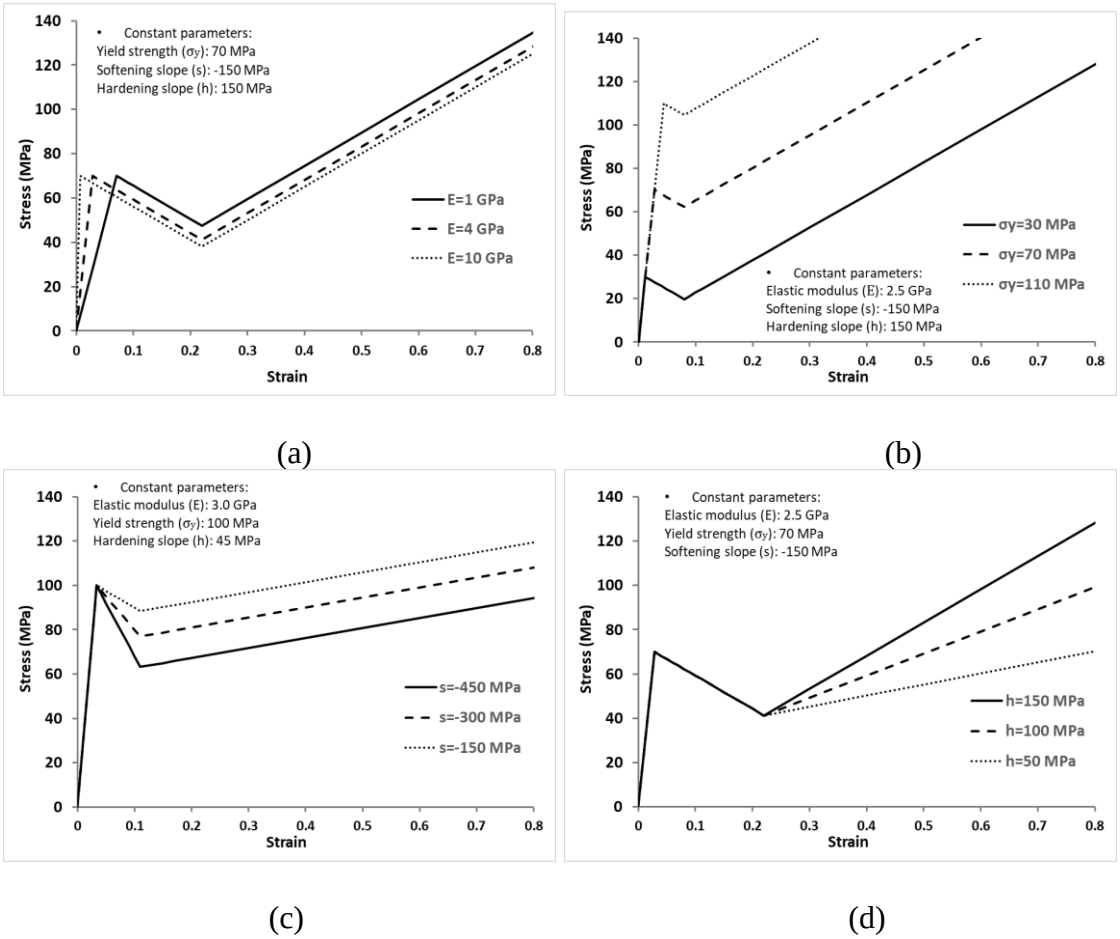

Figure III-5. Fixed and varying constitutive parameters considered in the parametric study (a) elastic modulus (b) yield stress (c) strain softening slope, and (d) strain hardening slope.

III.3. Results and Discussion

III.3.1. Experimental results

The surface coefficient of friction and root-mean-square (RMS) roughness (Rq) of the examined model systems are presented in Figure III-6. It is observed that the samples have similar COF and Rq values. Therefore, the difference in mar behavior to be discussed

later will be mainly attributed to their respective constitutive behaviors, instead of these two factors [105].

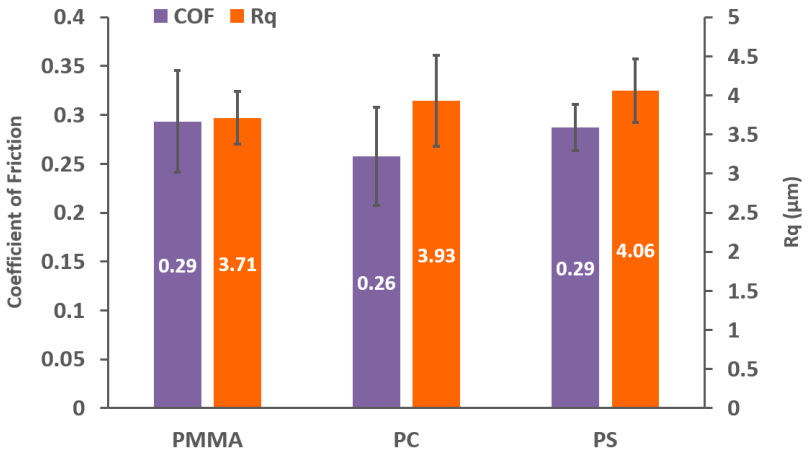

Figure III-6. Surface coefficient of friction and roughness of the model systems**.**

Figure III-7 presents the contrast curves along the mar path and the absolute integral area beneath them for each of the model systems. Figure III-7 (a) shows the representative contrast curves obtained by a moving average of 20 consecutive points to highlight the relative visibility. Also, the negative contrast values in this figure indicate the ironing effect due to the reduction in surface roughness, which makes mar damage to appear darker than the background [26, 106]. The contrast values of the three systems are about zero below 50 N mar load. It might due to the very low plastic deformation [107]. It was previously shown that the integrated area under the contrast curve is a straightforward way to quantify and compare the mar visibility resistance of polymers [105]. Higher integrated area is associated with lower mar visibility resistance. Figure III-7

(b) shows that PMMA has the lowest area beneath the contrast curve. Thus, this material is expected to have the highest mar visibility resistance. The integral area beneath PC contrast curve is slightly smaller than that of the PS. This indicates that these two materials have similar mar visibility resistance, with PS having a lower mar resistance.

To validate their mar performance, the contrast-based findings presented above are compared with the human assessment results shown in Figure III-8. The participants in the human assessment ranked mar damage on PMMA samples as the least visible, followed by that for PC which is ranked slightly lower than PS. These results are in good agreement with the findings of the contrast analysis presented in Figure III-7 (b).

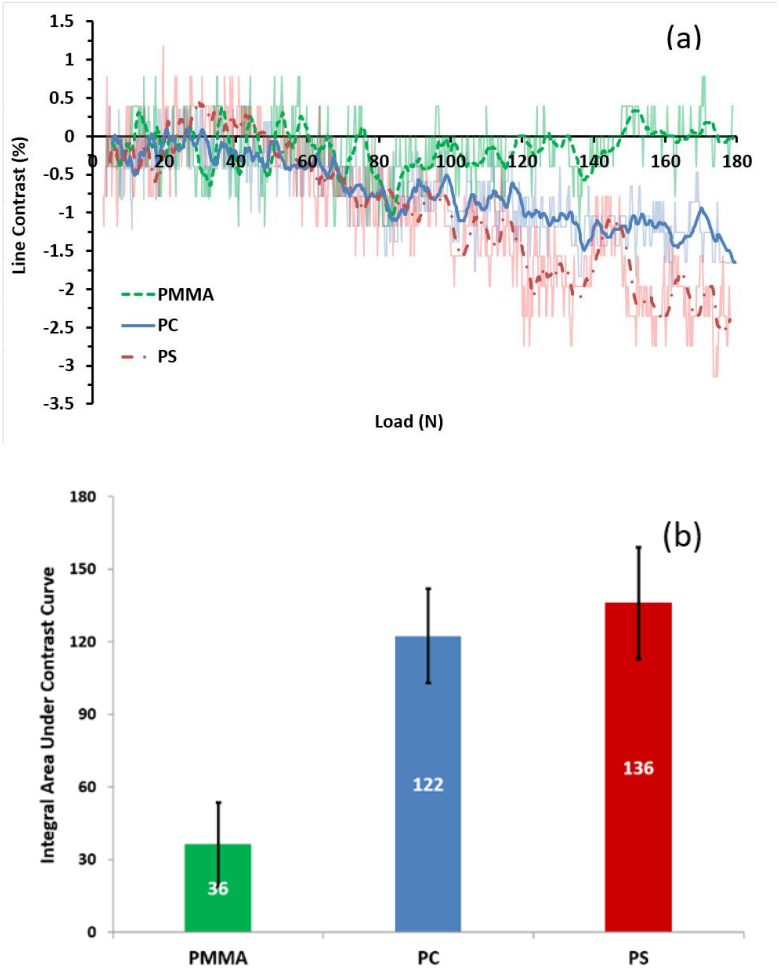

Figure III-7. PMMA, PC, and PS (a) contrast curves and (b) absolute integral area under them.

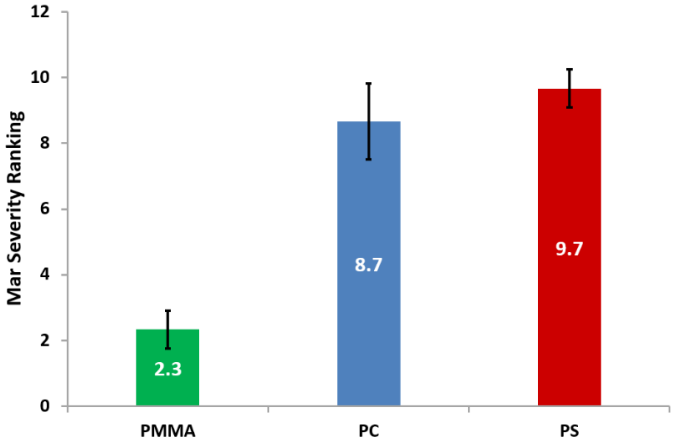

Figure III-8. Ranking of mar visibility on the model systems.

As mentioned previously, no cracking or crazing damages were observed on the mar area. Therefore, the detected subtle mar damage is mainly associated with the surface roughness changes. This effect can be studied using the percent change in surface roughness ($\Delta R_q\%$) given by Equation below:

$$\Delta Rq\% = \frac{Rq(Marred) - Rq_0(Virgin)}{Rq_0(Virgin)} \times 100\% \quad \text{(III-2)}$$

Figure III-9 shows the values of $\Delta R_q\%$ at different mar loads along the mar path. The negative value of this parameter signifies the ironing effect where the marred area is smoother than the background of the samples. A larger absolute $\Delta R_q\%$ value demonstrates a more severe ironing effect due to the barrel mar process. As mentioned above, the severity of the ironing effect correlates well with visibility. The figure clearly shows that PMMA has the least absolute $\Delta R_q\%$ value across the mar path which indicates its high mar visibility resistance. The two other materials, PC and PS, have similarly higher absolute $\Delta R_q\%$ values reflecting their low mar resistance with consideration of standard derivation. But it should be noted that the average absolute $\Delta R_q\%$ value of PC is higher than PS before about 55 N, while the trend reverses after that, which is probably due to the significantly higher strain hardening behavior of PC at large-strain region [108]. These results are consistent with the contrast analysis shown in Figure III-7 and the human assessment presented in Figure III-8.

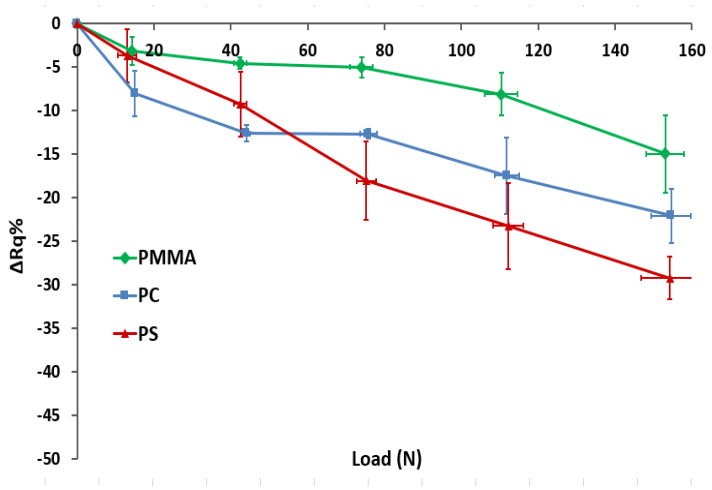

Figure III-9. Difference in roughness between mar area and sample background along the mar path.

III.3.2. Finite element modeling results

One of the major differences between mar simulation comparing to scratch simulation is the presence of the edge effect, an extremely high localized stress or strain concentration shown in FEM calculations caused by the barrel shape of mar tip. To avoid these effects, a middle area of the mar path in white rectangular (0.8 mm × 11 mm) is considered for analysis as shown in Figure III-10.

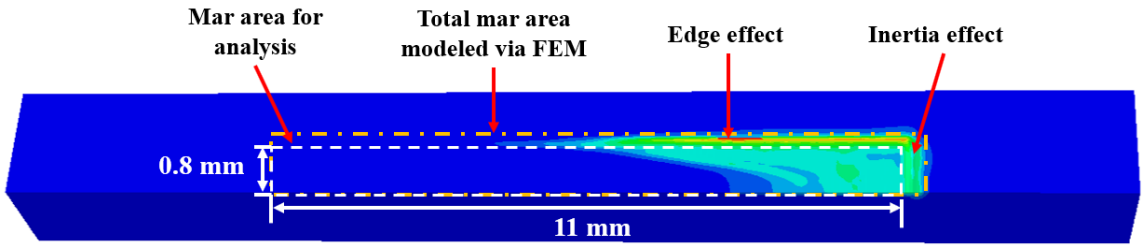

Figure III-10. Considered area for mar analysis.

Due to the fact that both the experimental and FEM simulation methodologies have been verified in previous studies [5, 6, 29, 43], the following analysis was directly conducted and results were discussed.

III.3.2.1. Stress analysis

Due to the barrel tip and inertia effects, the stress distribution on mar surface is different from that of scratch [9, 39]. The distributions of maximum principal stress (σ_1) on PC at different mar loads are shown in Figure III-11. At a low mar load of 11 N, tensile and compressive stresses dominate at the edge and beneath the mar tip, respectively (Figure III-11 (a)). As the applied normal load increases, the stress near the edge becomes more severe, and high tensile stress is generated behind the mar tip (Figure III-11 (b), (c)), which is similar to previous scratch simulations [9]. This may indicate the formation of plastic yielding-related damage and meniscus wrinkling on the mar path.

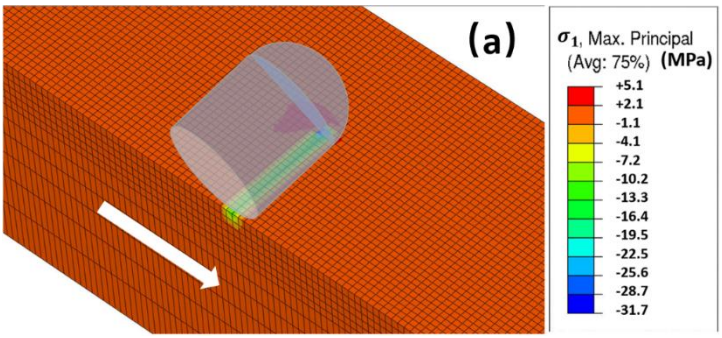

Figure III-11. Maximum principal stress σ_1 on PC at mar loads of (a) 11 N, (b) 34 N, and (c) 48 N.

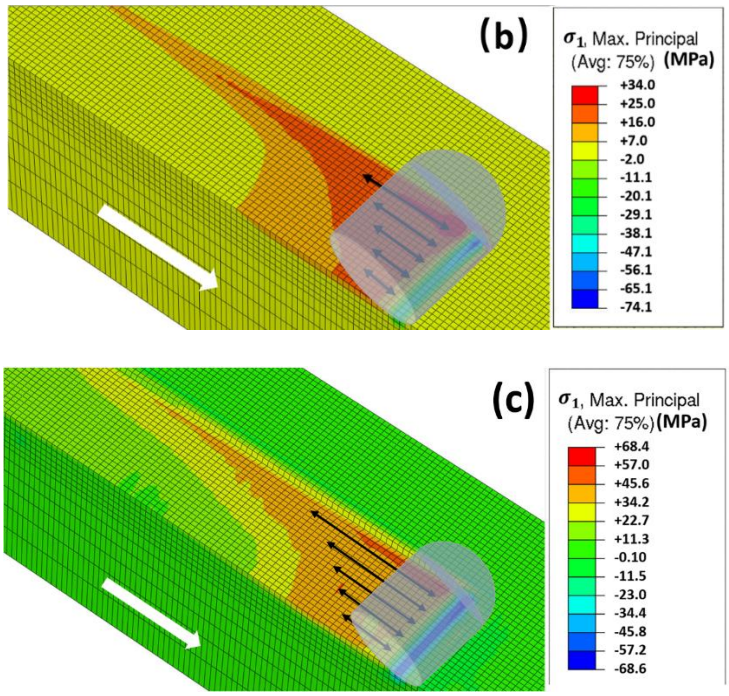

Figure III-11. Continued.

The main objective of the FEM modeling is to conduct a parametric analysis that allows the determination of the effect of different constitutive properties on mar resistance. However, it is crucial first to determine a parameter that can be used as a criterion to assess mar damage resistance. The parameters considered for this purpose are the maximum plastic principal strain (ε_1^p), maximum principal stress (σ_1), von Mises stress (σ_v), hydrostatic pressure (σ_p), and total plastic energy dissipation (E_p) [43, 109].

III.3.2.2. Mar assessment criteria

Maximum plastic principal strain (ε_1^p): Figure III-12 shows the distribution of ε_1^p across the mar path of the three materials after the elastic recovery. The mar direction is from left to right. The figure shows that PMMA exhibits much lower ε_1^p than PS and

PC in terms of distribution and intensity. The magnitude of ε_1^p is most significant on PS. These results are in good agreement with the experimental (Figure III-7) and human assessment findings (Figure III-8). They indicate that ε_1^p can be used as a criterion to assess mar damage resistance. This result can be explained by the mar-induced ironing effect being plastic deformation in nature, which makes the plastic principle strain a good criterion.

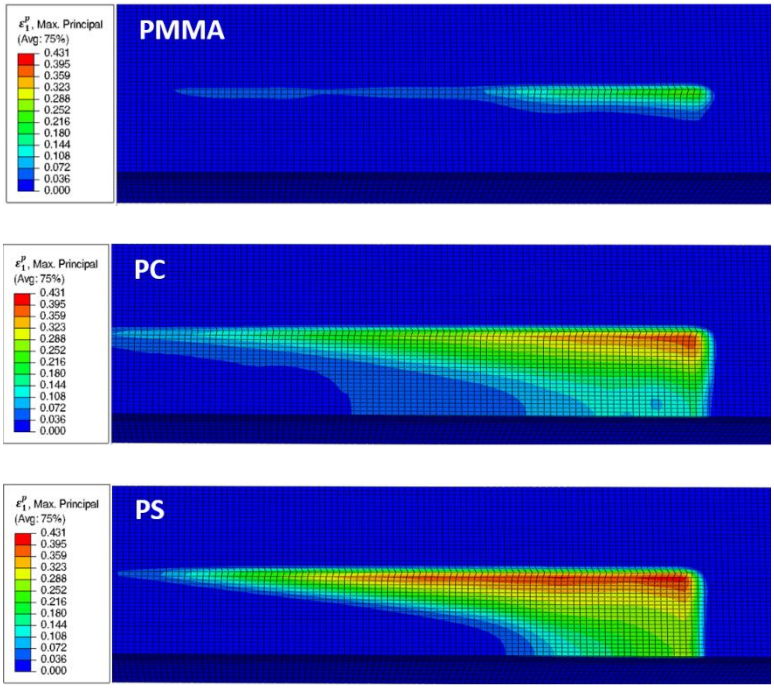

Figure III-12. The contour plots of maximum plastic principal strain ($\varepsilon^p{}_1$) across the mar path of the modeled materials.

Maximum principal stress (σ_1): Figure III-13 shows the contours of σ_1 across the mar path of the model polymers after the elastic recovery. The figure highlights that

PMMA has the lowest σ_1 level. However, it shows a higher σ_1 intensity and magnitude on PC compared to PS. These results are inconsistent with the previous experimental findings and human assessment, showing that PC is ranked between PMMA and PS in terms of mar visibility resistance. Therefore, this parameter fails as a criterion for ranking mar damage resistance on the examined materials.

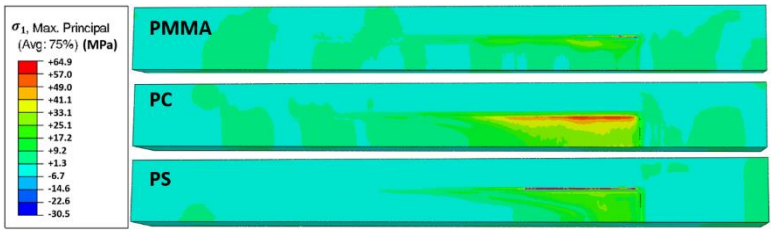

Figure III-13. The contour plots of residual maximum principal stress σ_1 on the mar path of the modeled materials.

Von Mises stress (σ_v): Previous studies showed that von Mises stress was related to the onset of shear banding in polymers [110, 111]. Figure III-14 highlights the σ_v contour plot across the mar path of the modeled materials. The figure shows that PMMA has the lowest values and PC exhibits higher values than PS, especially at the mar end. This parameter does not correlate well with the previous contrast-based analysis and human assessment. Therefore, σ_v fails as a criterion to reliably rank mar damage resistance on the examined samples. This finding suggests that the mar damage on the examined materials is not dominated by plastic yielding.

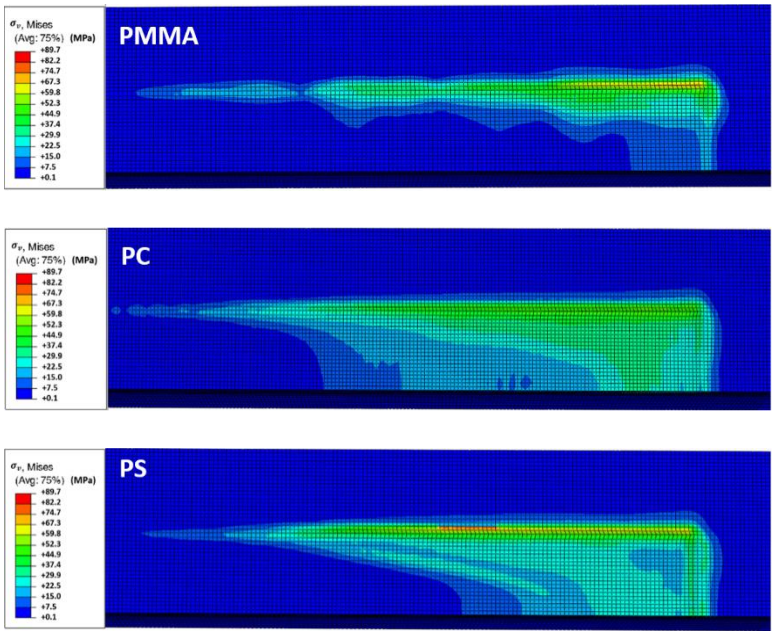

Figure III-14. The contour plots of von-Mises stress σ_v on the mar path of the modeled materials.

Hydrostatic pressure (σ_p): σ_p is known to be related to any damage mechanisms involving volume change, such as cracking, crazing, and voiding [112]. Figure III-15 shows the contour plots on the surface of the model polymers. It is clearly shown that PMMA exhibits a much lower σ_p than PC and PS. The experimental and human assessment results show that PMMA has the best mar visibility resistance. This suggests that a lower hydrostatic pressure corresponds to a higher mar resistance. However, σ_p magnitude on PC is higher than that on PS which contradicts the experimental and human assessment findings. Therefore, the hydrostatic pressure fails as a criterion to assess the mar resistance of the examined samples. This suggests that mar damage on the tested materials is not dominated by mechanisms involving volume changes.

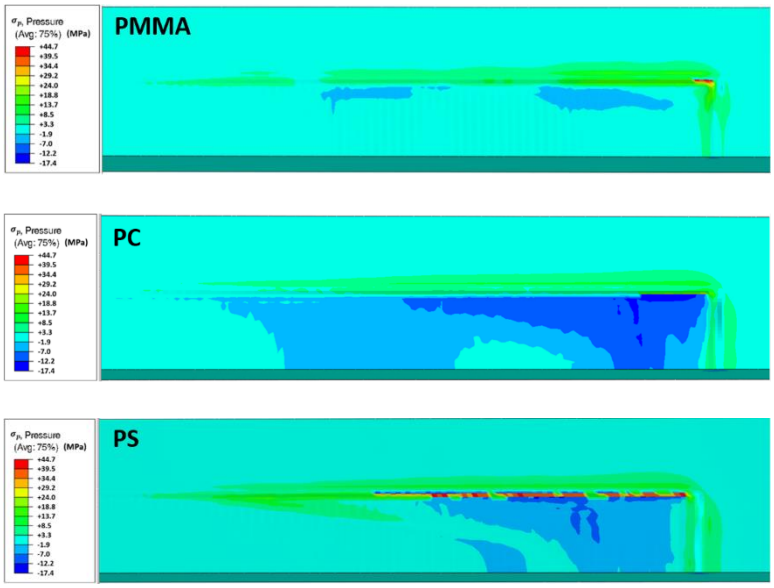

Figure III-15. The contour plots of the hydrostatic pressure σ_p on the mar path of the modeled materials.

Total dissipated plastic energy (E_p): The energy conservation principle is highlighted by Equations (III-3) and (III-4) below. For simplicity, this principle does not consider temperature- and time-dependent deformations. It indicates that the kinetic energy (E_w) on the mar tip is approximated by the summation of the dissipated frictional energy (E_f) and the internal energy stored in the polymer substrate (E_I) [99]. The barrel mar tip is modeled as an analytical rigid solid without internal energy. The value of E_I includes the elastic strain energy, E_s, and that dissipated by plastic mar deformation, E_p.

$$E_w \approx E_f + E_I \quad \text{(III-3)}$$

$$E_I = E_s + E_p \quad \text{(III-4)}$$

Figure III-16 shows E_p values obtained from the mar area on PMMA, PC, and PS. It is found that PMMA has the lowest E_p value, and that PC has slightly lower dissipated energy than PS. These results correlate well with the experimental findings (Figure III-7) and human assessment (Figure III-8). Therefore, the total dissipated plastic energy can be considered as a criterion to effectively evaluate the mar resistance of the studied materials.

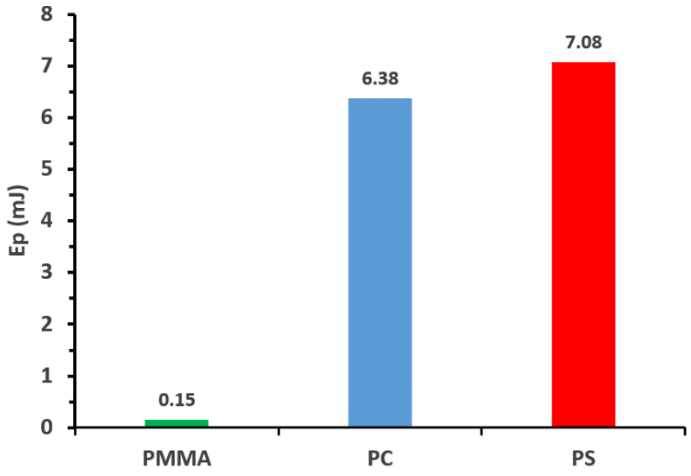

Figure III-16. Total dissipated plastic energy (E_p) of the modeled materials.

FEM results show that the maximum plastic principal strain (ε_1^p) and the total dissipated plastic energy (E_p) are the most likely parameters that can be chosen to predict the mar visibility resistance of polymers. Higher mar resistance corresponds to lower ε_1^p and E_p values. These two criteria will be used in the parametric study to determine how the constitutive properties influence mar visibility resistance of polymers [54].

III.3.2.3. Parametric study

The parameters involved in the parametric analysis are elastic modulus (E), yield stress (σ_y), strain softening (s), and strain hardening (h). The surface COF is not included in this analysis because it has already been demonstrated that higher COF results in lower mar resistance [4, 113].

Elastic modulus (E): Table III-2 shows that the examined materials have similar elastic modulus values. Therefore, this property is not expected to affect the difference in their mar resistance. However, other materials may have significantly different modulus values and should be addressed. Figure III-17 shows the effect of the elastic modulus on the maximum plastic principal strain and total dissipated plastic energy. It is found that a higher modulus leads to a higher ε_1^p and higher E_p values, thus a lower mar resistance.

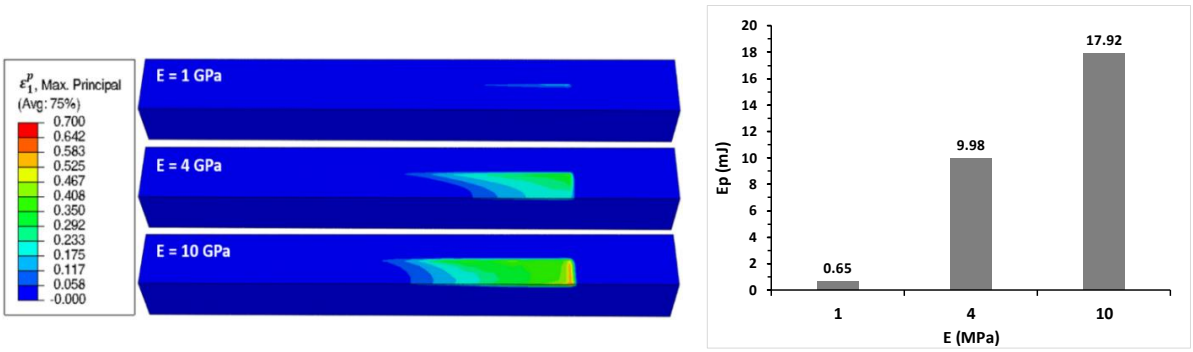

(a) (b)

Figure III-17. Effect of elastic modulus (E) on (a) maximum plastic principal strain $\varepsilon^p{}_1$ distribution and (b) total dissipated plastic energy E_p.

Yield stress (σ_y): Similarly, the impact of yield stress on ε_1^p and E_p contour plots after recovery are presented in Figure III-18. The figure shows that a higher yield stress corresponds to a significantly lower ε_1^p and $E_p$values. Since lower ε_1^p and E_p values are associated with higher mar resistance, this result implies that a higher yield stress corresponds to a higher mar resistance.

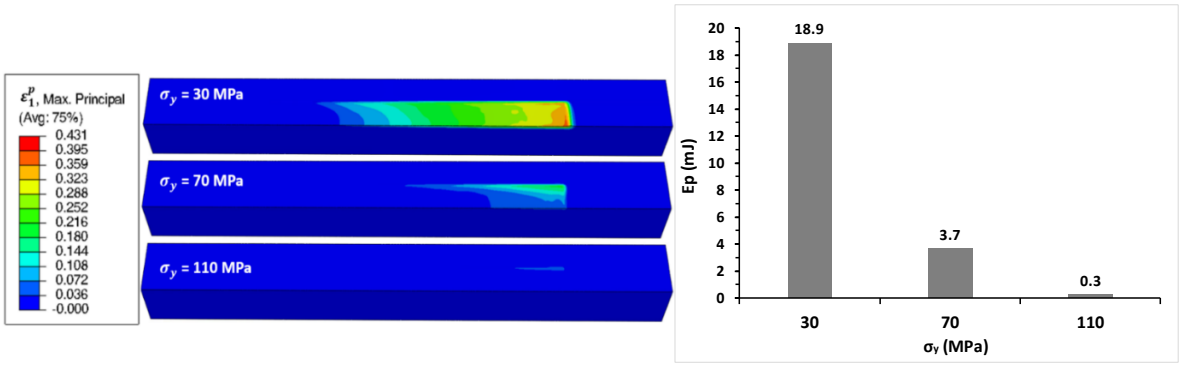

(a) (b)

Figure III-18. Effect of yield stress (σ_y) on (a) maximum plastic principal strain $\varepsilon^p{}_1$ distribution and (b) total dissipated plastic energy E_p.

Strain softening (s): Likewise, Figure III-19 shows the effect of strain softening slope on ε_1^p and E_p. It is observed that a higher softening slope leads to a higher ε_1^p and E_p values. This suggests that higher slope corresponds to lower mar visibility resistance.

It is crucial to point out the impact of strain rate on strain softening. Strain softening is associated with localized inhomogeneous deformation which makes it more dependent on the strain rate [67]. When the strain rate is slow enough, the strain softening

phenomenon from uniaxial tensile or compression test would disappear [109]. Hence, the strain softening of amorphous polymers measured by quasi-static uniaxial compression or tension tests may become more pronounced because of the much higher strain rate expected during the mar tests [4].

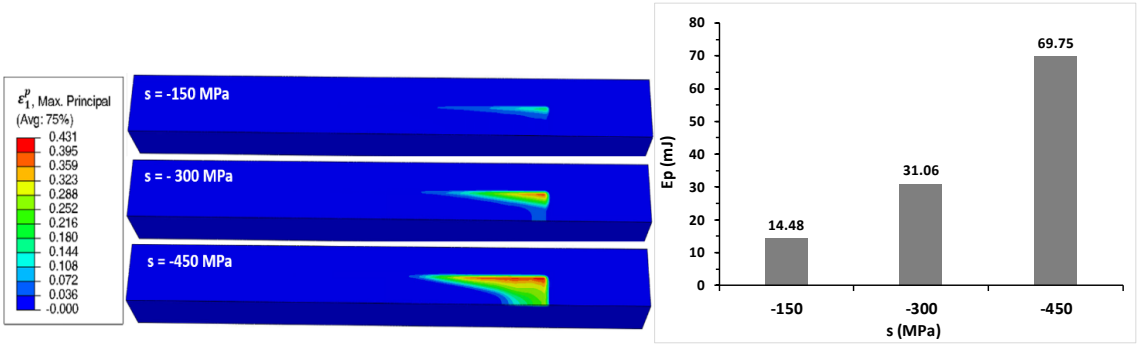

(a) (b)

Figure III-19. Effect of strain softening slope (s) on (a) maximum plastic principal strain $\varepsilon^{p}{}_{1}$ distribution and (b) total dissipated plastic energy E_p.

Strain hardening (h): Figure III-20 highlights the effect of strain hardening slope (h) on ε_1^p and E_p. It is found that a higher strain hardening is associated with a lower ε_1^p and E_p, thus a higher mar resistance.

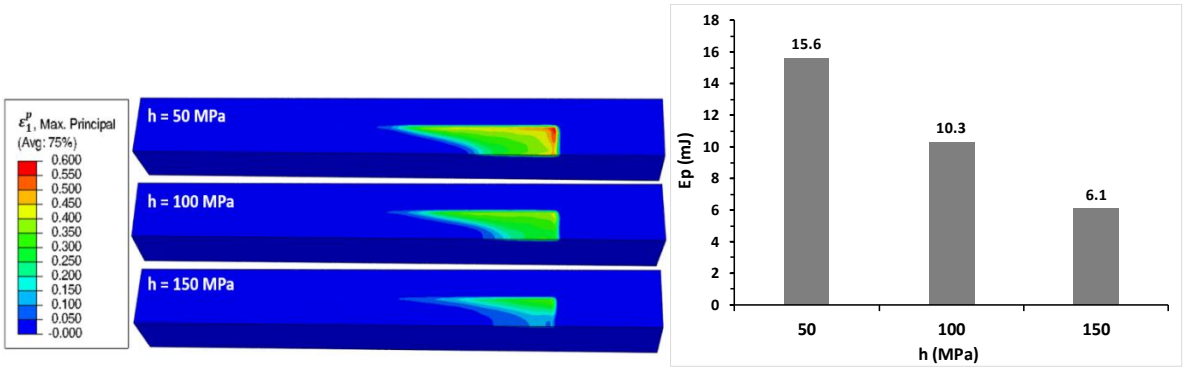

(a) (b)

Figure III-20. Effect of strain hardening slope (h) on (a) maximum plastic principal strain $\varepsilon^p{}_1$ distribution and (b) total dissipated plastic energy E_p.

Based on the above parametric analysis, the effect of the constitutive behavior on the mar resistance of PMMA, PC, and PS materials is summarized in Table III-3. PMMA has the highest mar resistance because of its high yield stress, low strain softening slope, and high strain hardening slope. Although PC has a lower strain softening slope and a higher strain hardening slope, its mar resistance is compromised by its low yield stress. Finally, PS has a higher yield stress but a significantly higher strain softening slope and a lower strain hardening slope, which decreases its mar resistance considerably.

Table III-3. Effect of the constitutive properties of the model systems on their mar resistance.
Green = increased resistance, Red = decreased resistance.

	Yield Stress	**Softening Slope**	**Hardening Slope**
PMMA	**High** (110 MPa)	**Low** (-160 MPa)	**High** (110 MPa)
PC	**Low** (70 MPa)	**Low** (-130 MPa)	**High** (130 MPa)
PS	**High** (100 MPa)	**High** (-480 MPa)	**Low** (45 MPa)

The present study aims at investigating how the constitutive behaviors of polymers influence mar visibility resistance. The model PMMA, PC, and PS were chosen to validate the framework of FEM modeling. It is hoped that the present findings can serve as a guideline for the design of polymeric materials with improved mar visibility resistance. The FEM model developed in this study can be further improved in the future by considering the material true stress-strain constitutive behavior, failure criteria, and viscoelastic behavior, which is the subject of our further research.

CHAPTER IV

NUMERICAL DETERMINATION AND ANALYSIS OF ADHESIVE FAILURE OF SEMI-RIGID POLYMERIC MULTILAYER SYSTEMS*

IV.1. Experimentals

IV.1.1. Model systems

Two model systems composed of three layers were used in this study. System 1 is PET/nylon/PET (P/N/P) and System 2 is PET/pigmented-PET/PET (P/pP/P) layered articles. The thickness of each layer was around 150 μm. The top and bottom layers of the model systems were pure PET (Laser+® C; E60A from DAK Americas). The middle layer of System 2 contained PET with pigment while the middle layer of System 1 was nylon 6 (MXD6 from Mitsubishi Gas Chemical), as shown in Figure IV-1. Samples were cut directly from the panel wall of blow-molded bottles into rectangular specimens of 110 mm in length and 15 mm in width for the scratch test.

* Part of this chapter was reprinted from Polymer Testing, 75, Molero, G., Du, S., Mamak, M., Agerton, M., Hossain, M. M., Sue, H.-J., Experimental and numerical determination of adhesive strength in semi-rigid multi-layer polymeric systems, 85-92, Copyright (2020), with permission from Elsevier.

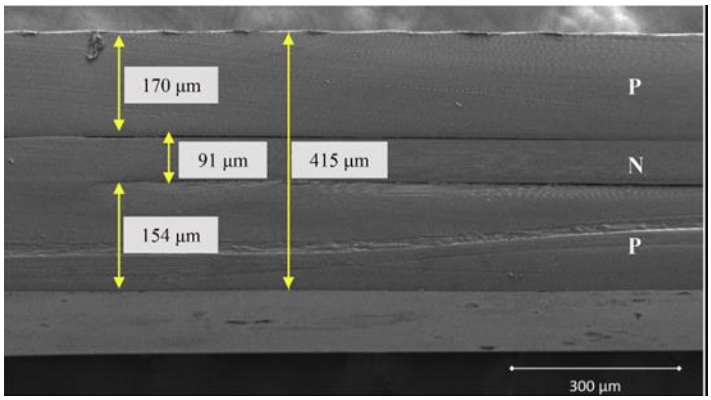

(a)

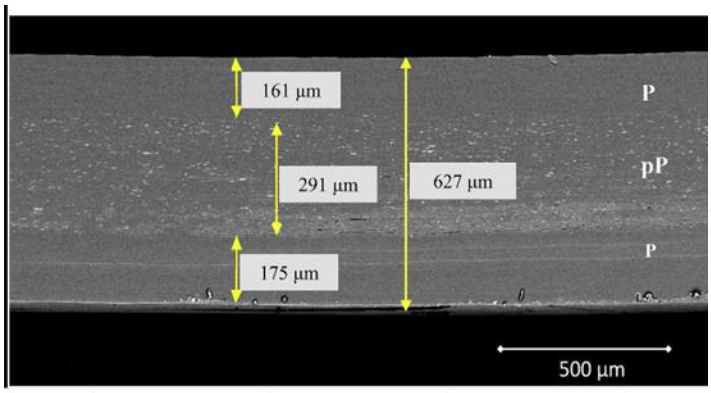

(b)

Figure IV-1. SEM image of the cross-section of (a) P/N/P and (b) P/pP/P.

IV.1.2. Determination of critical load for delamination via scratch test

Scratch tests were performed on the specimens according to the ASTM D7027/ISO 19252 using the Model G5, Surface Machine mentioned in the last Chapter. A linearly increasing normal load ranging from 1 to 120 N was applied to induce adhesive failure (layer separation) in P/N/P. For P/pP/P, the end-load was increased to 170 N to exert sufficient interfacial stress for failure to take place. The scratch velocity and scratch length were set at 10 mm/s and 100 mm, respectively. Different mar test shown in Chapter IV, a

1 mm diameter spherical stainless steel tip was used to conduct the scratch tests. A commercially available double-sided mounting tape (Catalog Number 112L from Scotch^{TM} Brand) of the width of 25.4 mm and thickness of 1.56 mm was used as a substrate. The soft substrate, i.e., the double-sided mounting tape, was used to distribute the stresses over a larger area to induce delamination, or in this case, adhesive failure. Additionally, the samples were cut into rectangular strips to reduce the overall resistance for layer separation. The systems were tested on the interior and exterior surfaces. Since the onset load for adhesive failure did not vary significantly with the tested surface, only the results of the interior surface are shown. At least three scratches were performed per sample.

Keyence VK-9700 laser scanning confocal microscope (LSCM) was employed to quantitatively observe surface profile changes produced by scratching. This tool was used to determine the onset of adhesive failure and the scratch depth profile. If the scratch depth was about the same as the thickness of the top layer (~150 μm), the damage was considered to be located at or near the interface.

IV.2. FEM Modeling

IV.2.1. 3-D FEM model

A three-dimensional (3D) FEM simulation was used to analyze the corresponding stresses induced during the scratch test [114]. ABAQUS 2017 was employed in this study to simulate the scratching process of a three-layer system onto a soft substrate. The dimensions and boundary conditions of the 3D model are illustrated in Figure IV-2 (a). The size of the model was 20 mm × 2 mm × 2 mm and only the symmetric half of the

model was simulated to reduce computation time. The x-direction movement of nodes on the symmetry plane (x=0) was fixed, z-direction displacement of all the nodes on the bottom plane (z=0) was constrained, as well as all directions on both ends of the model (y=0 and y=20). Since a half-symmetry model was incorporated, the scratch load applied during the simulation was 0.5-51 N, which corresponds to the normal load range 1-102 N in the experiment. The load range employed in the FEM model corresponds to the experimentally determined onset load for adhesive failure. Figure IV-2 (b) and (c) show the layers and the corresponding thicknesses of P/N/P and P/pP/P laminates, respectively. The mesh of the multilayer systems consists of 3D brick elements with 8 nodes in the reduced integration method (C3D8R) with the purpose of reducing computation time. The scratch tip was modeled as a rigid spherical body with a diameter of 1 mm. The contact area under the tip along the scratch path was finely meshed for better computational results. The element size of the refined mesh was 56 μm × 50 μm × 46 μm. Perfect bonding between the layers was assumed to simplify the numerical simulation. As such, the delamination phenomenon was not included in the simulation.

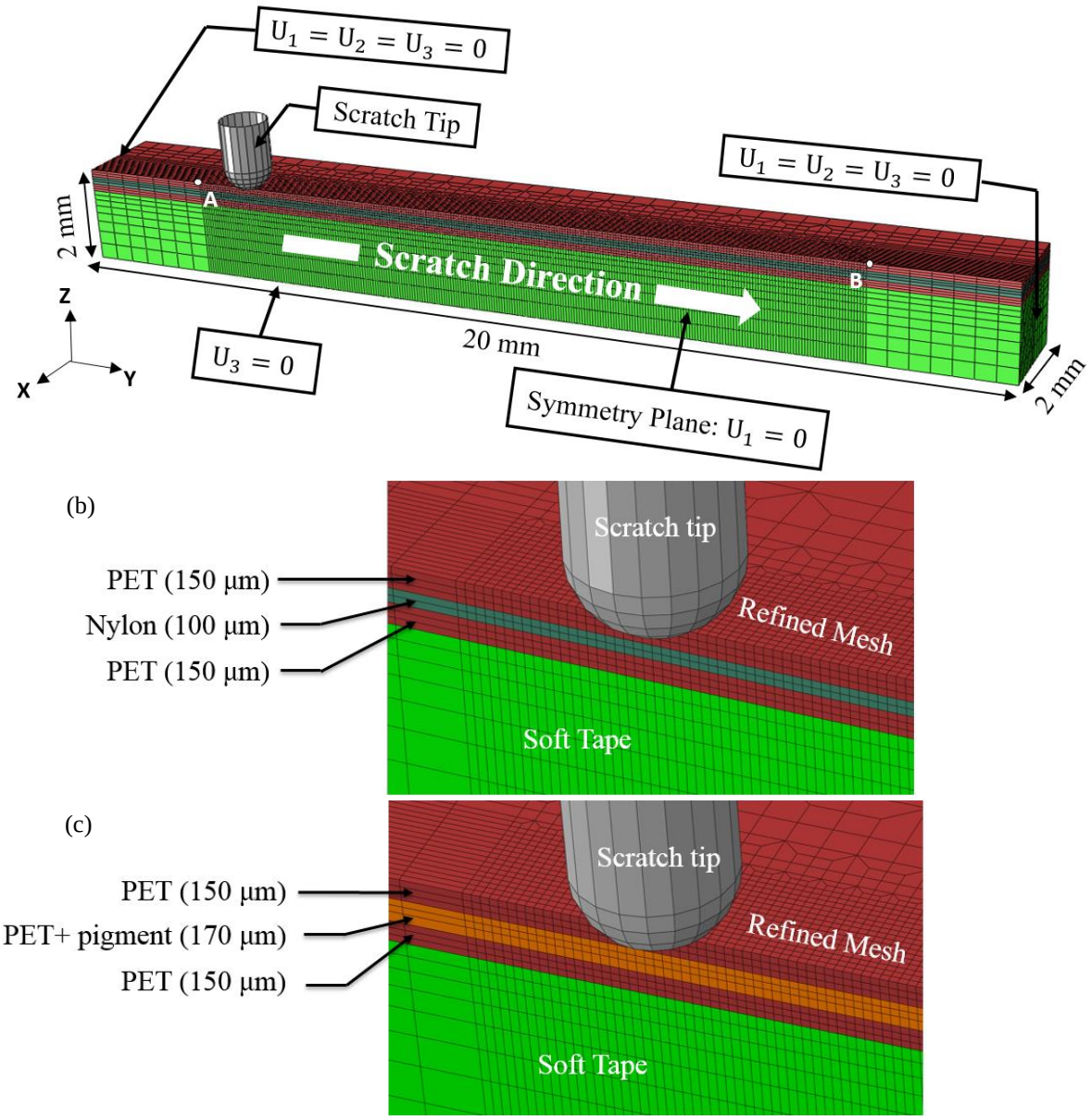

Figure IV-2. (a) FEM model of the three-layer laminated system and a soft substrate with defined boundary conditions, and the detailed dimensions of the three-layer systems for (b) P/N/P and (c) P/pP/P.

IV.2.2. Material properties

As pointed out earlier, it is difficult to obtain the exact constitutive properties of each layer in the polymeric system. Therefore, only semi-quantitative results are expected

from the present FEM modeling. The density and true stress-strain tensile properties of PET [115], nylon [116, 117], and the soft double-sided tape substrate [118] were obtained from the literature and were employed in the FEM model. Strain rate, temperature, and pressure dependent constitutive behavior were not considered in this study. The viscoelastic nature of the multi-layer systems was also neglected in the simulation. Groove formation before adhesive failure was observed during the scratch test. Therefore, both PET and nylon were modeled as elastic-plastic materials with isotropic hardening. Their material properties were approximated by a piece-wise linear curve, as shown in Figure IV-3. Material density (ρ) and some key constitutive parameters, such as Young's modulus (E), yield stress, softening slope (s), and hardening slope (h), used in the FEM modeling are summarized in Table IV-1. Since groove formation before adhesive or cohesive failure was not experimentally observed in the soft substrate, the substrate was considered as an elastic material in the simulation.

Table IV-1. Constitutive parameters used in the FEM model.

Layer	**E (GPa)**	σ_y **(MPa)**	**S (MPa)**	**h (MPa)**	$\rho\ (g/cm^3)$	**Reference**
PET	2.5	97	130	300	1.38	[115]
Nylon	3.7	73	150	150	1.15	[116, 117]

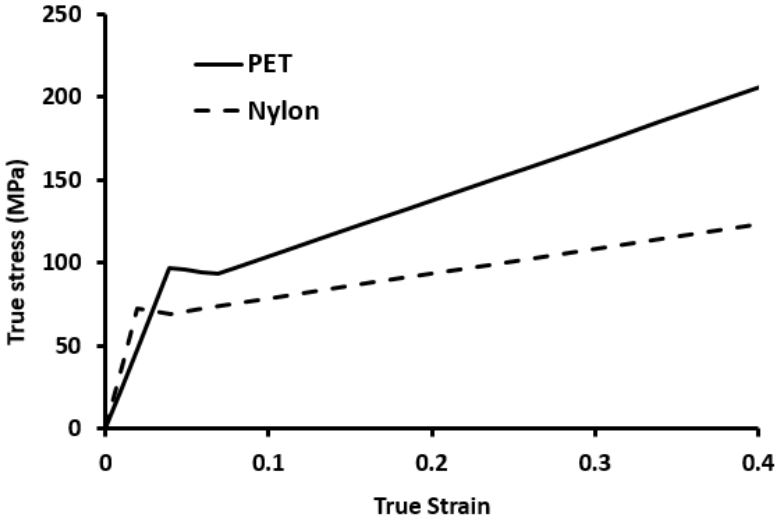

Figure IV-3. Piece-wise linear true tensile stress-strain curves of PET and nylon.

IV.3. Results and Discussion

IV.3.1. Determination of delamination process

Results from the scratch test are shown in Figure IV-4 for P/N/P and P/pP/P. The load required to induce adhesive failure for P/N/P was found to be 18.5 N, and a load of 98.5 N was required to produce cohesive failure in P/pP/P system. Adhesive failure was determined by visual observation of the change in appearance from the top to the middle layer, as shown in Figure IV-4 (b) and (c). Failure was readily apparent due to the formation of an air gap between the layers. Scratch depth was measured via LSCM if the adhesive failure was not evident by visual observation. It is noted that the layers in P/N/P systems are readily separated without significant plastic deformation during scratching. On the other hand, P/pP/P system exhibited significant groove formation before adhesive failure. P/N/P and P/pP/P show different damage features and a significant difference in

the onset load for failure. From the scratch test, P/pP/P not only shows better scratch resistance but also a much higher load to induce adhesive failure. The results suggest that the adhesive strength at the interface of PET and pigmented PET is significantly higher than that of PET and nylon. The delamination at the interfaces between PET and pigmented PET and between PET and nylon will be further analyzed in a subsequent section with FEM modeling.

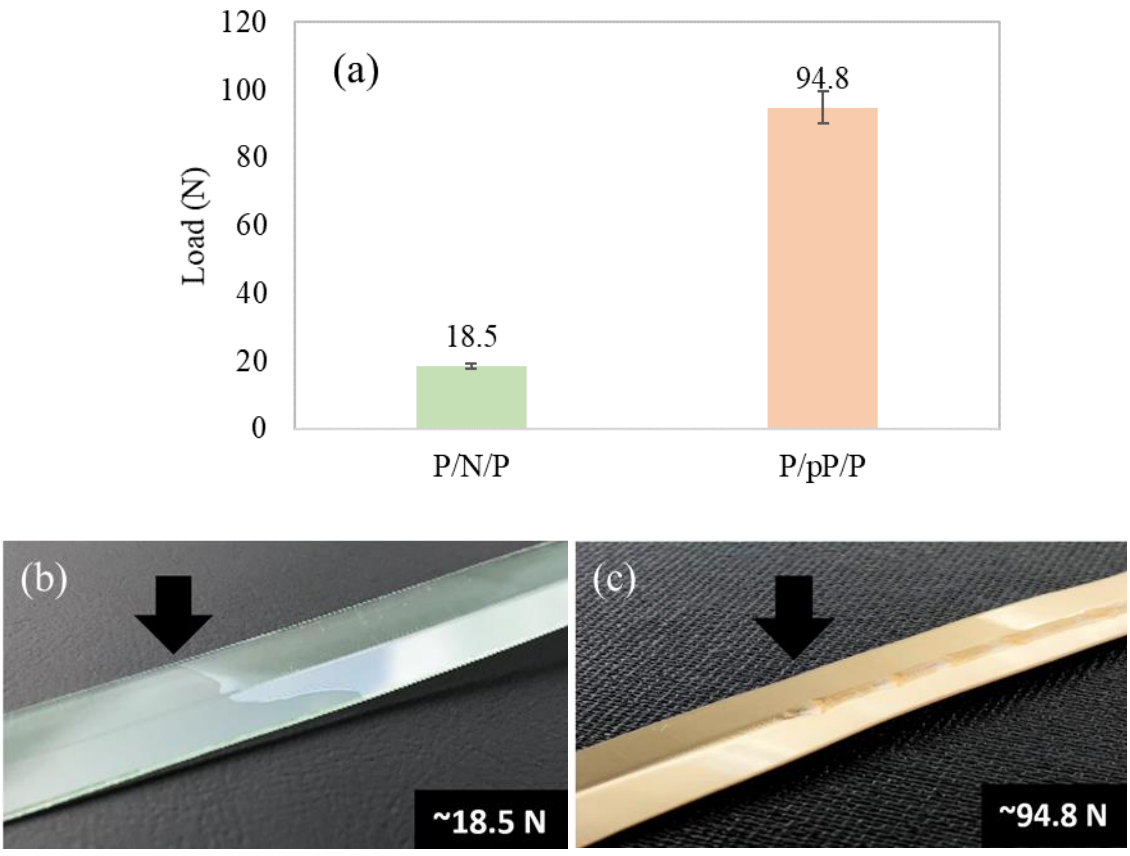

Figure IV-4. (a) Onset loads for delamination of P/N/P and P/pP/P laminates, and visual determination of delamination onset of (b) P/N/P, and (c) P/pP/P.

IV.3.2. FEM findings

As shown in Figure IV-5, the maximum principal stress contour plots for P/N/P and P/pP/P systems are similar at a load of 19 N, where adhesive failure in P/N/P system has occurred. Similar to an earlier study [9], high compressive stress exists underneath the scratch tip while high tensile stress is present in an area behind the scratch tip. The direction of tensile stress is nearly parallel with the scratch direction due to the high frictional force between the scratch tip and the top surface. Figure IV-5 also demonstrates that tensile stress does not transfer from the top layer to the middle layer due to the high modulus of the top PET layer.

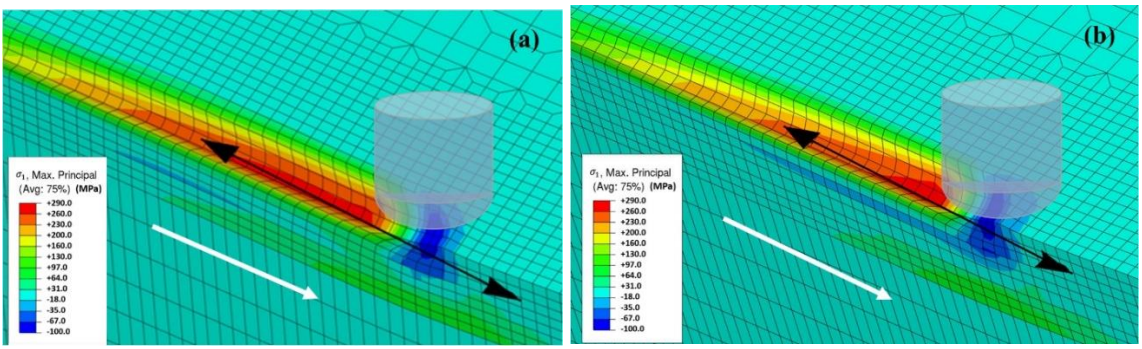

Figure IV-5. Maximum principal stress σ_1 on the top surface of (a) P/N/P and (b) P/pP/P at a load of 19 N. White arrows show the scratching direction.

The distribution of maximum principal stress σ_1 and tensile stress along the thickness direction σ_{zz} (i.e., perpendicular to the interfacial plane), after removing the top PET layer is shown in Figure IV-6 and Figure IV-7, respectively. The black arrows in Figure IV-6 and Figure IV-7 are the respective directions of the peak tensile maximum

principal stress (σ_1^t) and peak tensile stress along thickness direction (σ_{zz}^t) at the interface of both systems that corresponds to a scratch normal load of 19 N. In contrast to the P/pP/P system, P/N/P shows two high σ_1^t locations both behind and ahead of the scratch tip. Therefore, the significant difference in material properties between layers can induce significant inter-laminar stresses. This is in accordance with our experimental findings, which showed that P/N/P exhibits a significantly earlier onset load for adhesive failure. This is possibly due to the difference in material properties between the layers, which cause the development of a high interfacial stress component. A previous study [43] has shown that the relative stiffness and strength of both top and middle layers can significantly affect the scratch deformation and damage transitions. Figure IV-6 (b) and (d) show that the directions of the peak σ_1^t in the two systems are about 135° and 60° from the scratch direction, respectively, indicating the possible adhesive failure directions between top and middle layers. Additionally, Figure IV-7 demonstrates that the distribution of σ_{zz} at the interface at this load is similar for both systems, with the exception of a small area ahead of the tip above 30 MPa in the P/N/P system. However, this area is not associated with adhesive failure because the peak σ_{zz}^t exists on the scratch shoulder designated by a black arrow. Thus, the difference in σ_1^t magnitude at the interface can be considered for the assessment of the differences in the onset of adhesive failure stress of the two systems. It also suggests that compared to σ_{zz}^t, σ_1^t is more reasonable to demonstrate the correlation between the stress distribution at interface in FEA analysis and the delamination resistance measured from experiments.

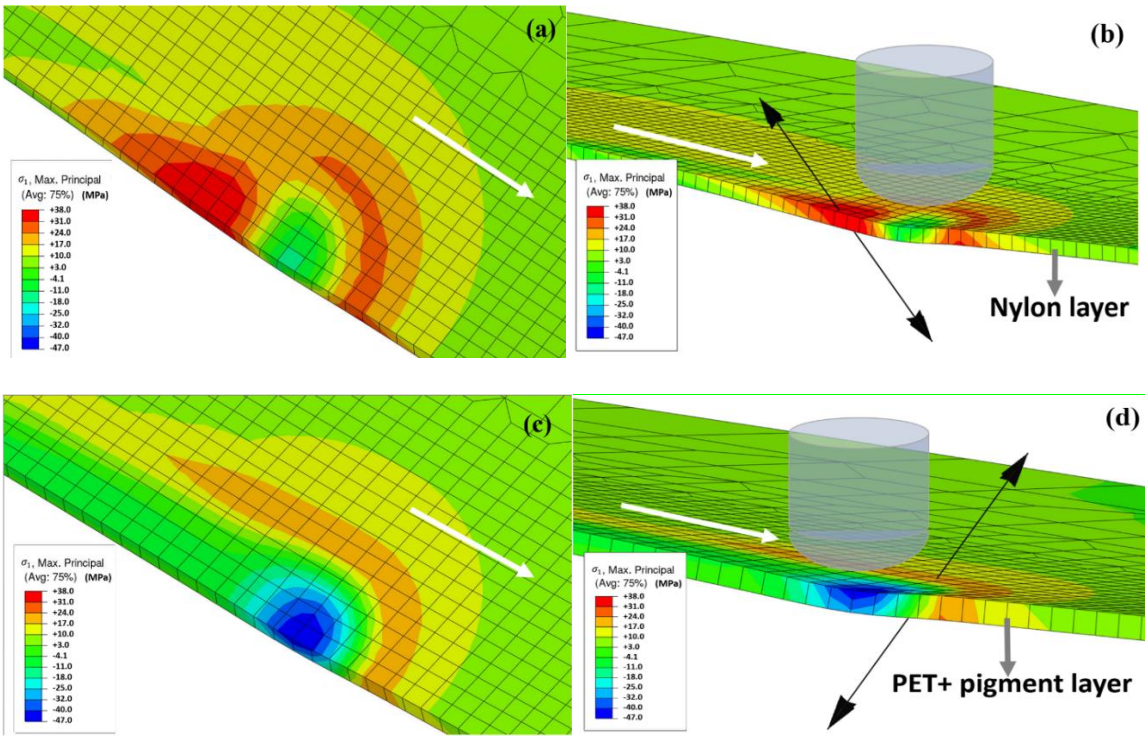

Figure IV-6. (a) Maximum principal stress σ_1 and (b) direction of the peak σ^{t}_{1} at PET and nylon interface; (c) maximum principal stress and (d) direction of the peak σ^{t}_{1} at PET and pigmented PET interface. Both systems at a load of 19 N. White arrows indicate the scratch direction.

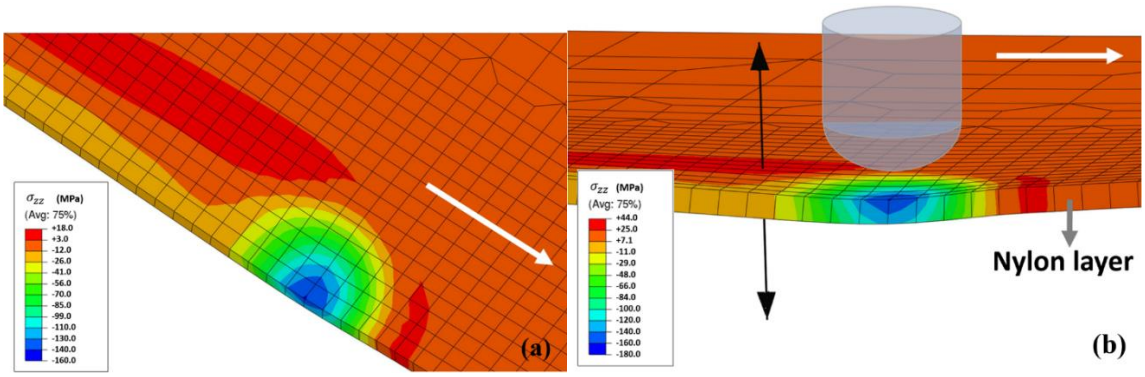

Figure IV-7. (a) Stress component along the thickness direction σ_{zz} and (b) direction of the peak σ^{t}_{zz} at PET and nylon interface; (c) stress component along the thickness direction σ_{zz} and (d) direction of the peak σ^{t}_{zz} at PET and pigmented PET interface. The scratch tip is located at the delamination load of 19 N. White arrows show the scratching direction.

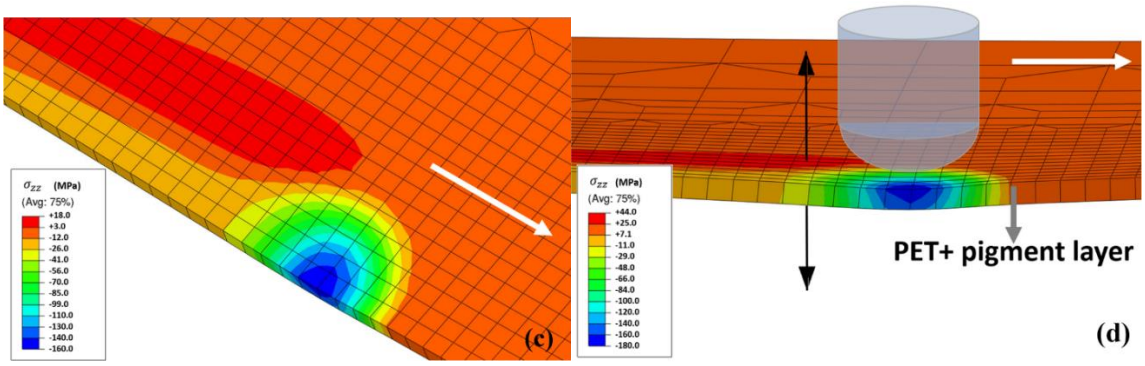

Figure IV-7. Continued.

Both the maximum principal stress σ_1 and stress along the thickness direction σ_{zz} at the P/pP/P interface at a load of 95 N, where adhesive failure takes place, are shown in Figure IV-8. At this load, the middle layer is severely deformed and exhibits high tensile maximum principal stress (σ_1^t) and tensile stress along z direction (σ_{zz}^t) at the interface behind the scratch tip. The direction of the peak σ_1^t is about 20° with the scratch direction and high σ_{zz}^t exists right behind the scratch tip, which could be responsible for the adhesive failure.

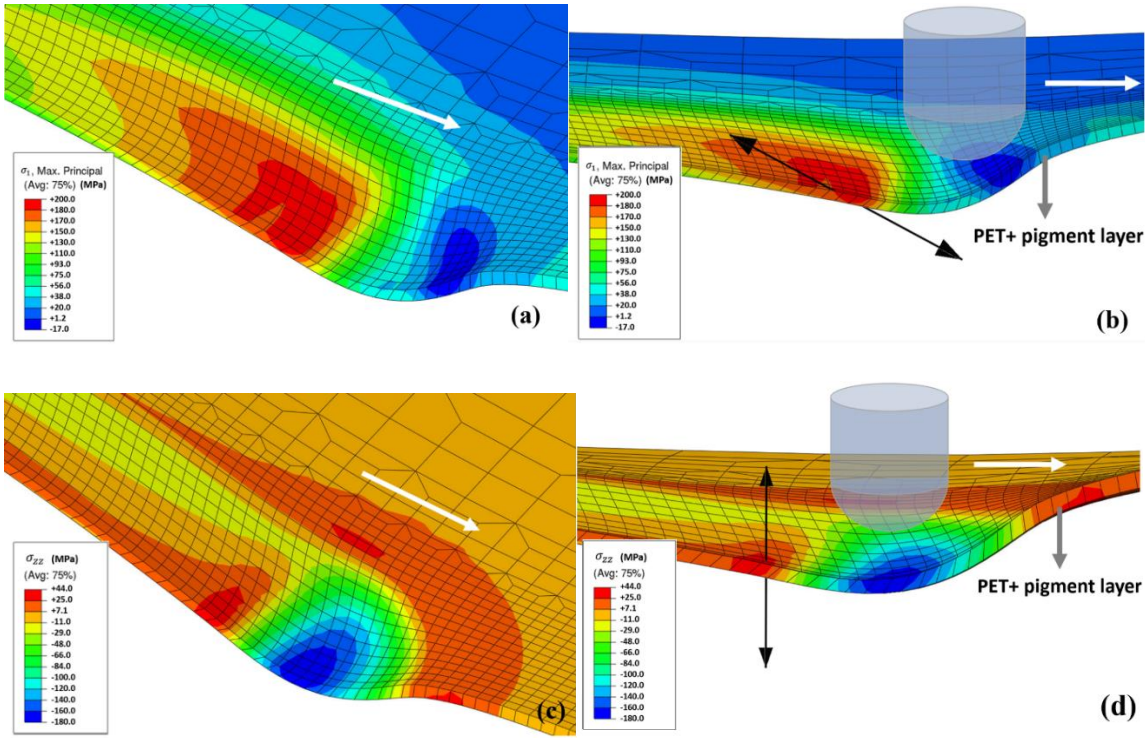

Figure IV-8. (a) Maximum principal stress σ_1 contour plot; (b) direction of the peak σ^t_1, at the interface of PET and pigmented PET; (c) stress component along the thickness direction; and (d) direction of the peak σ^t_{zz}, at the interface of PET and pigmented PET at a normal load of 95 N. White arrows indicate the scratching direction.

According to an earlier study [62], it has been shown that the tensile maximum principal stress, σ_1^t, and the tensile stress component in the z-direction, σ_{zz}^t, are dominant in the adhesive failure process during scratch testing, and mode I damage is expected to be responsible for the delamination. The peak σ_1^t and σ_{zz}^t at the interface with respect to the scratch normal load is shown in Figure IV-9 (a) and (b), respectively. As shown, as the scratch normal load increases, the peak σ_1^t stress increases approximately linearly for both P/N/P and P/pP/P systems, as well as the peak σ_{zz}^t for the P/N/P system. The difference in peak σ_1^t between the P/N/P and P/pP/P systems explains the observed

difference in their onset of adhesive failure. On the other hand, a plateau is observed in the peak σ_{zz}^{t} from a scratch load of 27–62 N in the case of the P/pP/P system. The peak tensile plastic strain in the thickness direction ε_{zz}^{p} and peak σ_{zz}^{t} at the interface as a function of scratch normal load is shown in Figure IV-10. Based on the results, it can be observed that the peak tensile ε_{zz}^{p} is very small before the beginning of the plateau. From the beginning of the plateau, the peak tensile ε_{zz}^{p} at the interface near the scratch tip increases significantly as the scratch normal load increases, which is due to yielding of the top PET layer in the P/pP/P laminate. During the "plateau period", where the scratch normal load ranges from 27 to 62 N, the contact area around the scratch tip increases significantly with the plastic deformation of the PET layer. As a result, the peak σ_{zz}^{t} at the interface stays at a similar small magnitude. Table IV-2 summarizes the onset of adhesive failure load and the peak delamination stresses, σ_{1}^{t} and σ_{zz}^{t}, at the interface. By comparing the calculated delamination strengths of P/N/P and P/pP/P respectively according to the σ_{zz}^{t} criterion and σ_{1}^{t} criterion, it could also conclude that tensile maximum principal stresses (σ_{1}^{t}) criterion is more reasonable for future scratch-induced delamination study, due to the obvious difference in their delamination resistances demonstrated in the experiments.

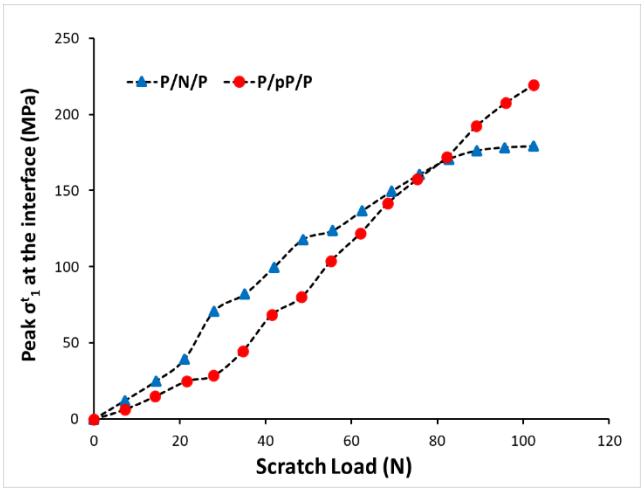

(a)

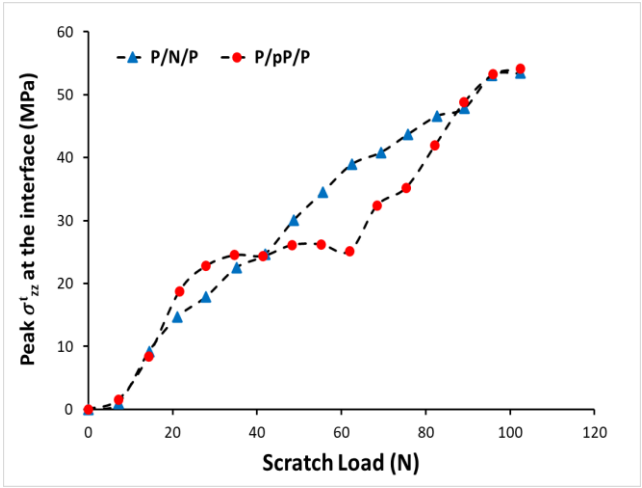

(b)

Figure IV-9. Peak (a)σ^{t}_{1} and (b)σ^{t}_{zz} as a function of scratch normal load at the interface of P/N/P and P/pP/P laminates.

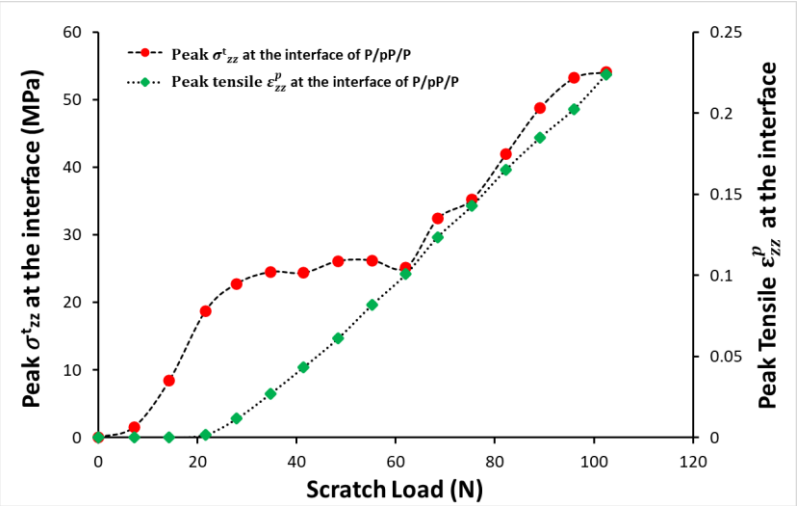

Figure IV-10. Peak σ^t_{zz} and tensile ε^p_{zz} as a function of scratch normal load at the interface of P/pP/P laminate.

Table IV-2. Delamination load, the peak delamination stresses, σ^t_1 and σ^t_{zz}, at the interface.

FEM Results	P/N/P	P/pP/P
Onset of delamination load (N)	19	95
Max. σ^t_1 at delamination (MPa)	27	195
Max. σ^t_{zz} at delamination (MPa)	10	50

As mentioned earlier, most of the common practices used to assess the delamination of polymer provide a "pass or fail" assessment with no insight about structure-property relationships. Based on this study, the proposed methodology can determine the adhesive strength of semi-rigid multi-layer polymeric systems in a practical and reproducible manner. This procedure can be employed to improve the performance of

multi-layer polymeric systems through changes in formulation and processing conditions. The present study suggests that combining a scratch test with FEM can serve as a tool to fundamentally understand the delamination phenomena. FEM plays a significant role in showing how both changes in layer material properties and geometry influence the delamination process during scratching. It should be noted that only generic material properties were used for the current simulation, which does not consider the morphology and anisotropy of each polymer layer in the multi-layer system. However, in principle, FEM can still be used to determine the adhesive failure stress that corresponds to the experimentally observed adhesive failure by including the actual material and surface properties in the numerical framework. It has been shown that, by including the rate and pressure dependent material and frictional behavior in the numerical framework, the scratch behavior of polymers can be predicted quantitatively using FEM [46]. Thus, by including the exact material constitutive behavior and surface characteristics of each layer in the system in the numerical framework, the adhesive strength of the multi-layer system can be predicted using numerical modeling. The determination of the adhesive failure stress between any layers is possible by normalizing geometric factors and material properties in the FEM model. It should also be noted that the proposed approach is not applicable for low yield stress and low strength systems where significant layer deformation and damage would occur before interlayer delamination can take place. Care should be taken when the proposed methodology is chosen for determining the delamination strength of weak and soft laminated systems.

CHAPTER V

FEM ANALYSIS TO SCRATCH INDUCED DELAMINATION OF POLYMERIC MULTILAYER STRUCTURES

The FEM analysis in CHAPTER IV has shown that tensile maximum principal stress (σ_1^t) distribution at the interface could be utilized as the criterion to analyze the scratch induced delamination damage. In this chapter, a more universal study about scratch induced delamination via FEM modeling was carried out to gain fundamental knowledge.

V.1. Experimentals

V.1.1. Model systems

Epoxy-based bi-layer coatings on a steel plate were chosen as the model systems to perform the scratch tests and to validate the FEM simulation findings. The structure of the model two-layer coating system used in the current study is schematically shown in Figure V-1. The epoxy utilized in this study was a liquid diglycidylether bisphenol-F (DGEBF) epoxy resin (D.E.R. 354, Dow Chemical). A Mannich curing agent (D.E.H. 615, Dow Chemical) was chosen which allows for the fast cure at room temperature. To alter the constitutive properties of each coating layer, different amount of monoamine (Jeffamine® M 1000, Huntsman) was mixed with the epoxy resin to prepare a set of model systems with three distinctly different properties: (1) neat DGEBF epoxy, (2) 20 wt.% M1000 in DGEBF epoxy, and (3) 32 wt.% M1000 in DGEBF epoxy. The epoxy resin, curing agent, and monoamine were prepared in the stoichiometric ratio before curing at

room temperature. The monoamine group of M1000 reacts with the epoxide group in epoxy matrix to reduce the crosslink density of the molecular network. Therefore, the mechanical properties including modulus, yield stress, and tensile strength are expected to reduce with an increasing amount of M1000 in epoxy [20].

The epoxy formulations prepared above were homogeneously mixed, followed by the removal of trapped air bubbles with a vacuum pump at room temperature. These epoxies were utilized to prepare bi-layer coatings for scratch tests and in bulk forms for uniaxial tensile and compressive tests.

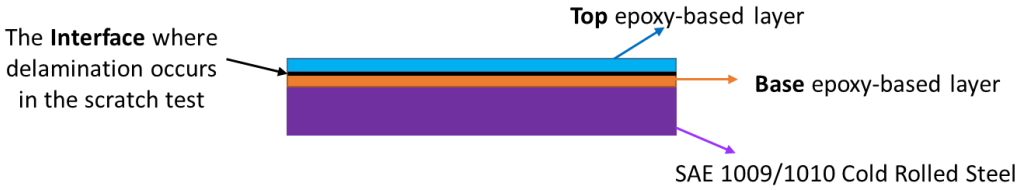

Figure V-1. Schematic of the model coating systems used for this study.

V.1.2. Preparation of double-layer coating system

Cold-rolled steel corrosion coupons from Q-lab® (1008/1010) were utilized as backings for double-layer epoxy coatings. A 2.5 inches width base coating was uniformly applied on the steel backings with BYK® 4301 film casting knife. The micrometer mounted on the casting knife and the accessory elcometer® calibration foil could control the gap clearance precisely. A Keyence® VK9700 violet laser scanning confocal microscope (VLSCM) was used to check the applied coating thickness. After base layer

coating cured, a ~1.5 μm thick PTFE release agent dry lubricant (miller-stephenson® MS-122AD) was sprayed on the base coating. It should be mentioned that the PTFE lubricant particles at the interface only covered part of the surface as shown in Figure V-2. Therefore, the bonding strength was only weakened instead of completely unbonded. The purpose of applying PTFE agent at the interface is to make delamination in scratch test takes place before the onset of unstable plowing damages, since there is still a lack of appropriate FEM modeling approach to model the plowing damages. And the onset of delamination is easier to track when the scratch groove is not obvious. Then one little drop of soluble blue dye was added to the epoxy resin when the top layer coating was made. By doing this, a color difference between the detached and undetached parts shown in Figure V-3 helps in the visual identification of delamination in the scratch test. The coating formulation and thicknesses chosen for the model bi-layer epoxy coating systems prepared for this study are summarized in Table V-1, Table V-2, and Table V-3.

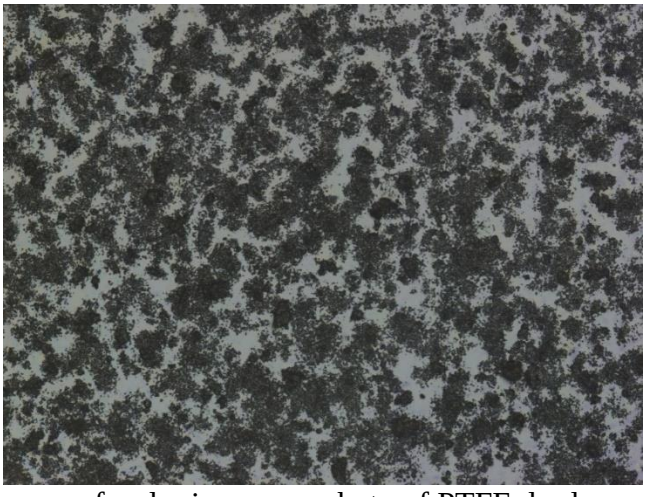

Figure V-2. Laser confocal microscope photo of PTFE dry layer at the interface.

Figure V-3. Onset of delamination in the scratch test.

Table V-1. Model systems for the base layer thickness effect study.

Top layer thickness (μm)	Base layer thickness (μm)
100	50
100	200
100	400
100	600

Table V-2. Model systems for the top layer thickness effect study.

Top layer thickness (μm)	Base layer thickness (μm)
50	400
150	400
250	400

Table V-3. Model systems for the base layer property effect study with top layer thickness = 100 μm and bottom layer thickness = 200 μm.

Top layer M1000 mount	Base layer M1000 mount
0	0
0	~ 20 wt.%
0	~ 32 wt.%

V.1.3. Uniaxial tensile behavior characterization

The model systems in liquid form were poured into a 3.5 mm thick rectangular glass mold coated with polytetrafluoroethylene (PTFE) mold release agent. After 7 hours curing at room temperature, it was taken out of the mold and cut into dumbbell shape with narrow section = 5.5 mm and gauge length = 33 mm. All the cutting edges were carefully polished with FEPA standard 2400 grit sandpaper to remove all the defects. An ultrafine black ink marker was utilized to apply speckles randomly in the gauge area. MTS Insight load frame combined with a custom-built tensile fixture was utilized to perform the tensile test. The quasi-static tensile tests were done with comparable strain rates among the systems. The tensile yield stress is used to calculate parameters in the Drucker-Prager model. A Canon EOS 5d Mark II DSLR camera was utilized to record the shape changes of the speckles during the test. Then the outputs from MTS Insight and camera were input into the commercial VIC-2D™ DIC software package to calculate the true strains in the tensile and lateral directions ε_{yy}, ε_{xx}. Based on the transverse isotropy assumption ($\varepsilon_{xx} = \varepsilon_{zz}$), true stress σ_{yy} was calculated by considering the lateral deformation in x and z directions. Three tests were performed on each system to check the consistency.

V.1.4. Uniaxial compression behavior characterization

The model systems in liquid form were poured into a 1-inch diameter cylindrical glass mold covered with polytetrafluoroethylene (PTFE) mold release agent. After 7 hours of curing at room temperature, it was taken out of the mold and cut with a diamond saw to the dimensions $6\,mm \times 6\,mm \times 10\,mm$. FEPA standard 4000 grits sandpaper was utilized to polish the top and bottom surface to make them smooth and parallel to each

other. A thin layer of lubricant was uniformly applied to the testing fixture to reduce the friction during the test. Then the fixture was installed into the MTS Insight load frame for the test. The strain rates of the three different material compositions are the same as those for uniaxial tensile tests. A Canon EOS 5d Mark II DSLR camera was utilized to record the dimension change in the lateral direction for ε_{xx} calculation. Compression displacement recorded by the load frame was used to calculate the true strain ε_{yy}. True stress σ_{yy} was calculated in the same way as those for uniaxial tensile tests. Three tests were performed on each system to confirm the consistency.

V.1.5. Scratch test

Like the scratch test performed in the previous chapters, the scratch tests for this study were performed using a 1-mm diameter stainless steel sphere tip with 10 mm/s over the length of 80 mm in the linearly increasing load range of 1-30 N.

V.1.6. Coefficient of friction (COF) measurement

The COF measurement procedure is similar to that described in section III.1.5 Testing speed was chosen to be the same as the scratch test 10 mm/s [30]. Three tests were conducted on each system over the 80 mm length under a constant load of 5 N. Then the COF was determined by the ratio of the tangential force experienced to the normal load applied during scratch tests [93].

V.2. FEM Modeling

V.2.1. 3D FEM model

The commercial finite element package ABAQUS 2017® [99] was utilized in this study to conduct the FEM modeling of the scratch process on a bi-layer coating on a steel

substrate [22]. The dimensions and boundary conditions of the 3D model are presented in Figure V-4 (a). Figure V-4 (b) illustrates the structure of the multilayer system in detail including the top, base epoxy coatings, and the steel substrate. The whole multilayer system was meshed with 3D linear brick full integration elements (C3D8). And a refined mesh with element dimensions of $23\ \mu m \times 28\ \mu m \times 20\ \mu m$ was employed across a critical distance A-B for better computational accuracy. The mesh size was determined in the preliminary simulations for the mesh convergence of computational results. The thickness of each layer of coating was precisely controlled by modifying the number of element layers. The scratch tip was modeled as the cylindrical rigid body at the bottom end connecting with a 1 mm diameter hemispheroid. FEM modeling is to simulate the condition right before delamination takes place. Therefore, perfect bonding between the laminates was assumed for the numerical calculation. Furthermore, as illustrated above, no cohesive elements or cohesive-based surface were involved in the current model to investigate the real delamination.

The scratch process was simulated over a distance of 12 mm with a linearly increasing load from 0.5 to 15 N. Since a half-symmetry model was employed, the scratch load applied in the simulation was corresponding to the normal load range of 1-30 N in the experiments. The COF between the scratch tip and top coating was chosen as 0.28 which is the average value measured by the experiment.

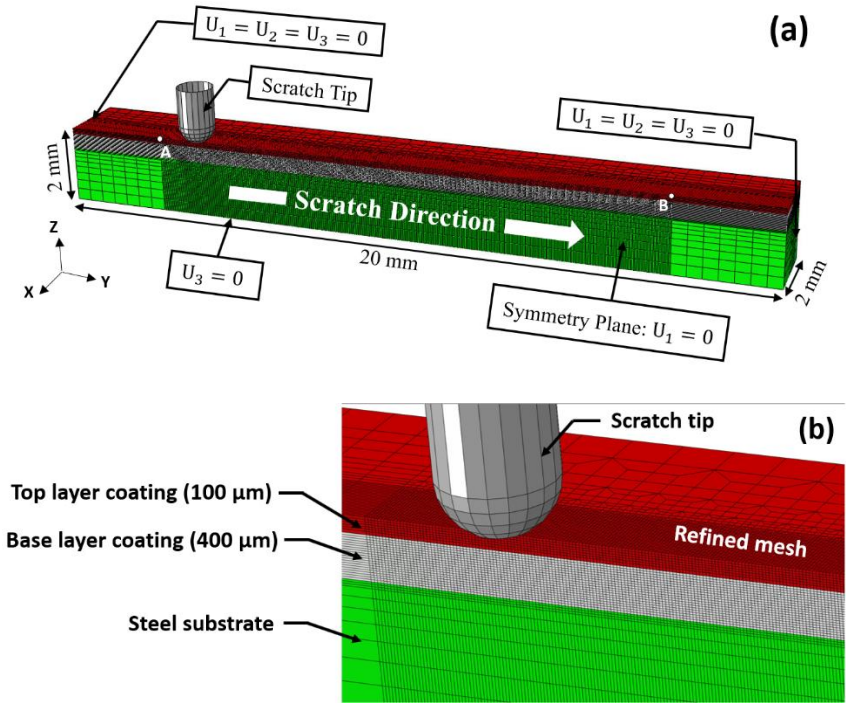

Figure V-4. A FEM model of the double-layer coating system and a steel substrate showing (a) the overall geometry and boundary conditions and (b) the thickness of the multilayer system.

The equation below was used to calculated the angle θ between the peak tensile maximum principal stress (σ_1^t) and the interface in the user subroutine (VUSDFLD). Since the interface doesn't deform severely, it is assumed to be still in the undeformed configuration (x-y surface) to simplify the problem.

$$\theta = \cos^{-1}\left(\frac{\sqrt{(\cos\alpha)^2+(\cos\beta)^2}}{\sqrt{(\cos\alpha)^2+(\cos\beta)^2+(\cos\gamma)^2}}\right) \quad \text{(V-1)}$$

Where α, β, γ are respectively the angle between the principal direction of peak σ_1^t and x, y, z axis. And the corresponding cosine values $\cos\alpha$, $\cos\beta$, and $\cos\gamma$ could be directly obtained via the VSPRIND function in ABAQUS 2017®.

V.2.2. Material properties

The constitutive model was chosen based on the uniaxial tensile/compression characterization results as shown in Figure V-5. Hydrostatic pressure dependent behavior needs to be included in the FEM model because polymer deformation and fracture is hydrostatic stress dependent [75, 76]. Time independent material properties were assumed for all the model systems because scratch testing speed is quite high and the delamination growth is not the focus of the current work. Since the neat epoxy system follows a typical elastic-plastic constitutive behavior, a yield criterion namely the Drucker-Prager model was utilized to depict the hydrostatic pressure dependent yielding behavior of the neat epoxy. The yield function F and flow potential G of linear Drucker-Prager model in ABAQUS 2017® can be briefly expressed from the equation from (V-2) to (V-4).

$$\mathrm{F} = \mathrm{t} - \mathrm{P}\tan\beta - d = 0 \tag{V-2}$$

$$G = t - P\,tan\,\psi \tag{V-3}$$

With

$$t = \frac{1}{2}q\left[1 + \frac{1}{K} - \left(1 - \frac{1}{K}\right)\left(\frac{J_3}{q}\right)^3\right] \tag{V-4}$$

Where P is the hydrostatic pressure, β is the angle of friction qualifying the slope of the linear yield surface in the meridional plane, which can be approximated by inputting the yield stress measured in uniaxial tension and compression tests. And d is the cohesion of material based on Mohr-Coulomb theory. ψ is the dilation angle in the meridional plane, which was assumed as 0 for neat epoxy. And q is the current von-Mises value, K is the material constant controlling the dependence of the yield surface on the value of the

intermediate principal stress. J_3 is the third principal scalar invariants of the deviatoric stress tensor.

According to the above equations, the parameters of neat epoxy to be input into the ABAQUS 2017® Drucker-Prager model were calculated based on the uniaxial tensile/compression testing results and summarized in Table V-4. And the strain softening and strain hardening behaviors were modeled by using the compressive experimental data shown in Figure V-5 (a).

Table V-4. Parameters for neat epoxy in the Drucker-Prager model.

Angle of Friction (β)	31.24°
Flow Stress Ratio (K)	0.83
Dilation Angle (Ψ)	0

Both the sample of 20 wt.% M1000 and 32 wt.% M1000 doesn't show any sign of plastic deformation in the uniaxial compression and tension tests. Therefore, a hyperelastic constitutive model namely the Marlow model was utilized to simulate the non-linear elastic behaviors for these two model systems as shown in Figure V-5 (a)(b), by directly inputting both uniaxial compression and tensile testing data.

V.3. Results and Discussion

V.3.1. Experimental results

V.3.1.1. Tension and compression behaviors

By conducting the testing procedure illustrated above, the uniaxial tensile and compressive true stress-strain curves of the model systems were generated and compared in Figure V-5 (a) and (b). In the tensile test, all the specimens were stretched to break to determine their tensile strength, while the compression tests were stopped before compressive failure occurs, when engineering strain reaches 80%. It was found that the 20 wt.% M1000 and 32 wt.% M1000 samples showed a fully elastic recovery after both tensile and compression tests, which demonstrated pure hyperelastic behavior. Only 0 wt.% M1000 epoxy exhibits yielding phenomenon during the test. As shown in Figure V-5 (a) and (b) respectively, these two model systems show non-linear hyperelastic behaviors. On the other hand, the neat epoxy system exhibits a yielding phenomenon and deform plastically under uniaxial compression, but failed right after yielding point in the brittle fashion under uniaxial tension.

In order to compare the elastic modulus values of the three model systems, compression and tensile tests were conducted for neat epoxy, 20 wt.% M1000 and 32 wt.% M1000 samples at a strain rate of $3 \times 10^{-4}/s$. The key uniaxial tensile and compressive properties were summarized in Table V-5. As expected, introduction of more M1000 made the compressive and tensile modulus and tensile strength to decrease while improving the elongation at break due to reduction in crosslink density.

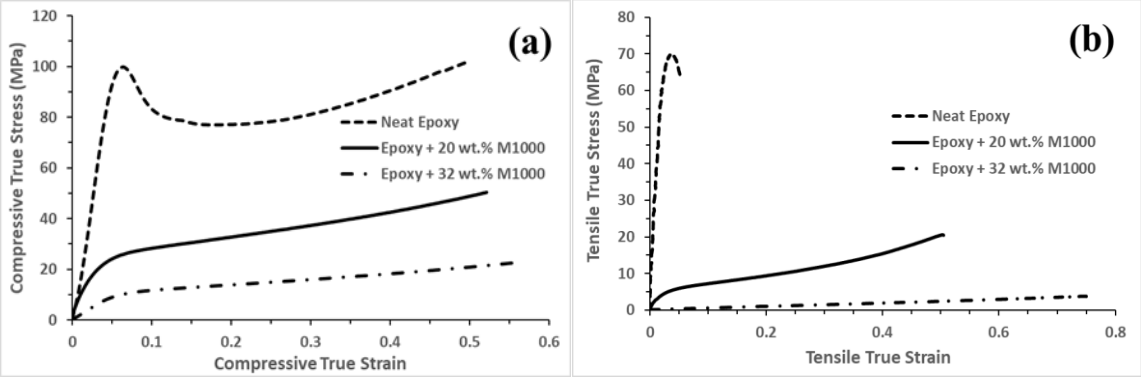

Figure V-5. (a) Compressive and (b) tensile behaviors of neat epoxy, epoxy + 20 wt.% M1000, and epoxy + 32 wt.% M1000.

Table V-5. Comparison between uniaxial tensile and compressive behaviors of model systems.

	Neat Epoxy	**20 wt.% M1000**	**32 wt.% M1000**
Tensile Young's modulus (GPa)	2.3 ± 0.1	0.34 ± 0.01	0.004 ± 0.0003
Tensile yield stress (MPa)	67.4 ± 2.0	-	-
Tensile strength (MPa)	67.4 ± 2.0	24.8 ± 4.7	2.1 ± 1.3
Tensile strain at break (%)	4.8 ± 0.4	50.5 ± 26.1	60.2 ± 22.8
Compressive Young's modulus (GPa)	3.0 ± 0.1	0.35 ± 0.04	0.018 ± 0.003
Compressive yield stress (MPa)	97.4 ± 2.8	-	-

V.3.1.2. Scratch test results

The critical onset loads of delamination identified using the scratch tests with different top and base layer thicknesses and M1000 content of the base layer are respectively shown in Figure V-6 (a)-(c). It is apparent that the increasing top layer

thickness and M1000 content delays the onset of delamination, while the base layer thickness does not have any effect on the onset of delamination, within the ranges of layer thicknesses considered in this study.

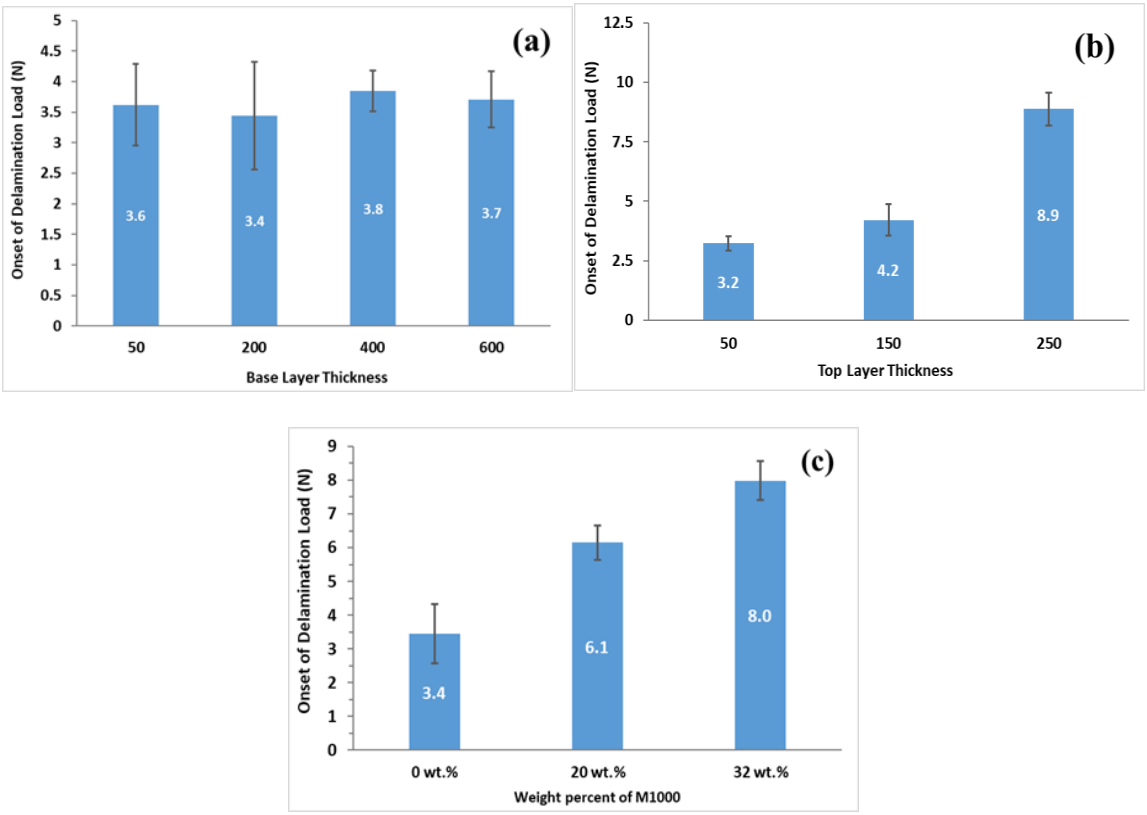

Figure V-6. The effect of (a) base layer thickness (b) top layer thickness and (c) M1000 content of base layer on the delamination resistance in scratch tests.

V.3.2. FEM modeling results

V.3.2.1. FEM model validation

The peak σ_1^t magnitude at the interface of each model system was captured in the FEM model at the onset delamination loads shown in Figure V-6. These results are

demonstrated in Figure V-7. In Figure V-7 (a) and (b), by taking into account of standard deviation, the peak tensile stresses at the onset loads of delamination are nearly the same regardless of different top and bottom layer thicknesses. This validates the FEM model since the actual delamination stresses at the interface should not be affected by the thicknesses of the coating layers. Figure V-7 (c) shows that the peak tensile stress at the interface reduces in the model system with increasing M1000 in the base layer. This is mainly due to the ability of the base layer to help redistribute imposed stresses away from the interface and into the base layer.

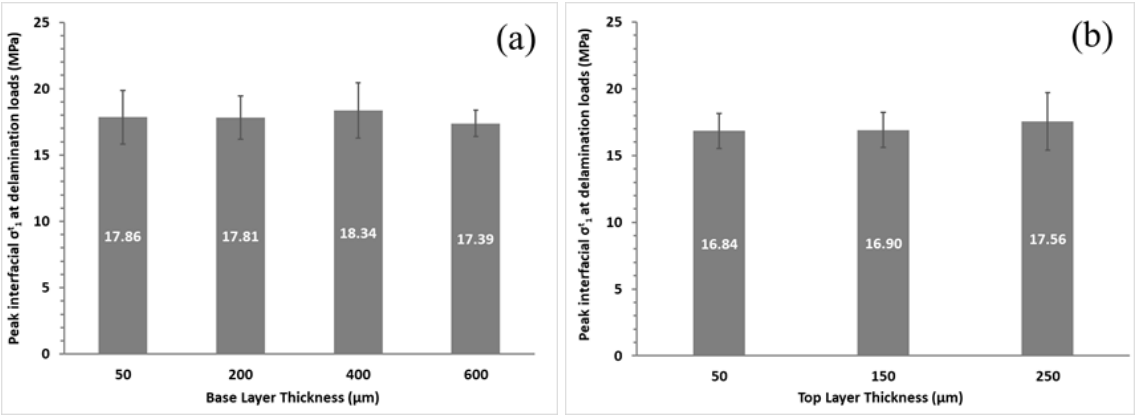

Figure V-7. The effect of (a) base layer thickness (b) top layer thickness (c) base layer weight percent of M1000 on peak σ^{t_1} at the interface at delamination loads.

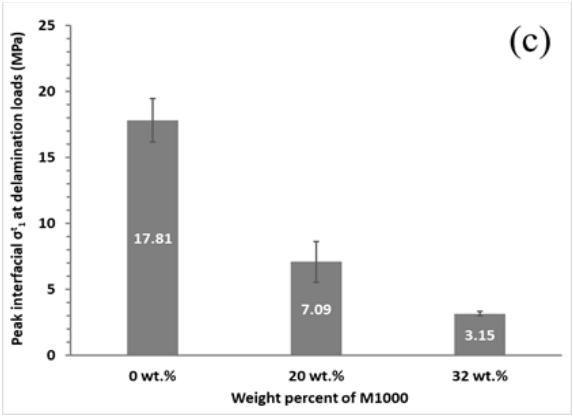

Figure V-7. Continued.

V.3.2.2. Extreme cases study to yield stress

Before showing the parametric study in the next section, it is necessary to point out the complexity of the delamination phenomenon in this work. Two extreme cases are considered: with Case I for the top layer σ_y = 30 MPa and base layer σ_y = 150 MPa and Case II for the top layer σ_y = 150 MPa and base layer σ_y = 30 MPa. The thicknesses of the top and base layers are chosen as 100 μm and 400 μm, respectively. To simplify the problem, other material constitutive behaviors such as elastic modulus, strain softening, and strain hardening behaviors are assumed to be piece-wise linear and kept the same for both layers, as shown in Figure V-8.

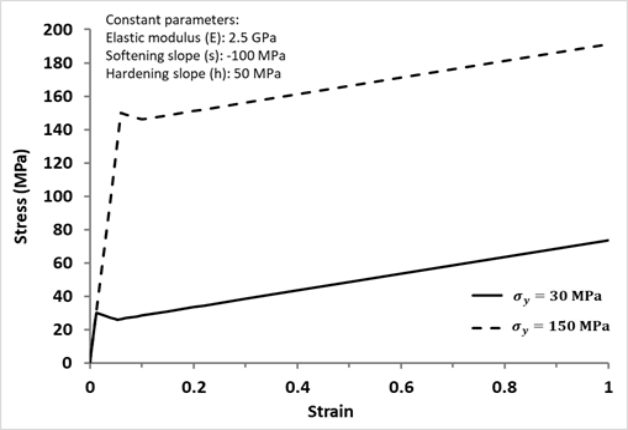

Figure V-8. The piece-wise linear stress-strain curves for the extreme cases study.

Figure V-9 (a) shows the peak tensile maximum principal stress (peak σ_1^t) at different locations of the interface that develops with increasing scratch load for the Case I scenario. It is found that the position of the peak σ_1^t on the entire interface is not always right behind the scratch tip. It may be located on the shoulder of the scratch groove, as well. When the scratch load is below 16 N, the peak σ_1^t is located on the scratch shoulder, which means that the delamination will probably initiate from the scratch shoulder if it occurs below this load range. However, when the scratch load is higher than 16 N, the delamination at the interface has a higher possibility of occurring right behind the scratch tip due to the higher peak σ_1^t value in this location. Furthermore, the FEM simulation shows the base layer laminate begins to yield at the scratch load 25 N, since the equivalent plastic strain is above 0. The peak σ_1^t magnitude at interface begins to show a small drop due to the strain softening behavior of the material behind the scratch tip. Figure V-9 (b) shows the direction of peak σ_1^t changes with scratch load. It is noted that the peak

σ_1^t location shift from scratch shoulder to the area behind the scratch tip at a scratch load of 16 N has led to a dip in σ_1^t (Figure V-9 (b)).

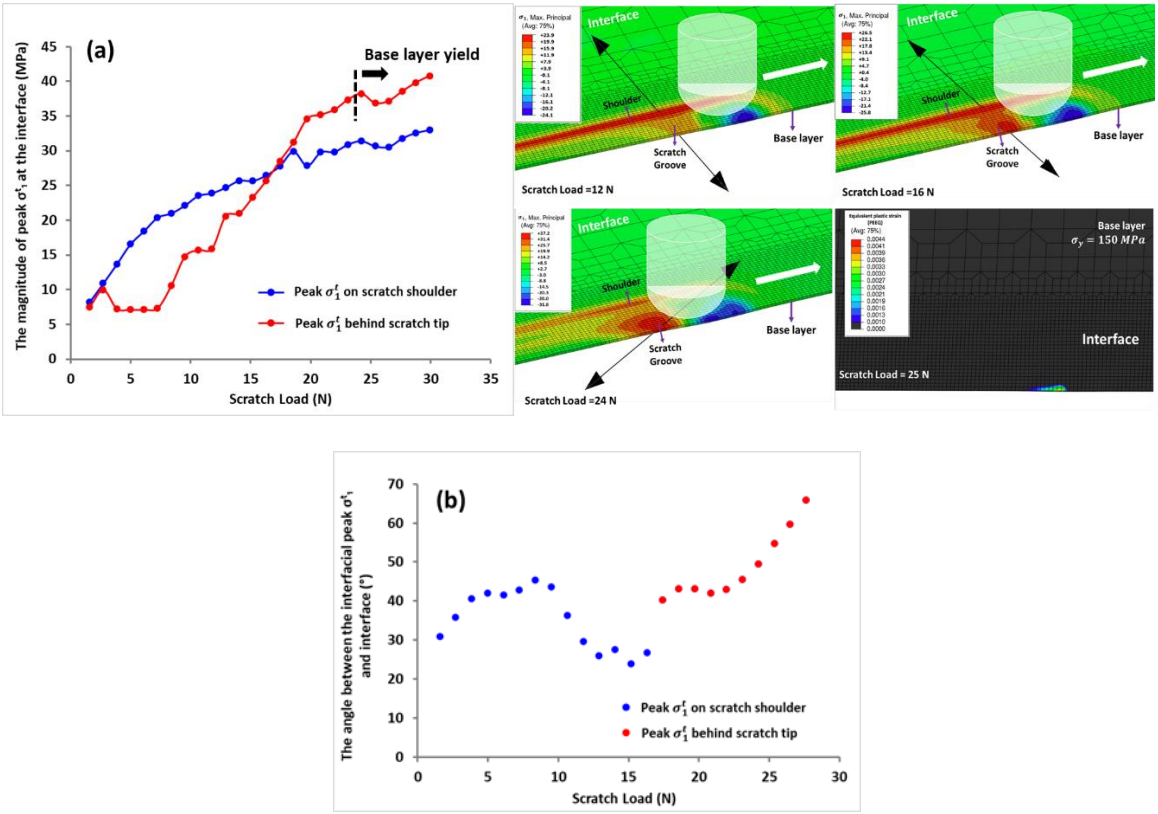

Figure V-9. The (a) magnitude and (b) angle of peak σ^{t_1} at the interface of the model system with σ_Y =30 MPa for the top layer and σ_Y =150 MPa for the base layer.

Note that the peak σ_1^t magnitude on the scratch shoulder is not always higher than that behind the scratch tip at the beginning of an increasing load scratch test. A good example is the case II scenario. In this case, the peak σ_1^t at the entire interface is located behind the scratch tip at the low loads as shown in Figure V-10 (a). Compared to Figure V-9 (a) (b), the magnitude and direction of peak tensile σ_1^t at the interface demonstrated

on Figure V-10 (a) (b) gives a completely different trend at a similar load range. This is because the base layer yields at a similar load range as the top layer at the beginning of scratch test due to its low yield stress. When both top and base layers have been extensively stretched, the peak σ_1^t begins to increase dramatically at 32 N as shown in Figure V-10 (a) due to stress concentration effect. However, this phenomenon is not observed in case I. The analyses of Cases I and II suggest that the differences in yielding and subsequent plastic deformation nature of each layer have a significant effect on the complex stress distribution not only at the interface but in the entire multilayer coating structure. It should be noted that there are many factors involved besides yield stress, such as modulus and strain hardening characteristics of both top and base layers, and top layer surface properties.

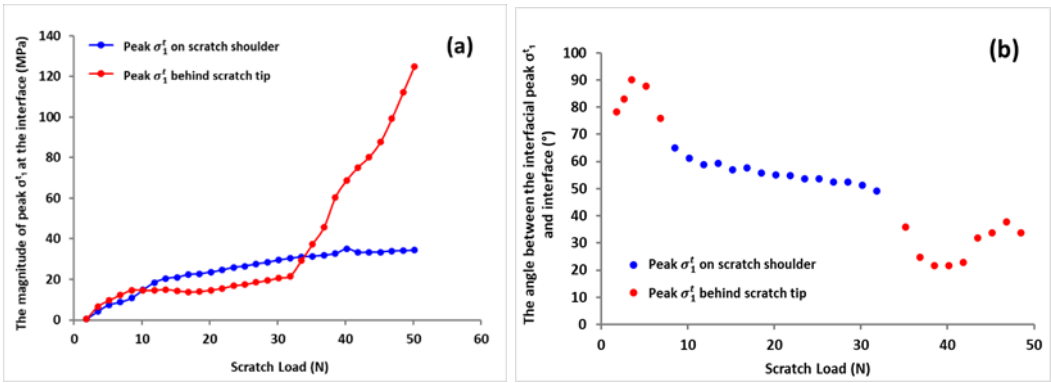

Figure V-10. The (a) magnitude and (b) angle of peak σ^{t_1} at the interface of the model system with σ_Y =150 MPa for the top layer and σ_Y =30 MPa for the base layer.

V.3.2.3. Parametric analysis

As explained above, due to the complexity of the delamination behavior in the bilayer coating system, a parametric study [119] was conducted to show how some key parameters affect the scratch induced delamination phenomenon. The key parameters to be analyzed include the modulus of base layer, the yield stress of both top and base layers, the strain hardening slope of the base layer, and the COF on the top surface. The von-Mises yielding criterion and isotropic hardening plasticity [120, 121] and the experimentally obtained piece-wise linear tensile and compressive true stress-strain curves were employed for the parametric study. The constitutive behaviors used for the following parametric study are shown in Figure V-11. The key parameters illustrated in this study are defined as those that could convey universal conclusions even other kept constitutive parameters changed.

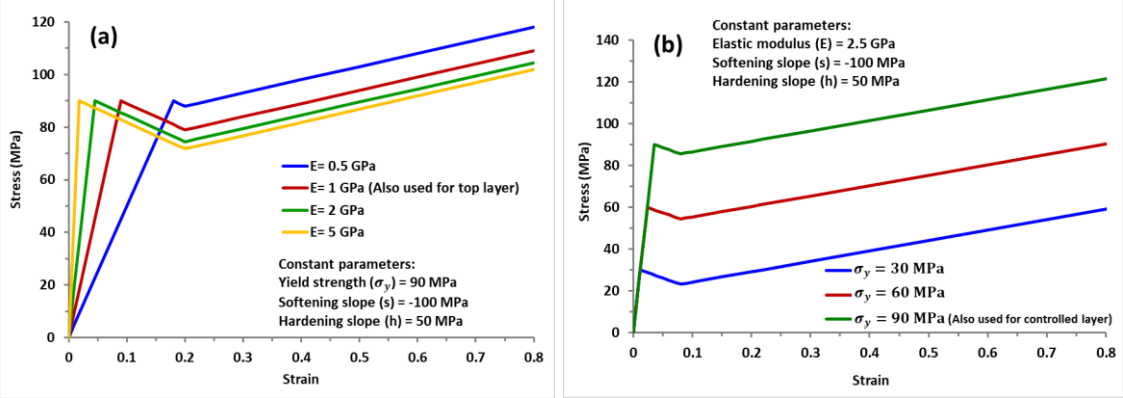

Figure V-11. The piece-wise linear stress-strain curves for the parametric study (a) effect of elastic modulus of the base layer (b) effect of the yield stress of both top & base layer (c) effect of strain hardening slope of the base layer, and (d) effect of COF on the top coating surface.

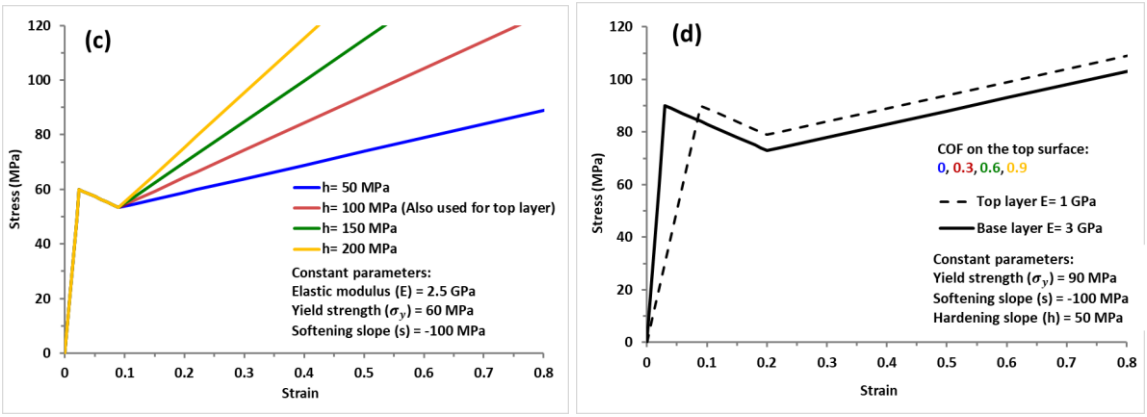

Figure V-11. Continued.

V.3.2.3.1. The effect of elastic modulus of the base layer

Figure V-12 presents the change in peak σ_1^t on the interface with increasing scratch normal load obtained via FEM modeling when the mechanical properties of the base layer are being systematically modified. Figure V-12 (a) shows that increase in elastic modulus of the base layer significantly increases the peak σ_1^t stress magnitude at the interface. Figure V-12 (b) demonstrates that the peak σ_1^t stress at the interface has a lower magnitude in the model system with a higher content of M1000 in the base layer. Therefore, the onset of delamination load in the scratch test will be higher in the model systems with more M1000 (Figure V-6 (c)). The parametric study results in Figure V-12 (a) and (b) support the experimental results obtained in Figure V-6 (c), suggesting that a base layer with lower elastic modulus will delay the delamination to a higher load in the linear increasing load scratch test.

As shown in Figure V-12 (c), the angle representing the direction of peak σ_1^t at the interface begins to show a trend after the location of the peak σ_1^t shifts to right behind the scratch tip. When the base layer is stiffer, the peak σ_1^t is more perpendicular to the interface, which suggests the delamination is more Mode-I dominant.

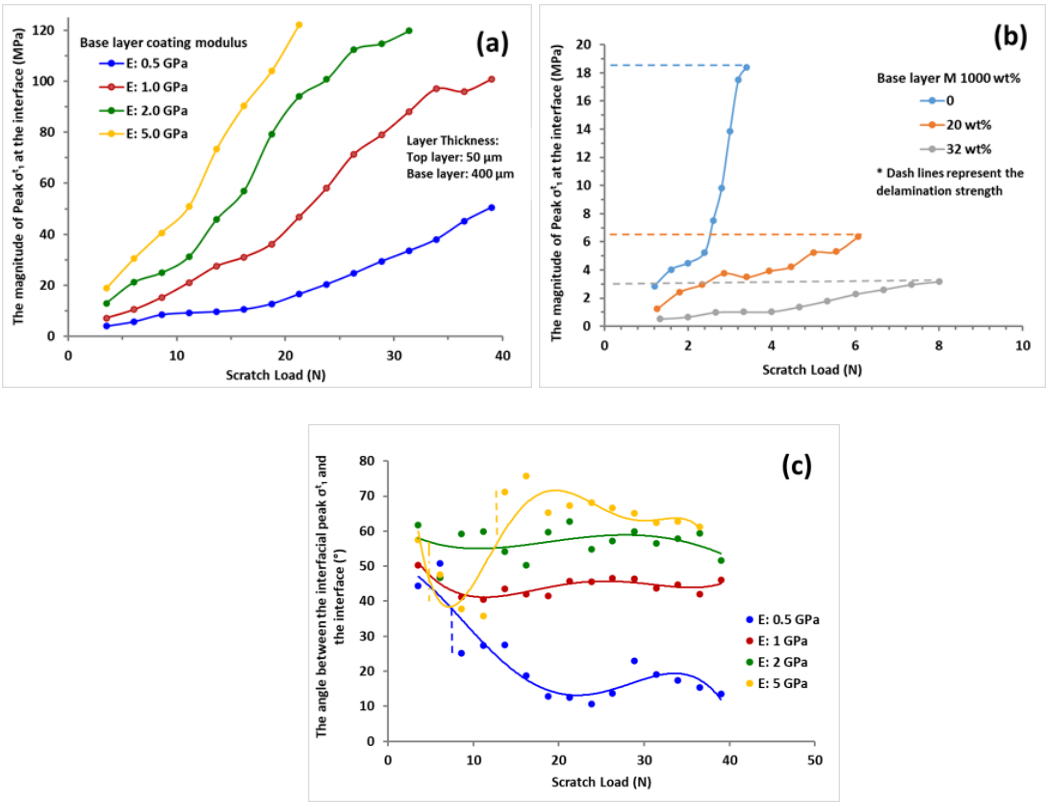

Figure V-12. (a) Effect of elastic modulus of the base layer on the peak σ^{t_1} magnitude at the interface, (b) effect of M1000 amount of the base layer on the peak σ^{t_1} magnitude at the interface, (The dash lines represent the delamination strength obtained through scratch tests and FEM modeling.), and (c) the angle between the direction of interfacial peak σ^{t_1} and interface. (The dash-dotted line reveals the load when the peak σ^{t_1} location at the interface shifts from behind the scratch tip to the shoulder region. The dash lines reveal the loads when peak σ^{t_1} location at interface shifts from scratch shoulder to tip behind.)

V.3.2.3.2. The effect of the yield stress of the top & base layer

Figure V-13 (a) shows that the peak σ_1^t magnitude decreases with the top layer yield stress at the interface at low loads Figure V-13 (b) shows the peak tensile σ_1^t magnitude at the interface decreases with the base layer yield stress at high loads. Since the top layer deforms first at the beginning of the scratch test, the resistance to plastic deformation of the top layer has a significant effect on the stress magnitude at the interface before it is fully deformed [54]. After the top layer deforms severely and the base layer begins to plastically deform, a higher yield stress of the base layer will delay the delamination by reducing the stress magnitude at the interface.

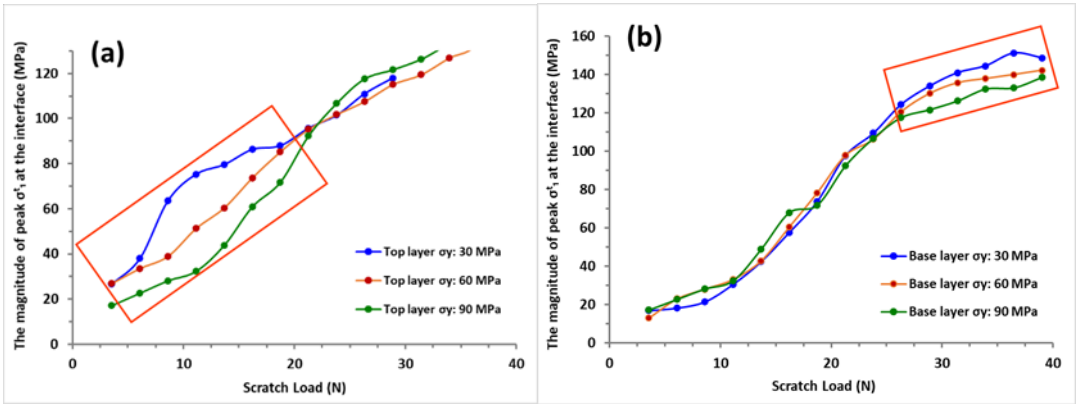

Figure V-13. The effect of the yield stress of (a) top layer and (b) base layer on the peak σ^{t_1} magnitude at the interface.

V.3.2.3.3. The effect of strain hardening behavior of the base layer

Figure V-14 (a) shows the increase in strain hardening slope of the base layer significantly increases the peak σ_1^t stress value at the interface and promotes delamination at high loads. As shown in Figure V-14 (b), an increase in the strain hardening slope of

the base layer makes the delamination mode more shear dominant after the peak σ_1^t begins to locate behind the scratch tip.

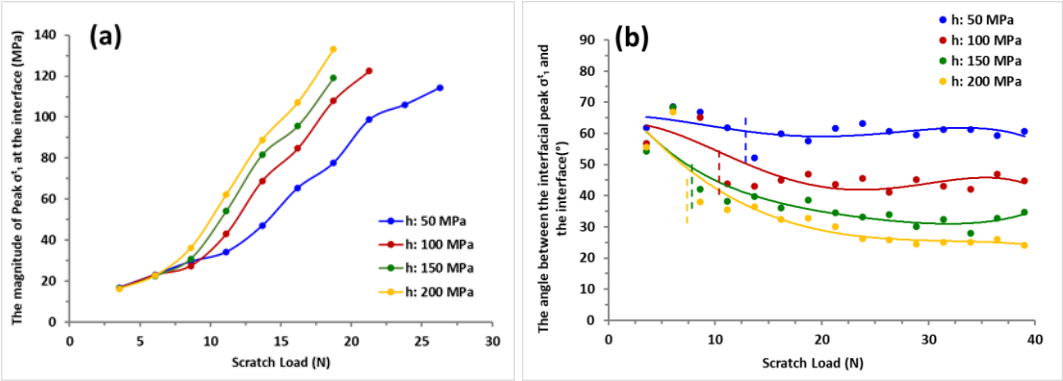

Figure V-14. The effect of strain hardening behavior of the base layer on the peak σ^{t_1} (a) the magnitude and (b) direction at the interface. (The dash lines indicate the loads when the peak σ^{t_1} location at interface shifts from scratch shoulder region to tip behind.)

V.3.2.3.4. The effect of the coefficient of friction (COF) on the top surface

Figure V-15 shows increasing COF on the top surface results in a higher peak σ_1^t magnitude at the interface [9]. The higher peak tensile stress with increase in COF may be attributed to the higher tangential stress and deformation induced, which can cause a significant stress-strain mismatch between the two layers. This would give rise to a higher interfacial stress.

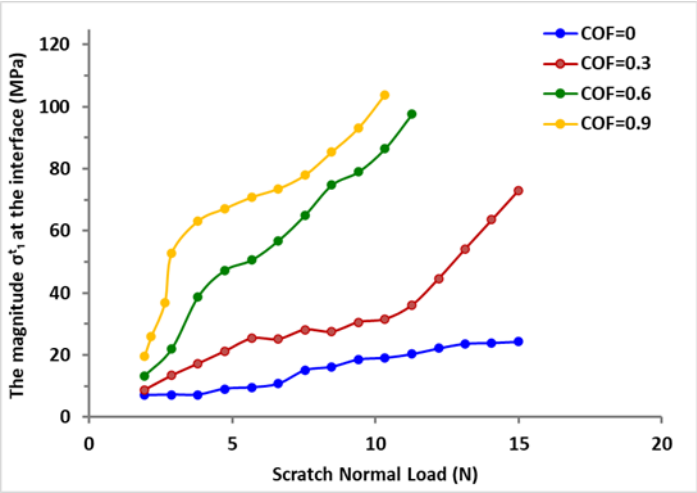

Figure V-15. The effect of coefficient of friction (COF) on the peak σ^{t_1} (a) the magnitude and (b) direction at the interface.

The delamination resistance of a multilayer system mainly depends on three factors, the interfacial bonding, and stress magnitude exerted, and the delamination mode at the interface. The current study aims at investigating how the geometry and constitutive parameters influence the stress generated at the interface. It should be noted that the model system with a lower stress magnitude generated at the interface does not equal to a higher delamination resistance.

CHAPTER VI

QUANTITATIVE MODELING OF SCRATCH BEHAVIOR OF AMORPHOUS POLYMERS AT ELEVATED TEMPERATURES[*]

The research strategy illustrated in Chapter II could be highlighted in Figure VI-1. The first part of this chapter briefly introduces the model system PC used in this study. The next part consists of different analytical models used in the simulation. The fundamentals of each model are first outlined, then the parameters corresponding to the modeled PC are listed. In the third part of this chapter, the experimental procedure is described in detail. Then the next part presents the single element axisymmetric model to apply the Arruda-Boyce model and 3D FEM scratch model for deformation prediction. Finally, the results and the usefulness of the present study are discussed.

[*] Part of this chapter was reprinted from Polymer, 197, Du, S., Mullins, M., Hamdi, M., Sue H.-J., Quantitative modeling of scratch behavior of amorphous polymers at elevated temperatures, 122504. Copyright (2020), with permission from Elsevier.

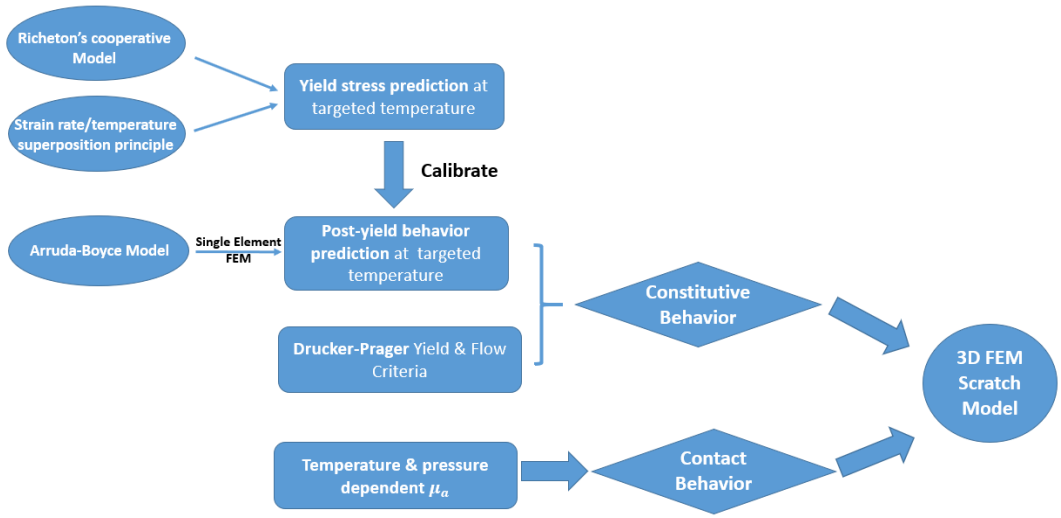

Figure VI-1. A chart summarizing the FEM modeling procedure.

VI.1. Model System

The experimental tests were performed on commercialized injection-molded polycarbonate (PC) samples provided by BASF SE (Ludwigshafen, Germany). They have dimensions of $150 \times 150 \times 3\ mm$ and $150 \times 150 \times 6\ mm$. First, the samples were dried in a vacuum for 6 h at 80 °C to remove the moisture effect. Then, they were annealed in a vacuum for 1 h at 160 °C, about 10 °C above their glass transition temperature (T_g ~148 °C), to eliminate chain orientation and prior thermal history. Finally, they were cooled to room temperature at a rate of 1.8 °C/min.

VI.2. Analytical Models

VI.2.1. Arruda-Boyce model for post-yield behavior

As highlighted in Figure VI-1, the post-yield behavior of PC is determined by axisymmetric single element FEM simulation using the Arruda-Boyce viscoplastic model [78, 100]. According to this model, the isotropic elastic behavior is modeled using

Hooke's law with the Hencky strain tensor. This model is represented by Equation (VI-1) below:

$$\boldsymbol{T^e} = \frac{1}{J^e}[2G \cdot \boldsymbol{h} + \lambda tr(\boldsymbol{h}) \cdot \boldsymbol{I}] \quad \text{(VI-1)}$$

Where $\boldsymbol{T^e}$ is the Cauchy elastic stress tensor, J^e is the elastic Jacobian of motion, G is the shear modulus, λ is Lamé's first parameter, and $\boldsymbol{h}$ is the Henky strain tensor. The stress tensor presented in Equation (VI-1) will be introduced in the Arruda-Boyce model for the single element FEM simulation. The elastic properties of the PC are presented in Table VI-1 [79, 100]:

Table VI-1. Elastic properties of PC in Arruda-Boyce model.

Young's modulus (E)	2300 MPa
Poisson's ratio (ν)	0.33

The plastic flow resistance consists of intermolecular resistance to segment rotation dominating near the yield point and entropic resistance to molecular alignment in the strain hardening region [79]. The intermolecular flow resistance is considered as the result of energy changes during the formation of kink pairs and the rotation of active kink corners along the principal tensile direction in the deformation process, based on the double-kink theory [122, 123]. The Arruda-Boyce model is described as Haward-Thachray mechanical analog [124], which is simply expressed as Eqn. (VI-2).

$$T^p = T^e - \frac{1}{J^e}F^e T^b F^e \quad \text{(VI-2)}$$

Where $\boldsymbol{T^p}$ is the visco-plastic stress tensor describing the viscoplastic flow rule of polymeric materials, $\boldsymbol{T^e}$ is the linear elastic stress calculated by Hooke's law of isotropic material in Equation (VI-1). $\boldsymbol{F^e}$ is the elastic deformation gradient, and $\boldsymbol{T^b}$ is the back stress of the Langevin spring described later in Equation (VI-7).

The non-linear plasticity flow rule in this model is expressed as:

$$\boldsymbol{D^p} = \dot{\gamma}^p \boldsymbol{N} \tag{VI-3}$$

Where $\boldsymbol{D^p}$ is the flow rate of the plastic deformation gradient, $\dot{\gamma}^p$ is the plastic shear strain rate, and $\boldsymbol{N}$ is the normalized tensor of plastic deviatoric stress. The expressions of $\dot{\gamma}^p$ and $\boldsymbol{N}$ are given in terms of the deviatoric visco-plastic stress tensor ($\boldsymbol{T^p_{dev}}$) as follows:

$$\dot{\gamma}^p = \dot{\gamma}_0 \cdot exp\left[-\frac{As}{k\theta}\left(1 - \left(\frac{\tau}{s}\right)^{5/6}\right)\right] \;\; ; \;\; \tau = \sqrt{\frac{\boldsymbol{T^p_{dev}}:\boldsymbol{T^p_{dev}}}{2}} \tag{VI-4}$$

$$\boldsymbol{N} = \frac{1}{\sqrt{2}\tau}\boldsymbol{T^p_{dev}} \tag{VI-5}$$

Where $\dot{\gamma}_0$ is a pre-exponential factor, A is the zero stress level activation energy, k is the Boltzmann constant, θ is the absolute temperature, s is the athermal shear stress and τ is the effective equivalent shear strength taking the temperature, strain rate dependent softening behavior into account. Previous experimental studies showed that the non-linear strain softening behavior of PC is associated with a 'preferred' molecular chain structure in the flow state. Therefore the PC specimens at different initial heat treatments soften to nearly the same strength level in the same testing conditions [125, 126]. The flow

rule of athermal shear stress of amorphous polymers related to plastic shear strain rate ($\dot{\gamma}^p$) is as follows [79, 101]:

$$\dot{s} = h(1 - \frac{s}{s_{ss}})\,\dot{\gamma}^p \tag{VI-6}$$

Where h is the softening slope, and $\dot{s}$ and s_{ss} refer to the rate of athermal shear stress and the "preferred" molecular state of s, respectively. When the molecules align along the deformation direction in the strain hardening regime, the plastic flow resistance becomes mainly due to the entropic resistance from molecular alignment. Due to the configurational entropy change, this resistance can be determined using the back stress model with 8 non-Gaussian chains as follows [100, 127, 128]:

$$T_i^b = \frac{1}{3} C_r \sqrt{N} \mathcal{L}^{-1}\left[\frac{\Lambda_{chain}^P}{\sqrt{N}}\right] \frac{\Lambda_i^{p^2} - \frac{1}{3} I_1}{\Lambda_{chain}^p} \tag{VI-7}$$

$$I_1 = \Lambda_1^{p^2} + \Lambda_2^{p^2} + \Lambda_3^{p^2} \quad \text{and} \quad \Lambda_{chain}^p = \left(1/\sqrt{3}\right) I_1^{1/2}$$

Where T_i^b is back stress component, C_r is the rubber modulus, N is the chain stretch parameter, $\mathcal{L}$ is the Langevin function, Λ_{chain}^p is the stretch on any individual chain in the eight-chain network, and $\Lambda_i^{p^2}$ are the eigenvalues of the plastic left Cauchy stretch tensor. By determining the expressions of strain softening and strain hardening, the model is capable of describing the post-yield behavior of the examined amorphous polymer.

The parameters of the Arruda-Boyce viscoplastic model corresponding to PC post-yield behavior are presented in Table VI-2 below [100, 129]. These parameters will be included in the axisymmetric single element FEM model.

Table VI-2. Parameters of the Arruda-Boyce model for the post-yield behavior of PC model system.

Pre-exponential factor ($\dot{\gamma}_0$)	2×10^{15} (s^{-1})
Initial Softening slope (h)	500 MPa
Shear stress state ratio (S_{ss}/S_0)	0.78
Zero stress level activation energy (A)	3.93×10^{-27} m^3
Rubber modulus (C_r)	18.0 MPa
Chain stretch parameter (N)	2.78

Our previous studies found that the elastic modulus in the range of 1.65 GPa – 4 GPa has minimal effect on scratch depth specific to the scratch tip geometry chosen [38, 130]. Therefore, the effect of temperature and strain rate on the elastic modulus would be insignificant and will not be considered in this study. Although the Arruda-Boyce model can effectively describe the post-yield behavior of amorphous polymers, it has limited capabilities in accurately predicting their yield stresses, especially at high strain rates [78, 83]. This limitation will be overcome after using the Richeton cooperative model for calibration.

VI.2.2. Richeton cooperative model for yield stress

As shown in Figure VI-1, the Richeton cooperative model is used to accurately predict the effect of temperature and strain rate on the yield stress of amorphous polymers. This model indicates that the yield stress below T_g can be written as [51]:

$$\sigma_y(T < T_g) = \sigma_i(0) - mT + \frac{2kT}{V}\sinh^{-1}\left(\dot{\varepsilon}\Big/\dot{\varepsilon}_0 exp\left(-\frac{\Delta H_\beta}{RT}\right)\right)^{1/n} \quad \text{(VI-8)}$$

Where $\sigma_i(0)$ is the athermal internal yield stress (i.e. at 0 °K), m reflects the yield stress-temperature linearity, T is the temperature, R is gas constant, V is the activation volume, $\dot{\varepsilon}$ is the strain rate, $\dot{\varepsilon}_0$ is a constant pre-exponential strain rate, ΔH_β is the activation energy of the β loss peak, and n is a parameter describing the cooperative movement of the polymer chains. Material parameters V and n characterize the state of the polymer structure. By setting the reference temperature to room temperature ($25°C$), and dividing both sides of Eqn. (VI-8) by $T_{25°C}$, the following equation is obtained:

$$\frac{\sigma_y}{T_{25°C}} = \frac{\sigma_i(T_{25°C})}{T_{25°C}} + \frac{2k}{V}\sinh^{-1}\left(\frac{\dot{\varepsilon}}{\dot{\varepsilon}^*(T_{25°C})}\right)^{1/n} \quad \text{(VI-9)}$$

where

$$\sigma_i(T_{25°C}) = \sigma_i(0) - m \cdot T_{25\,°C} \quad \text{(VI-10)}$$

$$\dot{\varepsilon}^*(T_{25°C}) = \dot{\varepsilon}_0 \cdot exp\,(-\frac{\Delta H_\beta}{RT}) \quad \text{(VI-11)}$$

The parameters of the Richeton model that correspond to PC material will be determined later in section VI.5.2 by applying the time-temperature superposition principle to the experimental results. The yield stress accurately determined using the Richeton model will be used to calibrate the post-yield behavior determined previously using the Arruda-Boyce model.

VI.2.3. Calibration of Arruda-Boyce model using Richeton yield stress

Figure VI-2 highlights the method used to calibrate the temperature and strain rate dependent post-yield behavior obtained by the Arruda-Boyce model using the yield stress

value determined by the Richeton model. The calibration is made by shifting the whole post-yield curve obtained by the Arruda-Boyce model so that its onset corresponds to the yield stress found by the Richeton model.

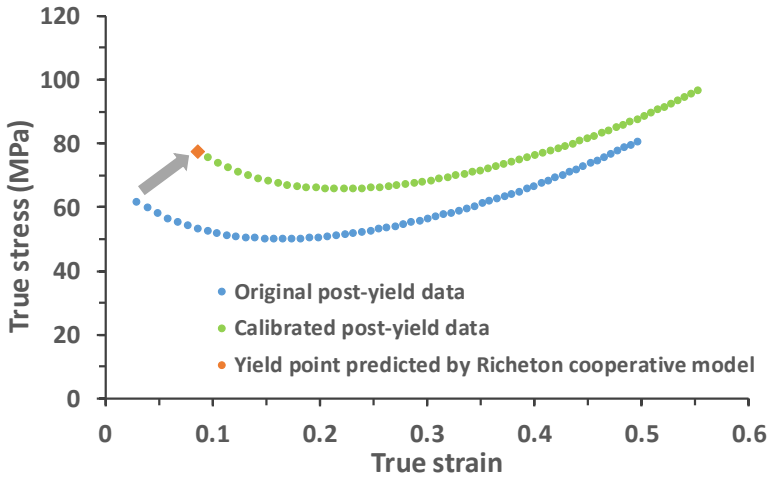

Figure VI-2. Calibration of yield point and post-yield behavior predicted by the Arruda-Boyce model with the Richeton model.

VI.2.4. Model for temperature and pressure-dependent adhesion COF

According to Chung's work, the adhesion coefficient of friction (μ_a) between a solid polymer and a metallic surface is temperature-dependent when the pressure is as low as 0.5 MPa, but becomes almost temperature-independent at higher pressures [131]. Therefore, the effect of temperature and pressure on the friction between PC and steel can be modeled using the equation below [46, 132, 133]:

$$\begin{cases} \mu_a(T) & P_r \leq 0.5\ MPa \\ \mu_a(P_r) = \frac{\tau_0}{P_r} + \alpha\ ; & P_r > 0.5\ MPa \end{cases} \quad \text{(VI-12)}$$

Where τ_0 is the shear yield stress at $P_r = 0\ MPa$ and α is a pressure coefficient. The value of $\mu_a(T)$ was measured by the COF measurement procedure described above [51]. The relation between α and the pressure sensitivity parameter (α_p) in Richeton's study is:

$$\alpha = \frac{\sigma_y^c - \sigma_y^t}{\sqrt{3}\cdot(\sigma_y^c + \sigma_y^t)} = \frac{\alpha_p}{3\sqrt{3}} \tag{VI-13}$$

Where σ_y^c and σ_y^t refer to the compressive and tensile yield stresses, respectively. It was previously shown that the effect of temperature on α_p is insignificant [134]. The relation between the two pressure parameters indicates that the pressure effect on the surface properties of a solid polymer is physically related to that on its bulk properties, and α can be assumed to be temperature independent for PC in a certain range. This model will be used in the FEM analysis to simulate the dependence of the surface COF on the test temperature and pressure. Its parameters for PC material have the following values (Table VI-3) demonstrated from a previous study [46]:

Table VI-3. Parameters for PC of the proposed COF model from Hossain et al. [46].

Shear yield stress (τ_0)	38.32 MPa
Pressure coefficient (α)	0.06

After identifying the appropriate models for post-yield behavior and surface COF, the Drucker-Prager model characterizing the deformation caused by scratch damage in the 3D FEM scratch model was described below.

VI.2.5. Drucker-Prager model for scratch-induced damage

The Drucker-Prager plasticity model in ABAQUS 2017® is adopted to simulate the plastic behavior of the model system [135-138]. As illustrated in Chapter V, the three key parameters to characterize the hydrostatic pressure-dependent constitutive behavior of materials, namely the angle of friction β, flow stress ratio K, and dilation angle ψ. The angle of friction β can be obtained via Equation (VI-14), it can be found that $\beta = \alpha_p$. Since the pressure sensitivity parameter (α_p) depends slightly on temperature below T_g, it is reasonable to assume the angle of friction (β) is nearly the same at different temperatures below T_g [51].

$$\beta = 3\frac{\sigma_y^c - \sigma_y^t}{\sigma_y^c + \sigma_y^t} \quad \text{(VI-14)}$$

A previous study showed that the friction angle (β) can be used to determine the stress ratio (K) for PC at room temperature in the range of $0.778 \leq K \leq 1$ according to the following equation [46]:

$$K = \frac{1}{1+\frac{1}{3}tan\,\beta} \quad \text{(VI-15)}$$

Therefore, the parameters of the Drucker-Prager model for PC at temperatures below T_g are determined and summarized in Table VI-4 below. Previous studies showed that the maximum inelastic volume change of PC at various temperatures below T_g is negligible [139, 140]. Therefore, the dilation angle of the PC can be approximated as $\psi = 0$ below T_g.

Table VI-4. Parameters of Drucker-Prager model for PC at temperatures below T_g from Hossain [49].

Angle of Friction (β)	27.13°
Flow Stress Ratio (K)	0.85
Dilation Angle (Ψ)	0

The effect of temperature and strain rates on yield and post-yield behavior is considered using the Arruda-Boyce model calibrated with the Richeton cooperative model. Then, the yield and post-yield data were input into the Drucker-Prager model in ABAQUS 2017® for the quantitative modeling of the scratch-induced deformation. Also, it should be noted that the strain calibration in the elastic region is not required because the Drucker-Prager model in ABAQUS 2017® considers only the plastic strain in the FEM modeling.

VI.3. Experimental Procedure

VI.3.1. Scratch test

Scratch tests were performed according to ASTM D7027/ISO 19252 standard [18, 141] using a G5 scratch tester provided by Surface Machine Systems (College Station, TX). These standards are commonly used to assess the scratch resistance of polymeric materials [29]. The scratch tip consists of a stainless-steel spherical tip with a diameter of 1 mm. To control the test temperature, the machine is enclosed in the custom-built environmental chamber presented in Figure VI-3. The test temperature can be maintained up to 120 °C using a PCB heater underneath the sample and a radiant heater inside the

chamber. The surface temperature is precisely and uniformly controlled within $\pm$ 2 °C using an Omega commercial pulse width modulation controller CN76000.

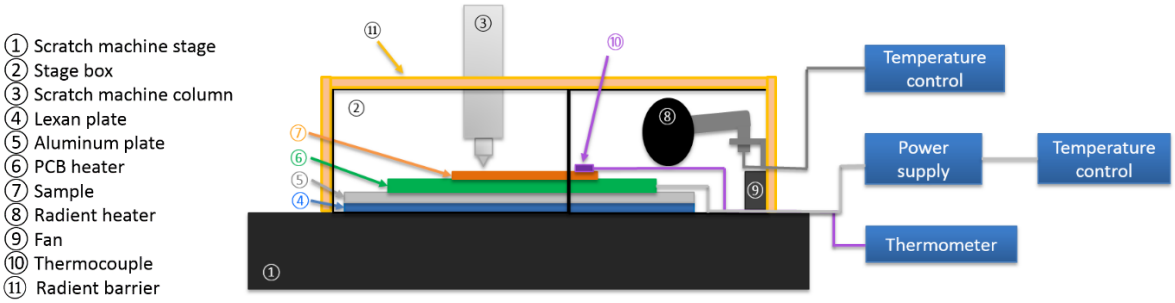

Figure VI-3. Scratch machine heating system and the environmental chamber.

Scratch tests were conducted at temperatures of 25, 60, and 100 °C. The applied linearly increasing normal load from 1 N to 35 N at a constant speed of 100 mm/s was performed over a length of 100 mm. The load range was chosen to generate a smooth scratch groove without tearing damages. To avoid scratch recovery in cyclic thermal conditions, only one scratch test was performed on each sample. At least three tests were carried out at each test temperature. Scratch-induced deformation was observed using a Keyence® VK9700 violet laser scanning confocal microscope (LSCM) 24 hours after removing the specimens from the environmental chamber [2, 96]. A previous study showed that this period was sufficient to allow for the viscoelastic recovery of PC [46].

VI.3.2. Surface coefficient of friction (COF)

The same setup shown in Figure VI-3 was employed to determine the adhesion coefficient of friction (μ_a) of the samples at different temperatures. A flat, smooth, and

self-aligned tip with a square surface of 10 × 10 mm was used to minimize the sliding-induced deformation on the samples [30]. At each temperature, five measurements were taken at a constant normal load of 5 N over a distance of 100 mm and at a speed of 100 mm/s. The test was applied at a constant contact pressure of approximately 0.05 MPa. Three tests were performed on each temperature.

VI.3.3. Uniaxial compression test

The uniaxial compression test in this chapter follows the procedure in CHAPTER IV. The tests were performed at temperatures of 25, 60, and 100 °C and strain rates of 4×10^{-4} , 5×10^{-3}, and 5×10^{-2} s^{-1} for each temperature.

VI.4. FEM Models

VI.4.1. Single element axisymmetric compressive simulation

As indicated in Figure VI-1, the Arruda-Boyce model was introduced in a single-element axisymmetric compressive simulation by user subroutine (VUMAT) to determine PC post-yield behavior at various temperatures and strain rates. This geometric model is presented in Figure VI-4. It consists of a single CAX4R element in the x-y plane with dimensions of 15 × 30 mm, representing the half cross-section of a cylindrical sample with a radius of 15 mm and a height of 30 mm. Its boundary conditions consist of a symmetry axis and the fixed bottom in the y-direction, respectively. The displacement (ΔU_y) was applied only on the upper edge to mimic the displacement control compression test at a constant speed. Based on the definition, the strain rate could be determined using Equation (VI-16) [142]:

$$\dot{\varepsilon} = \frac{d\varepsilon}{dt} = \frac{(\Delta U_y / L_0)}{t_s} \quad \text{(VI-16)}$$

Where t_s is the compression time in simulation and L_0 is the element dimension in the compression direction. This model was developed using a commercial FEM package [143].

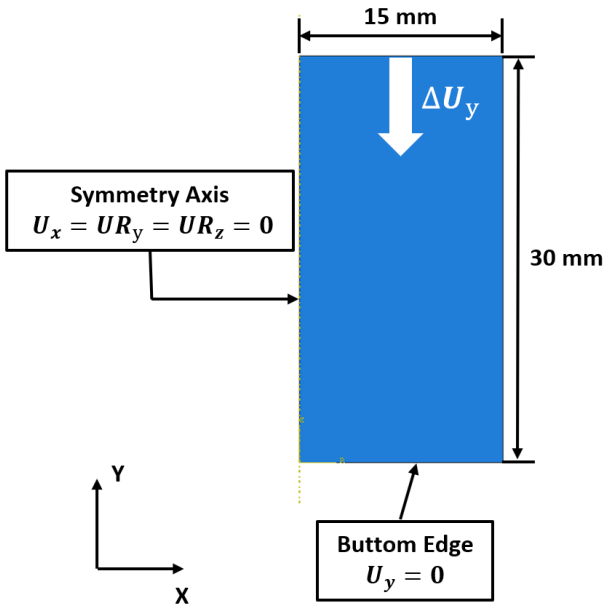

Figure VI-4. Geometry and boundary conditions of the single element axisymmetric compressive model.

VI.4.2. 3D FEM model for scratch test

A 3D scratch model for PC was built as described in previous studies with a FEM package [30, 61, 99]. The numerical computation domain and boundary conditions are shown in Figure VI-5. The critical length (A to B) is composed of 512 elements in the dimension of 22.8 μm × 28.1 μm × 33.3 μm to obtain accurate results in reasonable computation time. As shown in Figure VI-1, the Drucker-Prager model is incorporated

into the 3D scratch model to simulate the plastic behavior of the model system. And a linear elastic constitutive relationship with secant modulus and Poisson's ratio obtained from uniaxial compression test is considered to model the elastic behavior [49]. The viscoelastic recovery of the material, as well as the scratch-induced crack and fish-scale patterns, are not considered in this model. Furthermore, it has been shown that the temperature rise caused by heat generation in the ASTM standard scratch test is negligible at a speed of 100 mm/s below 40 N [144, 145]. Therefore, the heat generation in a single scratch path could be ignored in the FEM modeling.

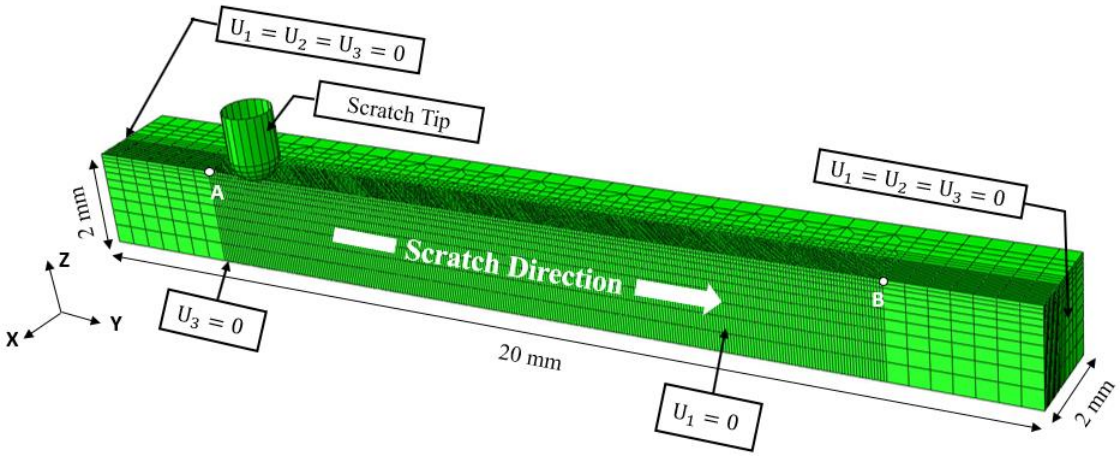

Figure VI-5. Geometry and boundary conditions of the FEM scratch model.

VI.5. Results & Discussion

VI.5.1. Prediction of the post-yield behavior

Figure VI-6 compares the post-yield behavior obtained using Arruda-Boyce visco-plastic model with the experimental results from the uniaxial compression test at a strain

rate of $\dot{\varepsilon} = 4 \times 10^{-4}\ s^{-1}$. It is observed that the yield stress decreases with temperature. Also, the modeled non-linear strain softening and strain hardening curves (dashed line) are generally consistent but slightly shifted compared to the experimental ones (solid line). This will be eliminated after the calibration of the post-yield behavior using the Richeton cooperative model in Section V.4.3. Also, the predicted strain-softening slopes at 60 °C and 100 °C are lower than the experimental results. This is explained by a more predominant stress relaxation effect due to the extremely low strain rate chosen for the tensile and compression tests [101, 146]. However, a previous parametric study showed that strain softening has an insignificant effect on the scratch depth and width [6]. Therefore, this difference in strain softening is not expected to meaningfully affect the modeled scratch deformation. Similarly, the predicted strain hardening at 100 °C starts deviating from the experimental results at a strain of approximately $\varepsilon = 0.36$. This can be explained by accelerated stress relaxation at high temperatures [146].

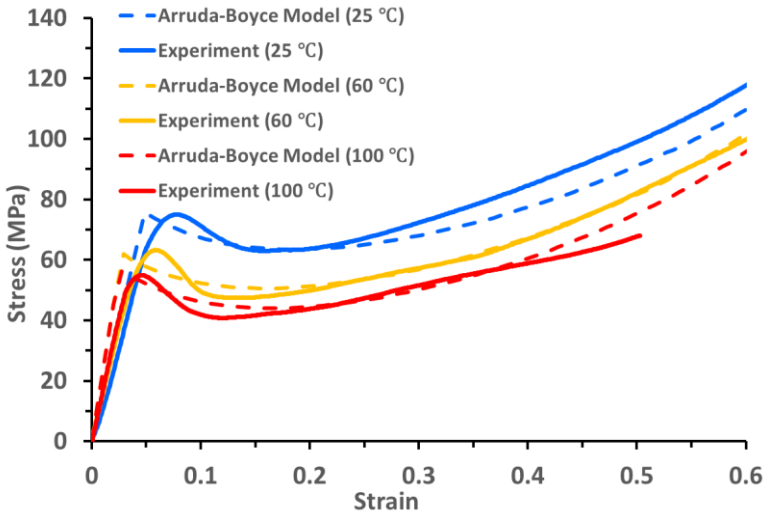

Figure VI-6. Experimental and predicted post-yield behavior at different temperatures and a strain rate of $4\times10^{-4}\ s^{-1}$.

Figure VI-7 shows the predicted stress-strain curves obtained using Arruda-Boyce viscoplastic model for different temperatures and strain rates. The figure clearly shows that the yield and post-yield stresses increase at lower temperatures and higher strain rates. This is consistent with previous studies [86, 147-149]. Also, for each temperature, the change in non-linear strain hardening with strain rate decreases at high strains. This is consistent with the experimental results presented in Figure VI-6.

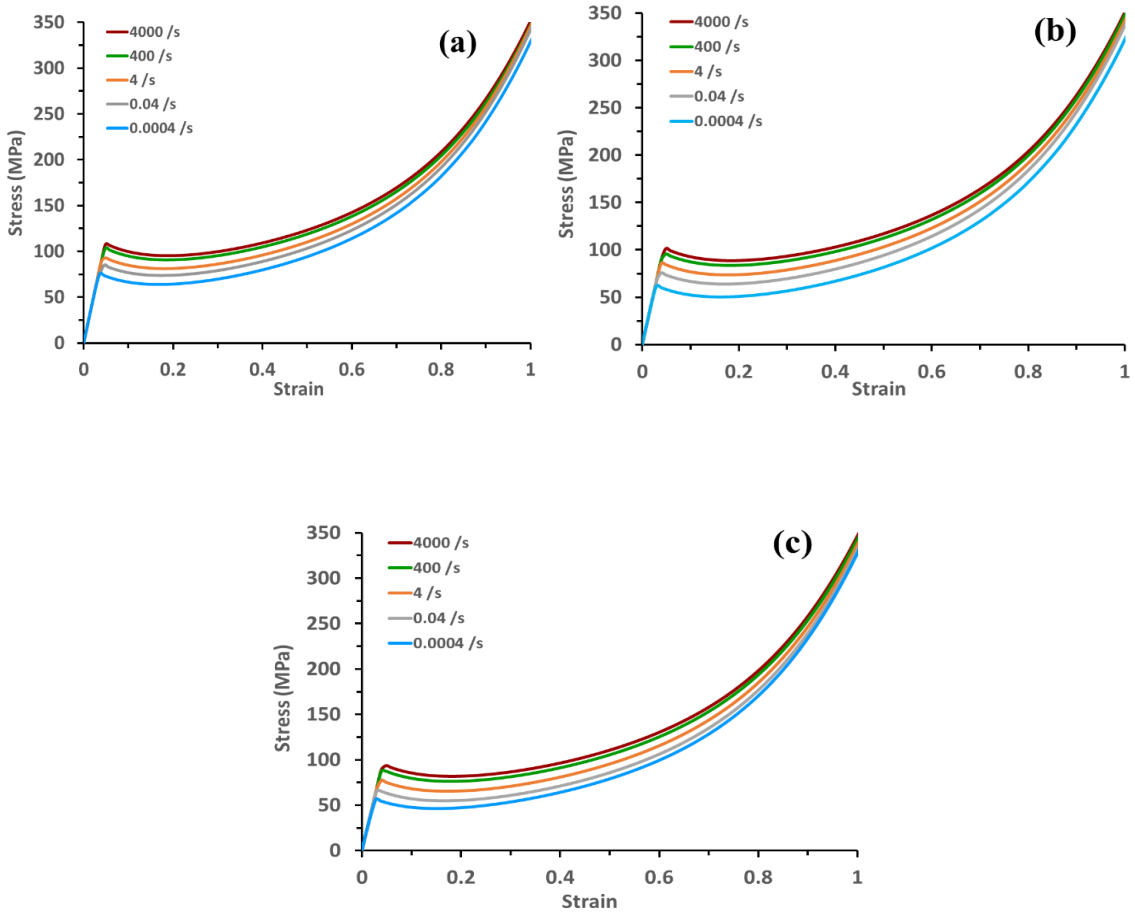

Figure VI-7. Post-yield behavior predicted using Arruda-Boyce model at (a) 25 °C, (b) 60 °C, and (c) 100 °C.

VI.5.2. Prediction of the yield stress

Table VI-5 summarizes the compressive yield stress values of PC obtained from the uniaxial compression test at various temperatures and strain rates. It is observed that the yield stress increases with a higher strain rate and lower temperature. This same observation was made for the predicted results highlighted in Figure VI-7 which shows their consistency.

Table VI-5. Experimental compressive yield stress (MPa) of PC at various temperatures and strain rates.

		$\dot{\varepsilon}$ (s^{-1})		
		$\mathbf{4 \times 10^{-4}}$	$\mathbf{5 \times 10^{-3}}$	$\mathbf{5 \times 10^{-2}}$
T (°C)	**25**	77.5 ± 1.7	82.7 ± 0.8	85.0 ± 1.1
	60	64.4 ± 2.5	72.4 ± 2.3	72.6 ± 0.4
	100	56.4 ± 4.2	61.5 ± 6.3	67.4 ± 3.3

The time-temperature superposition principle of yield stress presented in Equation below was applied to the obtained results [91]:

$$\begin{cases} \Delta(log\ \dot{\varepsilon}) = log\ \dot{\varepsilon}\left(T_{ref}\right) - log\ \dot{\varepsilon}(T) \\ \Delta\left(\frac{\sigma_y}{T}\right) = \frac{\sigma_y(T_{ref})}{T_{ref}} - \frac{\sigma_y(T)}{T} \end{cases} \quad \text{(VI-17)}$$

The yield stress data at three strain rates were shifted to establish a master curve for a reference temperature of $T_{ref} = 25$ °C. Results are shown as Eyring plots (σ_y/T v.s. $\log \dot{\varepsilon}$) in Figure VI-8 (a).

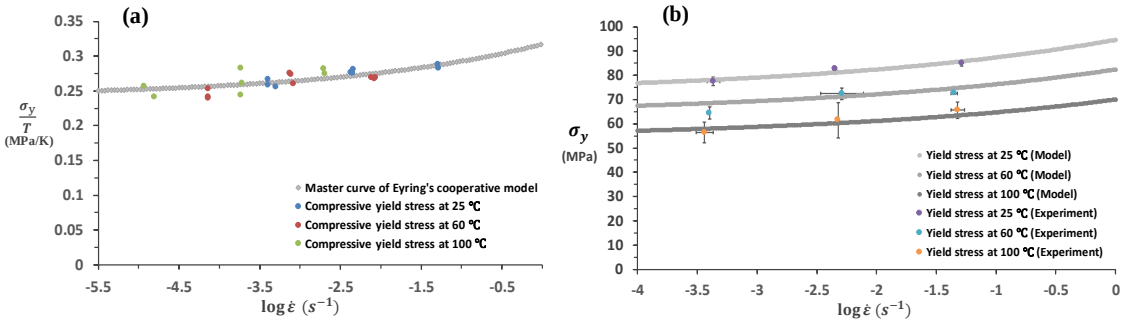

Figure VI-8. (a) Master curve of Eyring cooperative model for PC and shifted test data (b) Yield stress predicted by Eyring cooperative model compared with experimental results.

To obtain the four parameters in the Richeton model shown in Equation (VI-9) (namely n, V, $\dot{\varepsilon}^*(T_{25℃}), and\ \sigma_i(T_{25℃})$), a curve-fitting software was employed on all the data points at the reference temperature $T_{ref} = 25$ ℃. Then $\dot{\varepsilon}_0$ and m in Equation (VI-8) were calculated using Equations (VI-10) and (VI-11) with $\sigma_i(0)$ and ΔH_β values of PC taken from the literature [86, 91]. All the values of Richeton model parameters in Equation (VI-8) for PC material are summarized in Table VI-6.

Table VI-6. Measured parameters of Richeton cooperative model for PC.

Activation volume (V)	$3.70 \times 10^{-29}\ m^3$
Cooperative movement parameter (n)	5.88
Athermal internal yield stress ($\sigma_i(0)$) [86, 91]	145 MPa
Activation energy of the β loss peak (ΔH_β) [86, 91]	$40000\ J/(K \cdot mol)$
pre-exponential strain rate ($\dot{\varepsilon}_0$)	$7.13 \times 10^{12}\ s^{-1}$

Table VI-6. Continued.

Internal yield stress parameter (*m*)	0.24
Boltzmann constant (*k*)	$1.38 \times 10^{-29}\ MPa \cdot m^3/K$

Figure VI-8 (b) shows the yield stress predicted by the Richeton cooperative model at the targeted temperatures matching nearly all the experimental results. This demonstrates the consistency of this model in predicting the experimental yield stress.

VI.5.3. Calibration of the post-yield behavior

As explained previously, the post-yield behavior obtained using the Arruda-Boyce viscoplastic model (Figure VI-7) was calibrated using the Richeton model (Figure VI-8b). This was performed by shifting the whole post-yield curve to the yield point predicted by the Richeton model. An illustration of the calibration of the results at a temperature of 25 ℃ and a strain rate of $4\times 10^{-4}\ s^{-1}$ was previously shown in Figure VI-2. The final calibrated plastic behavior of PC at different temperatures and strain rates are presented in Figure VI-9. These curves will be introduced in Drucker-Prager model to accurately simulate the scratch-induced deformation of PC.

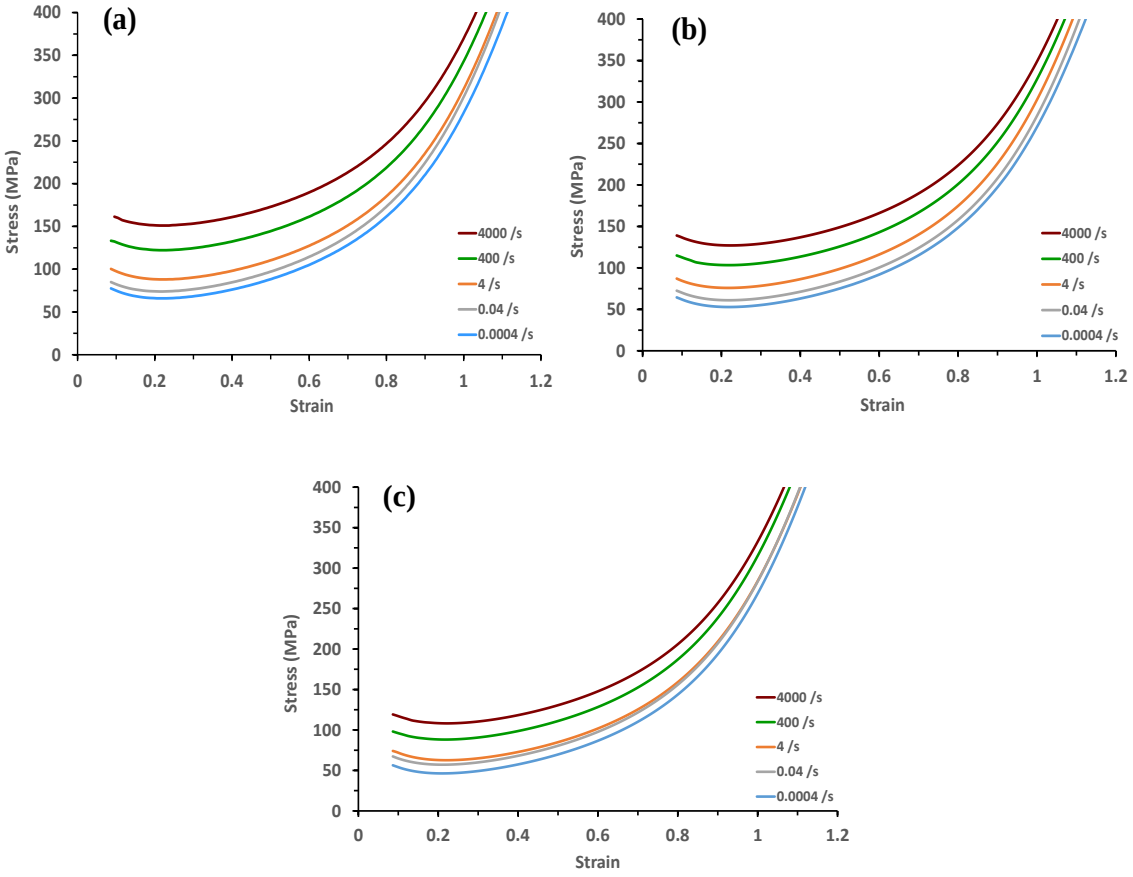

Figure VI-9. Arruda-Boyce post-yield behavior calibrated using Richeton model at (a) 25 °C, (b) 60 °C, and (c) 100 °C.

VI.5.4. Prediction of the surface COF

Figure VI-10 presents the adhesion coefficient of friction (μ_a) measured experimentally at the three considered temperatures. The contact pressure of these measurements is approximately 0.05 MPa. The dashed line is the curve fitting of the data points to show the general trend of μ_a varying with temperature. The figure clearly shows a slight increase in surface COF with temperature. The results are consistent with the findings of Chung and coworkers [131]. A previous study has shown that even with a

small difference in COF, the depth can change significantly [7], which is critical to the quantitative prediction of the micron-sized scratch groove formation. COF is dominated by two factors: the actual contact area between the sliding surfaces and the shear strength of the sliding material. Temperature increases the actual contact area between the contact surfaces due to the polymer softening induced by temperature rise [150]. Even though the shear strength of PC decreases with temperature, the slight drop in shear strength due to temperature rise is not significant in COF magnitude under low contact pressures [151].

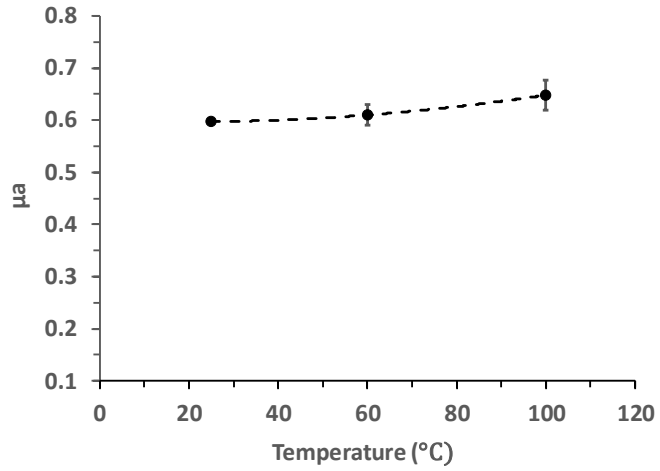

Figure VI-10. Variation of the adhesion coefficient of friction (μ_a) between PC and stainless steel with temperature at a contact pressure of ~ 0.05 MPa.

Figure VI-11 shows the values of the adhesion coefficient of friction predicted with Equation (VI-12) for the 3D FEM scratch model. $\mu_a(T)$ was used as the upper limit of the COF value to avoid unrealistic high values obtained when Pr is very low. The pressure dependent COF at $P_r = 75$ MPa is very close to the COF measurement results at

$P_r = 0.05$ MPa. To simplify the problem, the $\mu_a(T)$ at $P_r = 0.5$ MPa was determined by linearly interpolating these data, and $\mu_a(T)$ in the range of $P_r \leq 0.5$ MPa can be assumed to be pressure-independent. When $P_r > 0.5$ MPa, the COF was shown to have a reverse relationship with Pr, which is due to the reduction of actual contact area as Pr rises in the elastic-plastic contact process [150, 151].

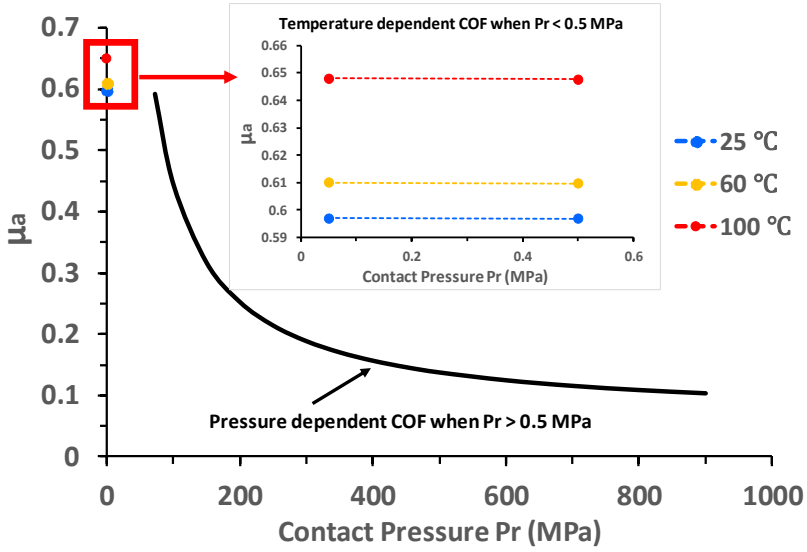

Figure VI-11. Adhesion coefficient of friction μ_a input into 3D scratch model.

VI.5.5. Prediction of the scratch-induced deformation

The predicted COF and calibrated post-yield behavior were introduced in the Drucker-Prager model to characterize the deformation caused by scratch damage. Figure VI-12 compares the residual scratch depth on PC model systems obtained experimentally with those predicted using the FEM model. A good agreement is obtained between the experimental and predicted results. This clearly demonstrates the effectiveness of the

modeling approach and the adequate assumptions involved in modifying the constitutive model parameters.

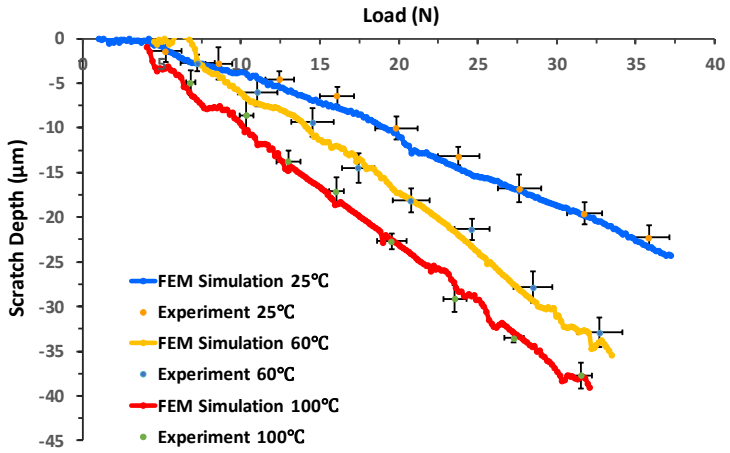

Figure VI-12. Experimental and modeled scratch depth values on PC at the three examined temperatures.

The residual cross-section scratch grooves obtained from FEM modeling and laser confocal microscope (LSCM) scanning at a normal load of 20 N are compared in Figure VI-13. The dashed black lines in the figures were used to mark the horizontal surface and the peak of the shoulders. The FEM approach proposed in this study can predict the groove's shape and depth precisely, with only minor differences at elevated temperatures. It is noted that the current modeling approach under-predicts the scratch width and shoulder height build-up [46]. This is due to the fact that this Lagrangian FEM model ignores the material accumulation on the shoulder flowing from the tip front [152]. By applying the Eulerian method in our future FEM modeling, this issue might be resolved

[153]. Furthermore, it should be noted that the differences in groove width and shoulder height between experimental and modeling results become larger when the test temperature is increased. This is probably due to the aforementioned more pronounced softening of PC at higher temperatures [41, 74, 152].

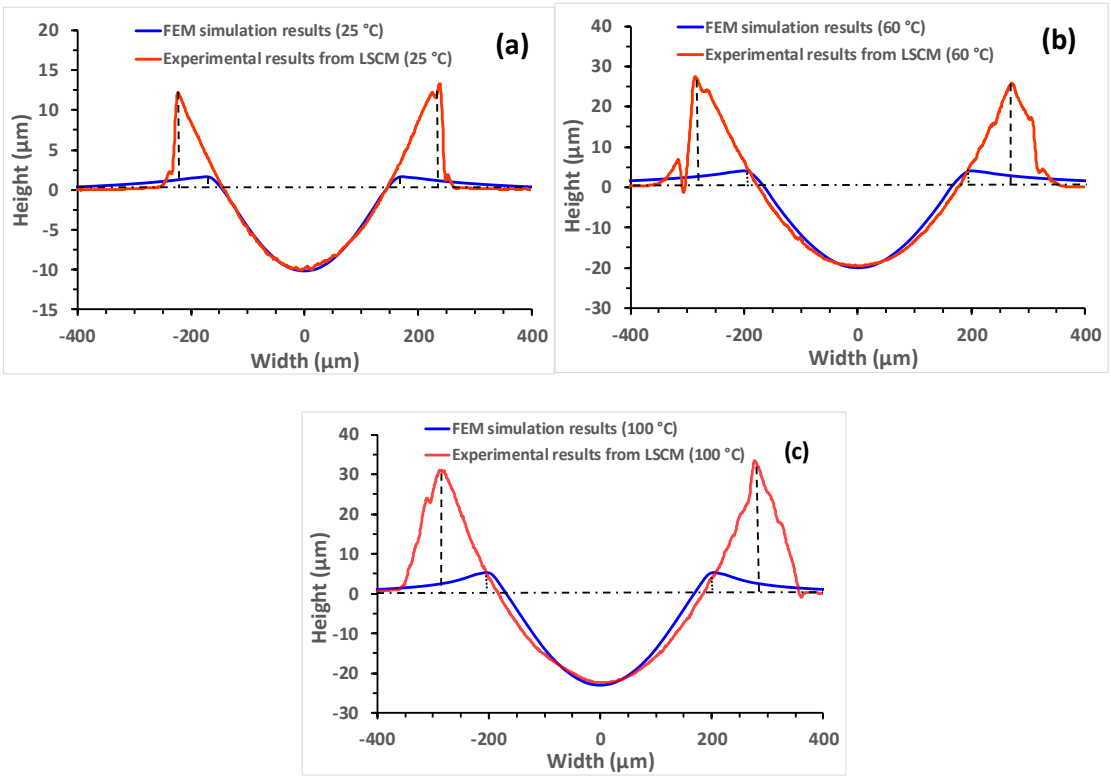

Figure VI-13. Experimental and FEM modeled scratch groove of PC with scratch load of 20 N at (a) 25 °C, (b) 60 °C, and (c) 100 °C.

A better understanding of the scratch behavior can be gained by considering the scratch coefficient of friction (SCOF). This parameter can be expressed as the ratio of tangential scratch load to the normal load [43, 96]. The values of the SCOF were

determined from the FEM model using Bowden and Tabor's theory presented in Equation (VI-18) below [154]:

$$SCOF = \mu_a + \mu_d \tag{VI-18}$$

$$\mu_d = \frac{4}{3\pi}\frac{a}{R} = \frac{4}{3\pi}\frac{\sqrt{2dR-d^2}}{R} \tag{VI-19}$$

Where μ_a is the adhesion coefficient of friction shown in Equation (VI-12), μ_d is the deformation coefficient of friction, a is the contact radius, R is the radius of the scratch tip, and d is the instantaneous scratch depth determined using the FEM simulation. The contact pressure P_r in Equation (VI-12) is the pressure underneath the scratch tip obtained from the FEM simulation.

Figure VI-14 presents the experimental and numerical SCOF measurements at the three tested temperatures. A good correlation is found between the experimental and FEM predicted results. This demonstrates the accuracy of the temperature-dependent model presented in this analysis. It is also observed that the SCOF only slightly increases across the scratch path for each of the three temperatures. This is partially caused by the absence of major changes in scratch deformation like fish scaling and stick-slip patterns. In fact, a previous study showed a correlation between these deformation feature changes and the value changes in SCOF [43, 96]. The figure also shows that the SCOF slightly increases with temperature. This is due to the softening of the polymer matrix at higher temperature, which increases the actual contact area. Therefore, a higher tangential load is needed to maintain the same scratching speed.

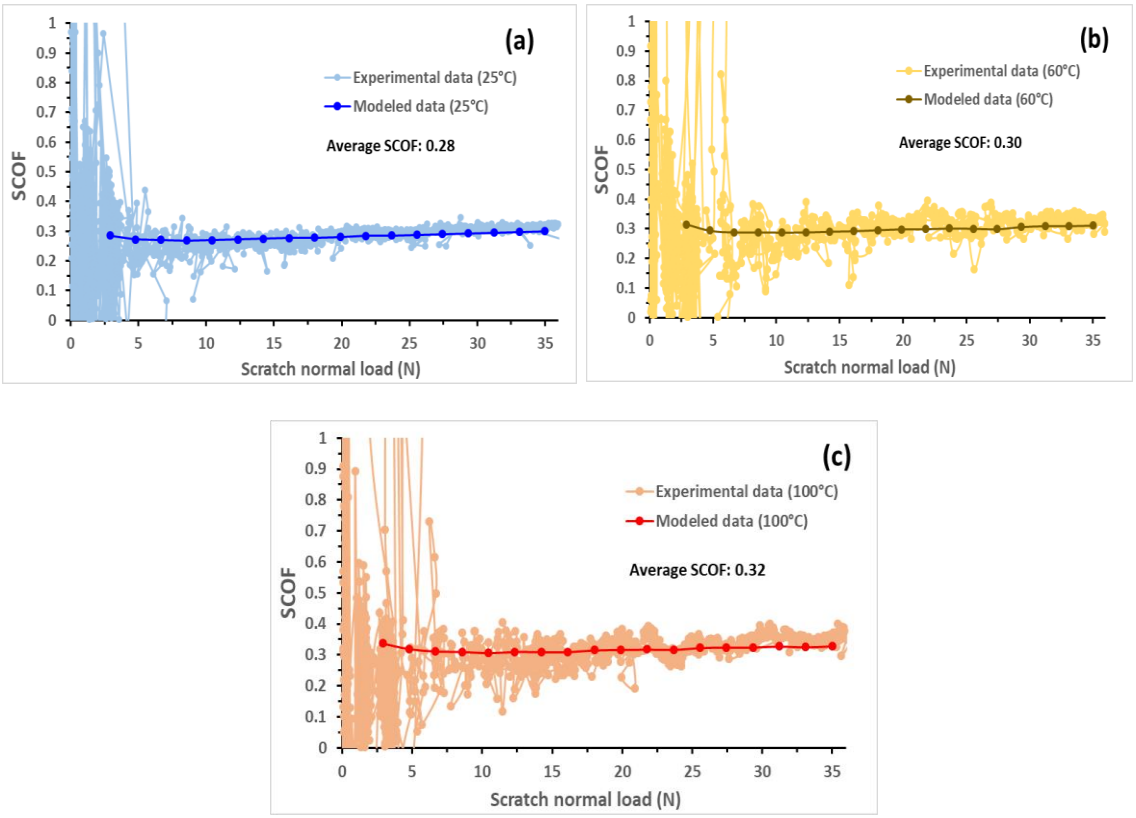

Figure VI-14. Experimental and modeled SCOF values on PC at (a) 25 °C, (b) 60 °C, and (c) 100 °C.

The modeling methodology proposed in the present study adopted temperature and strain rate dependent constitutive and contact relationships. This provides an effective approach to quantitatively predict the scratch behavior of amorphous polymers, including depth and scratch coefficient of friction (SCOF) at different temperatures. This approach will have a direct effect on several industrial applications in which temperature plays a significant role. Recent studies developed constitutive models to model the mechanical properties of semi-crystalline polymers [81]. Therefore, similar quantitative modeling analysis will be applied to low T_g semi-crystalline polymers in our future investigations.

The effect of temperature on crystallinity and skin-core morphology above T_g will be considered in these investigations. Furthermore, to model the material flow on the tip front and side edges [46], Eulerian or coupled Lagrangian-Eulerian (CLE) finite element methods will be considered in future studies [57, 153, 155].

CHAPTER VII

CONCLUSIONS AND FUTURE RESEARCH PLAN[*]

VII.1. Summary and Conclusion of Present Scratch & Mar Research

FEM modeling combined with experimental work was carried out in this dissertation to gain insight into the scratch and mar behaviors of polymeric systems. The focus of this work includes (1) Barrel mar damage (2) Scratch induced delamination in the multilayer system (3) Quantitative modeling to scratch deformations at elevated temperatures. The FEM model based on commercial software ABAQUS® was conducted to provide insight into the mechanics' knowledge and predict scratch behaviors. The mechanical testing such as uniaxial compression and tension test, COF measurements, etc. were performed to characterize the mechanical properties of polymer and contact properties between pairs. Furthermore, scratch tests according to ASTM/ISO standards were utilized to validate the FEM model. The conclusions of each subtopic were summarized as below:

The barrel mar modeling research investigates the mar resistance of three model amorphous polymers: PMMA, PC, and PS. The experimental analysis shows that PMMA has minimal changes in surface roughness and contrast on the mar path against the virgin

---

[*] Part of this chapter was reprinted from Wear, 444-445, Du, S., Hamdi, M., Sue, H.-J., Experimental and FEM analysis of mar behavior on amorphous polymers, 203155, Copyright (2020), with permission from Elsevier.

[*] Part of this chapter was reprinted from Polymer, 197, Du, S., Mullins, M., Hamdi, M., Sue H.-J., Quantitative modeling of scratch behavior of amorphous polymers at elevated temperatures, 122504. Copyright (2020), with permission from Elsevier.

background of the sample. This indicates that PMMA has the best mar visibility resistance. To conduct a meaningful FEM parametric study, the criteria that can correlate well with the mar visibility resistance of the model polymers were determined to be the maximum principal strain and total plastic energy dissipation values. Results show that mar resistance improves with a lower elastic modulus, a lower strain softening slope, a higher yield stress, and a higher strain hardening slope. Future studies will include further validation of other polymeric systems.

Two semi-rigid PET-based tri-layer laminates were used to demonstrate the methodology to determine the adhesive strength of multilayer polymer laminates with the combination of scratch test and FEM model. The FEA analysis of the stress state at the interface proves the maximum principal stress criterion is reasonable to be used to gain insight into scratch-induced delamination damage. Also from the FEA analysis, it is found that the reason why the PET-nylon-PET system showed early onset of adhesive failure is due to the high tensile stress generated around the scratch tip at the interface.

Then, the FEM modeling approach based on maximum principal stress criterion to determine the scratch-induced delamination strength was carried out and validated by the ASTM D7027 standard scratch test on a set of bi-layer epoxy coating systems. The experimental analysis shows a thicker top layer or a softer base layer could delay the onset of delamination during scratch. The FEM modeling results indicate the peak σ_1^t at the interface could either be located behind the scratch tip or on the scratch shoulder region, depending on the scratch normal load applied. The FEM parametric analysis shows that the onset of delamination would be delayed with a softer base layer, a top or base layer

with higher yield stress, a base layer with a lower strain-hardening slope, and a top surface with lower COF. The delamination mode will become more Mode-I dominant in a multilayer system if the base layer possesses a higher modulus or lower strain hardening slope. The present study indicates that it is possible to minimize the build-up of interfacial stresses by adjusting the layer thicknesses and material parameters of each layer in a laminated system upon scratching.

To precisely predict the scratch deformation of amorphous polymers at different temperatures, temperature and strain rate dependent post-yield behavior of amorphous polymers with precise yield stress values was determined using the Arruda-Boyce visco-plastic model calibrated with the Richeton cooperative model. Also, a temperature and pressure-dependent frictional model was established and included in the FEM analysis. By introducing calibrated post-yield data and modeled COF into the Drucker-Prager model, the pressure, temperature, and strain rate-dependent plastic constitutive behavior of amorphous polymeric materials was established. The predicted scratch depth, groove dimension, and SCOF were in good agreement with experimental tests. This indicates the effectiveness of the developed model to quantitatively simulate the scratch-induced deformation at various temperatures.

VII.2. Future Research Directions

VII.2.1. FEM modeling of sandpaper mar damage

As one of the commonly seen mar damages on polymeric surfaces, sandpaper mar has drawn significant attentions, as barrel tip mar damage. Therefore, it would be of great

importance to understand sandpaper mar behavior by using the numerical approach. The key to model the sandpaper mar damage is to simulate the multiple micro-scratches caused by micro-size random shape particles of sandpaper with appropriate statistical theories. Furthermore, efforts should be also given to take account the three-body abrasions and scratch intersection phenomena. This modeling work will be of benefit to the development of sandpaper roughening mar-resistant polymeric materials.

VII.2.2. FEM study of crack features involved with stick-slip phenomenon

It is well-known that the parabolic crack is the typical damage feature generated in scratch tests on many brittle polymeric surfaces, like the PMMA shown as Figure VII-1. Jiang et al. have demonstrated the parabolic crack feature in Figure VII-1 is due to the effect of stick-slip phenomenon in the crack formation [9]. Therefore, some appropriate techniques should be utilized to model the stick-slip phenomenon in the FEM simulation. Furthermore, the validated damage initiation and evolution criteria need to be involved in the FEM model to simulate crack. Since the energy conversion of both stick-slip and crack generation processes are complicated, the assumptions related have to be carefully made. Modeling stick-slip involved crack features could help to comprehensively understand the relationship between the crack features and material properties.

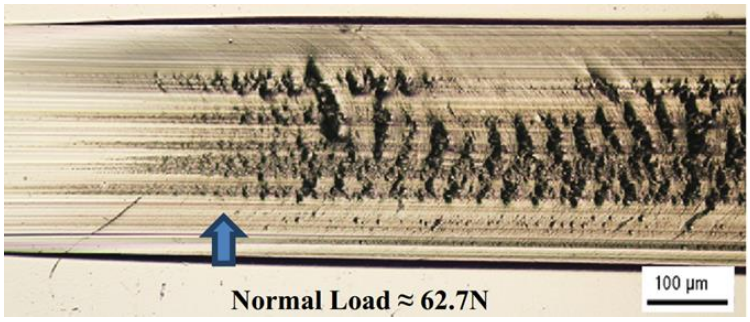

Figure VII-1. Parabolic crack features of PMMA. Reprinted from Moghbelli et al. [21].

VII.2.3. Quantitative precise prediction to scratch shoulder height and groove width

As illustrated in Chapter VI, the under-prediction of shoulder height and groove width is probably due to the ignore of material accumulation flowing from the tip front to the groove shoulder. This under-prediction will influence the scratch visibility analysis, since the topography change in groove height is one of the main reasons to cause scratch visible. Therefore, the precise quantitative prediction to scratch shoulder height and groove width is also important for many applications about damage visibility. One of the possible ways is to implement the coupled-eulerian-lagrangian (CEL) method into a 3D FEM scratch model. The CEL method is commonly used to simulate the metal scissel chip flow during the cutting process. However, employing this method to simulate the flow direction of polymer in the scratch test is the key. Once modeled successfully, it could help to build the relationship between mechanics and scratch visibility.

REFERENCES

[1] J. W. S. Xiao, D. Lipka and H.-J. Sue, "Correlation of TAMU Scratch and Mar Test Methodology to Field Performance of Automotive Interior Parts," in SPE Automotive TPO Engineering Polyolefin Global Conference Proceedings, Troy, MI, 2017.

[2] K. Friedrich, H. J. Sue, P. Liu, and A. A. Almajid, Scratch resistance of high performance polymers, Tribology International 44 (9) (2011) 1032-1046.

[3] R. L. Browning, H. Jiang, and H.-J. Sue, "Scratch behavior of polymeric materials," in Tribology and Interface Engineering Series, vol. 55: Elsevier, 2008, pp. 354-373.

[4] R. Browning, M. M. Hossain, J. Li, S. Jones, and H. J. Sue, Contrast-based evaluation of mar resistance of thermoplastic olefins, Tribology International 44 (9) (2011) 1024-1031.

[5] M. M. Hossain, R. Browning, R. Minkwitz, and H. J. Sue, Effect of Asymmetric Constitutive Behavior on Scratch-Induced Deformation of Polymers, Tribology Letters 47 (1) (2012) 113-122.

[6] M. M. Hossain, H. Jiang, and H. J. Sue, Effect of constitutive behavior on scratch visibility resistance of polymers-A finite element method parametric study, Wear 270 (11-12) (2011) 751-759.

[7] R. Browning, H. J. Sue, R. Minkwitz, and P. Charoensirisomboon, Effects of Acrylonitrile Content and Molecular Weight on the Scratch Behavior of Styrene-Acrylonitrile Random Copolymers, Polymer Engineering and Science 51 (11) (2011) 2282-2294.

[8] R. W. Hertzberg, H. Nordberg, and J. Manson, Fatigue crack propagation in polymeric materials, Journal of Materials Science 5 (6) (1970) 521-526.

[9] H. Jiang, R. Browning, and H. J. Sue, Understanding of scratch-induced damage mechanisms in polymers, Polymer 50 (16) (2009) 4056-4065.

[10] E. Moghbelli, R. Browning, W.-J. Boo, S. Hahn, L. Feick, and H.-J. Sue, Effects of molecular weight and thermal history on scratch behavior of polypropylene thin sheets, Tribology International 41 (5) (2008) 425-433.

[11] P. Chouwatat, M. Kotaki, M. Miyamoto, R. Nishimura, and A. Yokohama, Effect of soft base layer on scratch properties of acrylic hard coatings, Polymer Engineering and Science 56 (5) (2016) 528-535.

[12] G. Pagnoux, S. Fouvry, M. Peigney, B. Delattre, and G. Mermaz-Rollet, "Mechanical behavior of DLC coatings under various scratch conditions," in Internation Conference on Fracture Fatigue and Wear, 2014.

[13] I. G. Goryacheva, Contact Mechanics in Tribology. Moscow: Kluwer Academic Publishers, 1998.

[14] O. Vingsbo and S. Hogmark, Single-pass pendulum grooving—a technique for abrasive testing, Wear 100 (1-3) (1984) 489-502.

[15] E. Lughofer *et al.*, Self-adaptive evolving forecast models with incremental PLS space updating for on-line prediction of micro-fluidic chip quality, J Engineering Applications of Artificial Intelligence 68 (2018) 131-151.

[16] E. Hicks and A. Scroggie, Taber yarn-sheet abrasion test, J Textile Research Journal 18 (7) (1948) 416-423.

[17] S. Kuiry, Advanced scratch testing for evaluation of coatings, J Tribology Mechanical Testing, Bruker Nano Surfaces Division, USA (2012).

[18] ASTM D7027–05, Standard Test Method for Evaluation of Scratch Resistance of Polymeric Coatings and Plastics Using an Instrumented Scratch Machine, 2005.

[19] P.-L. Larsson, A. Giannakopoulos, E. Söderlund, D. Rowcliffe, and R. Vestergaard, Analysis of Berkovich indentation, J International Journal of Solids Structures 33 (2) (1996) 221-248.

[20] G. Molero and H.-J. Sue, Scratch behavior of model epoxy resins with different crosslinking densities, Materials & Design 182 (2019) 107965.

[21] E. Moghbelli, R. Banyay, and H.-J. Sue, Effect of moisture exposure on scratch resistance of PMMA, Tribology International 69 (2014) 46-51.

[22] S. Du, M. Mullins, M. Hamdi, and H.-J. Sue, Quantitative modeling of scratch behavior of amorphous polymers at elevated temperatures, Polymer 197 (2020) 122504.

[23] M. M. Hossain, R. Minkwitz, and H. J. Sue, Minimization of Surface Friction Effect on Scratch-Induced Deformation in Polymers, Polymer Engineering and Science 53 (7) (2013) 1405-1413.

[24] R. Browning, G. T. Lim, A. Moyse, L. Sun, and H. J. Sue, Effects of slip agent and talc surface‐treatment on the scratch behavior of thermoplastic olefins, J Polymer Engineering Science 46 (5) (2006) 601-608.

[25] M. Hamdi and H. J. Sue, Effect of color, gloss, and surface texture perception on scratch and mar visibility in polymers, Materials & Design 83 (2015) 528-535.

[26] H. Jiang, R. L. Browning, M. M. Hossain, H. J. Sue, and M. Fujiwara, Quantitative evaluation of scratch visibility resistance of polymers, Applied Surface Science 256 (21) (2010) 6324-6329.

[27] M. M. Hossain *et al.*, Rubber particle size and type effects on scratch behavior of styrenic-based copolymers, Polymer 63 (2015) 71-81.

[28] R. L. Browning *et al.*, Scratch behavior of soft thermoplastic olefins: effects of ethylene content and testing rate, Journal of materials science 43 (4) (2008) 1357-1365.

[29] J. Chrisman, S. Xiao, M. Hamdi, H. Pham, M. J. Mullins, and H.-J. Sue, Testing and evaluation of mar visibility resistance for polymer films, Polymer Testing 69 (2018) 238-244.

[30] S. Du, M. Hamdi, and H.-J. Sue, Experimental and FEM analysis of mar behavior on amorphous polymers, Wear 444 (2020) 203155.

[31] C. Barr, L. Wang, J. Coffey, and F. Daver, Influence of surface texturing on scratch/mar visibility for polymeric materials: a review, Journal of materials science 52 (3) (2017) 1221-1234.

[32] J. N. Reddy, An Introduction to the Finite Element Method, 2nd ed. ed. New York: McGraw-Hill., 1993.

[33] W. J. Boo *et al.*, Morphology and mechanical behavior of exfoliated epoxy/alpha-zirconium phosphate nanocomposites, Composites Science and Technology 67 (2) (2007) 262-269.

[34] P. Liu *et al.*, Influence of Trace Amount of Well-Dispersed Carbon Nanotubes on Structural Development and Tensile Properties of Polypropylene, Macromolecules 46 (2) (2013) 463-473.

[35] S. V. Nair, S. C. Wong, and L. A. Goettler, Fracture resistance of polyblends and polyblend matrix composites .1. Unreinforced and fibre-reinforced nylon 6,6/ABS polyblends, Journal of Materials Science 32 (20) (1997) 5335-5346.

[36] H. G. H. van Melick, L. E. Govaert, and H. E. H. Meijer, On the origin of strain hardening in glassy polymers, Polymer 44 (8) (2003) 2493-2502.

[37] G. Subhash and W. Zhang, Investigation of the overall friction coefficient in single-pass scratch test, Wear 252 (1-2) (2002) 123-134.

[38] H. Jiang, G. T. Lim, J. N. Reddy, J. D. Whitcomb, and H. J. Sue, Finite element method parametric study on scratch behavior of polymers, Journal of Polymer Science Part B-Polymer Physics 45 (12) (2007) 1435-1447.

[39] G. T. Lim, "Scratch behavior of polymers," Texas A&M University, 2005.

[40] G. T. Lim, M. H. Wong, J. N. Reddy, and H. J. Sue, An integrated approach towards the study of scratch damage of polymer, Jct Research 2 (5) (2005) 361-369.

[41] Y. Xu, D. Li, J. Shen, S. Guo, and H.-J. Sue, Scratch damage behaviors of PVDF/PMMA multilayered materials: Experiments and finite element modeling, Polymer 182 (2019) 121829.

[42] S. Xiao, H. Wang, F. Hu, and H.-J. Sue, Effect of moisture exposure on scratch behavior of model polyurethane elastomers, Polymer 137 (2018) 209-221.

[43] M. Hamdi, X. Zhang, and H.-J. Sue, Fundamental understanding on scratch behavior of polymeric laminates, Wear 380 (2017) 203-216.

[44] X. N. Jing, S. Maiti, and G. Subhash, A new analytical model for estimation of scratch-induced damage in brittle solids, Journal of the American Ceramic Society 90 (3) (2007) 885-892.

[45] L. C. A. van Breemen, L. E. Govaert, and H. E. H. Meijer, Scratching polycarbonate: A quantitative model, Wear 274 (2012) 238-247.

[46] M. M. Hossain, R. Minkwitz, P. Charoensirisomboon, and H. J. Sue, Quantitative modeling of scratch-induced deformation in amorphous polymers, Polymer 55 (23) (2014) 6152-6166.

[47] H. Jiang *et al.*, Mechanical Modeling of Scratch Behavior of Polymeric Coatings on Hard and Soft Substrates, Tribology Letters 37 (2) (2010) 159-167.

[48] Z. Z. Wang, P. Gu, H. Zhang, Z. Zhang, and X. P. Wu, Finite Element Modeling of the Indentation and Scratch Response of Epoxy/Silica Nanocomposites, Mechanics of Advanced Materials and Structures 21 (10) (2014) 802-809.

[49] M. M. Hossain, "Quantitative modeling of polymer scratch behavior," Doctor of Philosophy, Texas A&M University, 2013.

[50] C. S. Gauthier, R, Time and temperature dependence of the scratch properties of poly (methylmethacrylate) surfaces, Journal of Materials Science 35 (9) (2000) 2121-2130.

[51] J. Richeton, S. Ahzi, K. Vecchio, F. Jiang, and R. Adharapurapu, Influence of temperature and strain rate on the mechanical behavior of three amorphous polymers: Characterization and modeling of the compressive yield stress, International Journal of Solids and Structures 43 (7-8) (2006) 2318-2335.

[52] A. S. Wineman and K. R. Rajagopal, Mechanical response of polymers: an introduction. Cambridge university press, 2000.

[53] P. C. Hiemenz and T. P. Lodge, Polymer chemistry. CRC press, 2007.

[54] M. Hamdi, M. Puopolo, H. Pham, and H.-J. Sue, Experimental and FEM analysis of scratch behavior on polypropylene thin films: Effect of film orientation and ethylene monomer content, Tribology International 103 (2016) 412-422.

[55] M. M. Hossain, S. Xiao, H.-J. Sue, M. J. M. Kotaki, and Design, Scratch behavior of multilayer polymeric coating systems, 128 (2017) 143-149.

[56] V. K. Chandelia, H.-J. Sue, and M. M. Hossain, FEM Modeling on Scratch Behavior of Multiphase Polymeric Systems, Tribology Letters 66 (2) (2018) 62.

[57] W. M. Gao, L. Wang, J. K. Coffey, and F. Daver, Finite element simulation of scratch on polypropylene panels, Materials & Design 140 (2018) 400-408.

[58] M. Hamdi, D. Manica, and H. J. Sue, A Multidimensional Scaling Analysis of Surface Perceptual Parameters on Scratch and Mar Visibility Resistance in Polymers, Sae International Journal of Materials and Manufacturing 10 (2) (2017) 94-106.

[59] W. M. Gao, L. Wang, J. K. Coffey, and F. Daver, Understanding the scratch behaviour of polymeric materials with surface texture, Materials & Design 146 (2018) 38-48.

[60] J. Stráský, M. Janeček, P. Harcuba, M. Bukovina, and L. Wagner, The effect of microstructure on fatigue performance of Ti–6Al–4V alloy after EDM surface treatment for application in orthopaedics, Journal of the mechanical behavior of biomedical materials 4 (8) (2011) 1955-1962.

[61] G. Molero, S. Du, M. Mamak, M. Agerton, M. M. Hossain, and H. J. Sue, Experimental and numerical determination of adhesive strength in semi-rigid multi-layer polymeric systems, Polymer Testing 75 (2019) 85-92.

[62] H. Jiang, R. Browning, P. Liu, T. A. Chang, and H.-J. Sue, Determination of epoxy coating wet-adhesive strength using a standardized ASTM/ISO scratch test, Journal of Coatings Technology and Research 8 (2) (2011) 255-263.

[63] P. Lu, X. Xia, and Y. K. Chou, Interface delamination study of diamond-coated carbide tools considering coating fractures, Surface & Coatings Technology 260 (2014) 239-245.

[64] F. Wredenberg and P. L. Larsson, Delamination of thin coatings at scratch: experiments and numerics, Journal of Mechanics of Materials and Structures 4 (6) (2009) 1041-1062.

[65] P. Lu, H. Gomez, X. C. Xiao, and M. Lukitsch, etc., Coating thickness and interlayer effects on CVD-diamond film adhesion to cobalt-cemented tungsten carbides, Surface & Coatings Technology 215 (2013) 272-279.

[66] P. Lu, X. Xiao, M. Lukitsch, and K. Chou, Micro-scratch testing and simulations for adhesion characterizations of diamond-coated tools, Proceedings of NAMRI/SME 39 (2011).

[67] L. C. A. van Breemen, T. A. P. Engels, E. T. J. Klompen, D. J. A. Senden, and L. E. Govaert, Rate- and temperature-dependent strain softening in solid polymers, Journal of Polymer Science Part B-Polymer Physics 50 (24) (2012) 1757-1771.

[68] R. M. Caddell, R. S. Raghava, and A. G. Atkins, A yield criterion for anisotropic and pressure dependent solids such as oriented polymers, Journal of Materials Science 8 (11) (1973) 1641-1646.

[69] R. M. Caddell, R. S. Raghava, and A. G. Atkins, Pressure dependent yield criteria for polymers, Materials Science Engineering 13 (2) (1974) 113-120.

[70] F. Erdogan and G. Sih, On the crack extension in plates under plane loading and transverse shear, Journal of basic engineering 85 (4) (1963) 519-525.

[71] K. Palaniswamy and W. Knauss, Propagation of a crack under general, in-plane tension, International Journal of Fracture 8 (1) (1972) 114-117.

[72] M. Schöllmann, H. A. Richard, G. Kullmer, and M. Fulland, A new criterion for the prediction of crack development in multiaxially loaded structures, International Journal of Fracture 117 (2) (2002) 129-141.

[73] H. Jiang, J. W. Zhang, Z. R. Yang, C. K. Jiang, and G. Z. Kang, Modeling of competition between shear yielding and crazing in amorphous polymers' scratch, International Journal of Solids and Structures 124 (2017) 215-228.

[74] J. Zhang, H. Jiang, C. Jiang, Q. Cheng, and G. Kang, In-situ observation of temperature rise during scratch testing of poly (methylmethacrylate) and polycarbonate, Tribology International 95 (2016) 1-4.

[75] Z. E. A. Benaoun and J. Pan, Effects of elasticity and pressure-sensitive yielding on plane-stress crack-tip field, Engineering Fracture Mechanics 44 (5) (1993) 649-661.

[76] P. Dong and J. Pan, Elastic plastic analysis of cracks in pressure-sensitive materials, International Journal of Solids and Structures 28 (9) (1991) 1113-1127.

[77] J. Yue, C. Zhao, Y. Dai, H. Li, and Y. Li, Catalytic effect of exfoliated zirconium phosphate on the curing behavior of benzoxazine, Thermochimica acta 650 (2017) 18-25.

[78] E. M. Arruda, M. C. Boyce, and R. Jayachandran, Effects of strain rate, temperature and thermomechanical coupling on the finite strain deformation of glassy polymers, Mechanics of Materials 19 (2-3) (1995) 193-212.

[79] M. C. Boyce and E. M. Arruda, An experimental and analytical invastigation of the large strain compressive and tensile response of glassy polymers, Polymer Engineering and Science 30 (20) (1990) 1288-1298.

[80] M. C. Boyce, D. M. Parks, and A. S. Argon, Large inelastic deformation of glassy polymers .2. Numerical-simulation of hydrostatic extrusion, Mechanics of Materials 7 (1) (1988) 35-47.

[81] Y. Wang and E. M. Arruda, Constitutive modeling of a thermoplastic olefin over a broad range of strain rates, Journal of Engineering Materials Technology 128 (4) (2006) 551-558.

[82] G. Qun and W. Ajun, Effects of molecular weight, degree of acetylation and ionic strength on surface tension of chitosan in dilute solution, Carbohydrate Polymers 64 (1) (2006) 29-36.

[83] Q. Fichot, Characterization, Modeling, and Consequences of the Development During Plastic Flow of Large Anisotropy in the Wave-speeds, (2010).

[84] J. Zhang, H. Jiang, C. Jiang, G. Kang, Q. Kan, and Y. Li, Experimental and numerical investigations of evaluation criteria and material parameters' coupling effect on polypropylene scratch, Polymer Engineering and Science 58 (1) (2018) 118-122.

[85] C. Bauwens-Crowet, J. C. Bauwens, and G. Homes, Tensile yield-stress behavior of glassy polymers, Journal of Polymer Science Part A‐2: Polymer Physics 7 (4) (1969) 735-742.

[86] C. Bauwens-Crowet, J.-C. Bauwens, and G. Homes, The temperature dependence of yield of polycarbonate in uniaxial compression and tensile tests, Journal of Materials Science 7 (2) (1972) 176-183.

[87] J. C. Bauwens, Relation between the compression yield stress and the mechanical loss peak of bisphenol-A-polycarbonate in the β transition range, Journal of Materials Science 7 (5) (1972) 577-584.

[88] B. J. Briscoe, E. Pelillo, and S. K. Sinha, Scratch hardness and deformation maps for polycarbonate and polyethylene, Polymer Engineering and Science 36 (24) (1996) 2996-3005.

[89] J. Richeton, S. Ahzi, L. Daridon, and Y. Remond, A formulation of the cooperative model for the yield stress of amorphous polymers for a wide range of strain rates and temperatures, Polymer 46 (16) (2005) 6035-6043.

[90] J. Richeton, S. Ahzi, L. Daridon, and Y. Remond, Modeling of strain rates and temperature effects on the yield behavior of amorphous polymers, Journal De Physique Iv 110 (2003) 39-44.

[91] J. Richeton, S. Ahzi, K. S. Vecchio, F. C. Jiang, and R. R. Adharapurapu, Influence of temperature and strain rate on the mechanical behavior of three amorphous polymers: Characterization and modeling of the compressive yield stress, International Journal of Solids and Structures 43 (7-8) (2006) 2318-2335.

[92] R. Browning, G. T. Lim, A. Moyse, L. Y. Sun, and H. J. Sue, Effects of slip agent and talc surface-treatment on the scratch behavior of thermoplastic olefins, Polymer Engineering and Science 46 (5) (2006) 601-608.

[93] H. Jiang, R. Browning, J. Fincher, A. Gasbarro, S. Jones, and H. J. Sue, Influence of surface roughness and contact load on friction coefficient and scratch behavior of thermoplastic olefins, Applied Surface Science 254 (15) (2008) 4494-4499.

[94] N. Myshkin, M. Petrokovets, and A. J. T. I. Kovalev, Tribology of polymers: adhesion, friction, wear, and mass-transfer, 38 (11-12) (2005) 910-921.

[95] M. Tokita and T. Tanaka, Friction coefficient of polymer networks of gels, The Journal of chemical physics 95 (6) (1991) 4613-4619.

[96] F. Lei *et al.*, Scratch behavior of epoxy coating containing self-assembled zirconium phosphate smectic layers, Polymer 112 (2017) 252-263.

[97] ASTM D7027–13 Standard Test Method for Evaluation of Scratch Resistance of Polymeric Coatings and Plastics Using an Instrumented Scratch Machine, 2013.

[98] ISO 19252:2008, Plastics - Determination of Scratch Properties, 2008.

[99] D. S. Corporation, ABAQUS 2018 Documentation, ed, 2018.

[100] E. M. Arruda and M. C. Boyce, Evolution of plastic anisotropy in amorphous polymers during finite straining, International Journal of Plasticity 9 (6) (1993) 697-720.

[101] M. C. Boyce, D. M. Parks, and A. S. Argon, Large inelastic deformation of glassy-polymers .1. Rate dependent constitutive model, Mechanics of Materials 7 (1) (1988) 15-33.

[102] L. E. Govaert, P. H. M. Timmermans, and W. A. M. Brekelmans, The influence of intrinsic strain softening on strain localization in polycarbonate: Modeling and experimental validation, Journal of Engineering Materials and Technology-Transactions of the Asme 122 (2) (2000) 177-185.

[103] E. T. J. Klompen, T. A. P. Engels, L. E. Govaert, and H. E. H. Meijer, Modeling of the postyield response of glassy polymers: Influence of thermomechanical history, Macromolecules 38 (16) (2005) 6997-7008.

[104] L. C. A. van Breemen, T. A. P. Engels, C. G. N. Pelletier, L. E. Govaert, and J. M. J. Den Toonder, Numerical simulation of flat-tip micro-indentation of glassy polymers: Influence of loading speed and thermodynamic state, Philosophical Magazine 89 (8) (2009) 677-696, Art. no. Pii 909461806.

[105] M. Hamdi and H.-J. Sue, Effect of color, gloss, and surface texture perception on scratch and mar visibility in polymers, Materials & Design 83 (2015) 528-535.

[106] M. Hamdi, "Fundamental Understanding of Scratch and Mar Behavior of Polymers," Doctoral dissertation, Department of Mechanical Engineering, Texas A&M University, 2016.

[107] H. Pelletier, C. Gauthier, and R. Schirrer, Relationship between contact geometry and average plastic strain during scratch tests on amorphous polymers, Tribology International 43 (4) (2010) 796-809.

[108] D. J. A. Senden, S. Krop, J. A. W. van Dommelen, and L. E. Govaert, Rate- and temperature-dependent strain hardening of polycarbonate, Journal of Polymer Science Part B-Polymer Physics 50 (24) (2012) 1680-1693.

[109] Narisawa. I, A. F. Yee, and J. P. Harcup, Strength, Fracture and Fatigue of Polymers, Elsevier (2006).

[110] S. Abrate, Criteria for yielding or failure of cellular materials, Journal of Sandwich Structures & Materials 10 (1) (2008) 5-51.

[111] D. C. Drucker and W. Prager, Soil mechanics and plastic analysis for limit design, Quarterly of Applied Mathematics 10 (2) (1952) 157-165.

[112] S. S. Sternstein, Flaws, Anisotropy and failure of solid polymers, Journal of Rheology 23 (3) (1979) 412-413.

[113] H. Pelletier, A. L. Durier, C. Gauthier, and R. Schirrer, Viscoelastic and elastic-plastic behaviors of amorphous polymeric surfaces during scratch, Tribology International 41 (11) (2008) 975-984.

[114] H. Jiang, R. Browning, P. Liu, T. Chang, and H.-J. Sue, Determination of epoxy coating wet-adhesive strength using a standardized ASTM/ISO scratch test, Journal of Coatings Technology and Research 8 (2) (2011) 255-263.

[115] P. Cinelli, M. Schmid, E. Bugnicourt, M. B. Coltelli, and A. Lazzeri, Recyclability of PET/WPI/PE multilayer films by removal of whey protein isolate-based coatings with enzymatic detergents, J Materials 9 (6) (2016) 473.

[116] V. K. Rangari, M. Y. Shaik, H. Mahfuz, and S. Jeelani, Fabrication and characterization of high strength Nylon-6/Si3N4 polymer nanocomposite fibers, Materials Science and Engineering a-Structural Materials Properties Microstructure and Processing 500 (1-2) (2009) 92-97.

[117] B. Yalcin, Z. Ergungor, Y. Konishi, A. Cakmak, and C. Batur, Molecular origins of toughening mechanism in uniaxially stretched nylon 6 films with clay nanoparticles, Polymer 49 (6) (2008) 1635-1650.

[118] S. R. Nutt and L. Vaikhanski, Composite foam made from polymer microspheres reinforced with long fibers, ed: Google Patents, 2005.

[119] Z. Hu, S. Du, and J. Yang, Simulation Study on the Combined Harvester with Four Tracked Feet Passing through Ditch Based on RecurDyn, J Applied Mechanics and Materials 541-542 (2014) 756-762.

[120] S. Du, "Residual Stress Analysis For Axisymmetric Welded Cone & Tee Assembly Model " M.S., Department of Mechanical Engineering & Mechanics, Lehigh University, Lehigh preserve, 2579, 2016.

[121] Z. Hu, S. Du, B. Shen, and L. Wang, Mechanical Property Analysis on Cutting Tool of the Ice and Snow Removing Machine Based on ANSYS, J Applied Mechanics & Materials 779 (2015).

[122] A. Argon, A theory for the low-temperature plastic deformation of glassy polymers, Philosophical Magazine 28 (4) (1973) 839-865.

[123] T. Ree and H. Eyring, Theory of non‐newtonian flow. i. solid plastic system, Journal of Applied Physics 26 (7) (1955) 793-800.

[124] R. Haward and G. Thackray, The use of a mathematical model to describe isothermal stress-strain curves in glassy thermoplastics, 302 (1471) (1968) 453-472.

[125] R. Haward *et al.*, The effect of chain structure on the annealing and deformation behaviour of polymers, 258 (6) (1980) 643-662.

[126] R. N. Haward, The physics of glassy polymers. Springer Science & Business Media, 2012.

[127] D. Parks, A. Argon, and B. Bagepalli, Large elastic-plastic deformation of glassy polymers, Part I (1984).

[128] M. C. Wang and E. Guth, Statistical theory of networks of non‐Gaussian flexible chains, The Journal of Chemical Physics 20 (7) (1952) 1144-1157.

[129] V. Tømmernes, "Implementation of the Arruda-Boyce Material Model for Polymers in Abaqus," Institutt for konstruksjonsteknikk, 2014.

[130] C. Xiang, H. J. Sue, J. Chu, and B. Coleman, Scratch behavior and material property relationship in polymers, Journal of Polymer Science Part B-Polymer Physics 39 (1) (2001) 47-59.

[131] C. Chung, W. Hennessey, and M. Tusim, Frictional behavior of solid polymers on a metal surface at processing conditions, Polymer Engineering Science 17 (1) (1977) 9-20.

[132] R. C. Bowers, Coefficient of friction of high polymers as a function of pressure, Journal of Applied Physics 42 (1971) 4961-4970.

[133] B. J. Briscoe and D. Tabor, Shear properties of thin polymeric films, Journal of Adhesion 9 (2) (1978) 145-155.

[134] R. Quinson, J. Perez, M. Rink, and A. Pavan, Yield criteria for amorphous glassy polymers, J Journal of Materials Science 32 (5) (1997) 1371-1379.

[135] H. Altenbach and K. Tushtev, A new static failure criterion for isotropic polymers, Mechanics of Composite Materials 37 (5-6) (2001) 475-482.

[136] P. Bardia and R. Narasimhan, Characterisation of pressure-sensitive yielding in polymers, Strain 42 (3) (2006) 187-196.

[137] A. F. Epee, F. Lauro, B. Bennani, and B. Bourel, Constitutive model for a semi-crystalline polymer under dynamic loading, International Journal of Solids and Structures 48 (10) (2011) 1590-1599.

[138] A. I. Karabinis, T. C. Rousakis, and G. E. Manolitsi, 3D finite-element analysis of substandard RC columns strengthened by fiber-reinforced polymer sheets, Journal of Composites for Construction 12 (5) (2008) 531-540.

[139] M. Kitagawa and T. Yoneyama, Plastic dilatation due to compression in polymer solids, Journal of Polymer Science Part C: Polymer Letters 26 (4) (1988) 207-212.

[140] L. Yang, Y. Yan, Y. J. Liu, and Z. G. Ran, Microscopic failure mechanisms of fiber-reinforced polymer composites under transverse tension and compression, Composites Science and Technology 72 (15) (2012) 1818-1825.

[141] ISO 19252:2008, Plastics - Determination of Scratch Properties, Annual Book of ISO Standards, 2008.

[142] M. A. Meyers and K. K. Chawla, Mechanical Behavior of Materials, 2nd Edition (Mechanical Behavior of Materials, 2nd Edition). 2009, pp. 1-856.

[143] Abaqus analysis user's manual, 2007.

[144] R. Gulino, S. Bair, W. O. Winer, and B. Bhushan, Temperature-measurement of microscopic areas within a simulated head tape interface using infrared radiometric technique, Journal of Tribology-Transactions of the Asme 108 (1) (1986) 29-34.

[145] K. A. Laux, A. Jean-Fulcrand, H. J. Sue, T. Bremner, and J. S. S. Wong, The influence of surface properties on sliding contact temperature and friction for polyetheretherketone (PEEK), Polymer 103 (2016) 397-404.

[146] A. F. Yee, R. Bankert, K. Ngai, and R. Rendell, Strain and temperature accelerated relaxation in polycarbonate, Journal of Polymer Science Part B: Polymer Physics 26 (12) (1988) 2463-2483.

[147] Z. Li and J. Lambros, Strain rate effects on the thermomechanical behavior of polymers, International Journal of solids structures 38 (20) (2001) 3549-3562.

[148] J. Richeton, S. Ahzi, L. Daridon, and Y. J. P. Rémond, A formulation of the cooperative model for the yield stress of amorphous polymers for a wide range of strain rates and temperatures, 46 (16) (2005) 6035-6043.

[149] F. Rietsch and B. Bouette, The compression yield behaviour of polycarbonate over a wide range of strain rates and temperatures, European Polymer Journal 26 (10) (1990) 1071-1075.

[150] T. Fort, Adsorption and boundary friction on polymer surfaces, Journal of Physical Chemistry 66 (6) (1962) 1136-1143.

[151] C. Gsell and A. J. Gopez, Plastic banding in glassy polycarbonate under plane simple shear, Journal of Materials Science 20 (10) (1985) 3462-3478.

[152] C. Jiang, H. Jiang, J. Zhang, and G. Kang, Analytical model of friction behavior during polymer scratching with conical tip, J Friction 7 (5) (2019) 466-478.

[153] D. J. Benson and S. Okazawa, Contact in a multi-material Eulerian finite element formulation, Computer Methods in Applied Mechanics and Engineering 193 (39-41) (2004) 4277-4298.

[154] F. P. Bowden, F. P. Bowden, and D. Tabor, The friction and lubrication of solids. Oxford university press, 2001.

[155] F. Ducobu, E. Rivière-Lorphèvre, M. Galindo-Fernandez, S. Ayvar-Soberanis, P.-J. Arrazola, and H. Ghadbeigi, Coupled Eulerian-Lagrangian (CEL) simulation for modelling of chip formation in AA2024-T3, Procedia CIRP 82 (2019) 142-147.